1-31-2013

Nonlinear Microscopy for Material Characterization

Reed Weber

Reed Weber

Candidate

Optical Science & Engineering - Physics

Department

This dissertation is approved, and it is acceptable in quality and form for publication:

Approved by the Dissertation Committee:

Wolfgang Rudolph , Chairperson

James Thomas

Keith Lidke

John Grey

Nonlinear microscopy for material characterization

by

Reed Alan Weber

B.S. Physics, Bethel University, 2005
M.S. Optical Science and Engineering, University of New Mexico, 2009

DISSERTATION

Submitted in Partial Fulfillment of the
Requirements for the Degree of

Doctor of Philosophy
Optical Science and Engineering

The University of New Mexico

Albuquerque, New Mexico

December, 2012

Dedication

To my wife and parents.

Acknowledgments

Many thanks to my advisor, Prof. Wolfgang Rudolph, for his devoted guidance and feedback. Insight into his thinking process has been truly invaluable. Additionally, thanks to Prof. James Thomas, Dr. Xuejun Liu, and Dr. Mark Mero for sharing significant insights on the research conducted here. I am indebted to Dr. Luke Emmert and Duy Nguyen for sharing their intimate knowledge of damage studies and preparing the HfO_2 samples.

Thanks to those who have contributed directly to this work, including: Cristina Rodriguez, Jacob Gorman, Travis Savage, Dr. Eric Carnes, Stoney Haver, Michael Sheyka, Dr. Keith Lidke, Peter Relich, Dr. Carmen S. Menoni, and Dr. Dinesh Patel. For feedback on the work completed here, I'm very thankful to Prof. Mansoor Sheik-Bahae and Dr. John Grey. Thanks to Dr. Igor Pastirk for his kind help with the SLM software. Thanks to the rest of our group for many insightful and fun conversations: Dr. Vasudevan Nampoothiri, Mao Chenchen, Zhang Xuerong, Sun Zhanliang.

I'm very blessed to have such an amazing family. Paula, Marilyn, Mark and Ross, I love you very much. In all things, and in this, thanks to Jesus Christ.

Nonlinear microscopy for material characterization

by

Reed Alan Weber

B.S. Physics, Bethel University, 2005
M.S. Optical Science and Engineering, University of New Mexico, 2009

Ph.D., Optical Science and Engineering, University of New Mexico, 2012

Abstract

Making use of femtosecond laser sources, nonlinear microscopy provides access to previously unstudied aspects of materials. By probing third order nonlinear optical signals determined by the nonlinear susceptibility $\chi^{(3)}$, which is present in all materials, we gain insight not available by conventional linear or electron microscopy. Third-harmonic (TH) microscopy is applied to supplement laser-induced damage studies of dielectric oxide thin film optical coatings. We present high contrast (S/N$>$ 100 : 1) TH imaging of $\approx$ 17 nm nanoindentations, individual 10 nm gold nanoparticles, nascent scandia and hafnia films, and laser induced material modification both above and below damage threshold conditions in hafnia thin-films. These results imply that TH imaging is potentially sensitive to laser-induced strain as well as to nanoscale defects or contamination in oxide films. Compared to other sensitive imaging techniques such as Nomarski and dark field, TH imaging exhibits dramatically increased sensitivity to typical material modifications undergone during the

formation of optical damage as evidenced by a dynamic range $\approx 10^6 : 1$. Four-wave mixing (FWM) microscopy is employed to investigate delay dependent FWM signals and their implied characteristic resonant response times in multiple solvents. Mathematical modeling of resonant coherent anti-Stokes Raman scattering (CARS), coherent Stokes Raman scattering (CSRS) and stimulated parametric emission (SPE) processes supplement the FWM studies and suggest a resonant CARS process that accounts for $\approx 95\%$ of the total visible FWM signal which probes a characteristic material response time ≈ 100 fs. This signal enhancement likely indicates the net effects of probing several Raman active C-H stretch bands near 2950 cm^{-1}. This FWM technique may be applied to characterize the dominant resonant response of the sample under study. Furthermore this technique presents the newfound capability to provide estimates of characteristic material dephasing times in combination with potential spatial resolution ≈ 1 μm. In addition to TH and FWM microscopy, a genetic algorithm is developed and implemented that allows for the synthesis of arbitrary temporal waveforms to maximize the generation of nonlinear optical signals in the focal plane of a microscope without any prior knowledge of the experiment. This algorithm is demonstrated to compensate high order optical dispersion and thereby increase TH microscopy signals $\approx 10\times$ in a fused silica sample.

Contents

List of Figures

List of Tables

Glossary

$\chi^{(n)}$	nth-order optical susceptibility
CARS	coherent anti-Stokes Raman scattering
CSRS	coherent Stokes Raman scattering
FROG	f requency-resolved optical gating
fs LIDT	femtosecond laser-induced damage threshold
FWHM	full width at half maximum
FWM	four wave mixing
G	number of generations
GA	Genetic algorithm
I	optical intensity
IBS	ion beam sputtering
MIIPS	multiphoton intrapulse interference phase scan
N	population size
NIR	near-infrared

P	material polarization
PPLN	periodically poled lithium niobate
SFG	sum frequency generation
SH, SHG	second harmonic (generation)
SLM	spatial light modulator
S/N	signal to noise ratio
TH, THG	Third-harmonic (generation)
THCP	Third-harmonic from circularly polarized illumination
THLP	Third-harmonic from linearly polarized illumination
Ti:S	Titanium sapphire oscillator
OPO	Optical parametric oscillator

Chapter 1

Introduction

The goal of this chapter is to provide the reader with a broad introduction to the work presented in this thesis. This includes motivation for using nonlinear microscopy, motivation for the specific research problems addressed by subsequent chapters, an outline of research goals and an outline of the material presented in this thesis. When appropriate, additional motivating details are presented at the onset of each chapter.

1.1 The rise of nonlinear microscopy

Advances in science often have been reliant on the development of new methods for observing the universe around us. This certainly holds true in the area of microscopic evaluation of matter. The advent of optical microscopy more than 400 years ago revolutionized the study of biology and helped pave the way for modern medicine. The arrival of electron microscopy furthered advances for all science by resolving miniscule features of less than 2 nanometers in size. These two techniques each display their own unique merits because they represent two different ways of interrogating matter on a microscopic scale. Traditional optical microscopy probes matter via its

interaction with low intensities of light, while electron microscopy probes matter via its interaction with other matter. Throughout this thesis, traditional optical microscopy will be referred to as so-called linear optical microscopy because the optical signals depend linearly on the electric field of incident light, E. A linear dependence on electric field governs commonplace observation of light and explains why humans perceive objects with properties such as color and opacity. This nomenclature is adopted here for clarity so that we may distinguish a third way of of interrogating matter on a microscopic scale. The scope of discussion in this thesis centers upon probing matter via its interaction with high intensities of light in so-called nonlinear optical microscopy. As you may have gathered, nonlinear optical microscopy owes its name to the many nonlinear optical processes of modern science that exhibit signals proportional to higher powers of the electric field ($\propto E^2, E^3$ etc.).

While linear optical microscopy and electron microscopy remain proven scientific tools and make use of a diverse range of contrast mechanisms including transmission, reflection, scattering, optical phase change and optical interference, these techniques possess inherent shortcomings that render them unsuitable for numerous applications. A quintessential example of these shortcomings is found in the inability of both linear optical microscopy and electron microscopy to image interfaces between optical index matched components of living biological samples. Linear optical microscopy fails to create contrast where optical indices are matched and where the phase change induced by the surface is irresolvably small. Electron microscopy may resolve these features, but in doing so requires preparation that will both permanently alter the sample and kill any living components contained therein. Nonlinear optical microscopy, however, presents a method to image interfaces between optical index matched components of living biological samples in real time video rate [1, 2, 3] without the need for staining or other permanent sample alteration. By probing a higher order optical susceptibility present in the sample, nonlinear microscopic techniques access a fundamentally different way of creating contrast and have established

novel contrast mechanisms with widespread application.

Early work in nonlinear optics laid key foundations for microscopy by characterizing both the multiphoton processes, such as harmonic generation [4, 5, 6], and the material susceptibilities [7, 8] that would later find application in nonlinear microscopy. Seminal work with two-photon excited fluorescence (TPEF) microscopy in 1990 [9] sparked a decade of rampant growth in the area of nonlinear microscopy research. Broad acceptance of TPEF microscopy in the biological and medical sciences, largely due to inherent 3-dimensional sectioning and large signal yield within living biological samples, bolstered the development of second-harmonic (SH)[10, 11] and third-harmonic (TH) microscopy [1, 12] and kindled a renewed interest in coherent anti-Stokes Raman scattering (CARS) microscopy which had been pioneered nearly a decade earlier [13]. This era of exponential growth [14] for nonlinear microscopy research paralleled the arrival and prevalence of robust and commercially available femtosecond lasers as well as the introduction of the first commercial nonlinear microscope in 1996 (BioRad Microscience). As is the case with all nonlinear optics, nonlinear microscopy relies upon intense light interacting with matter [15]. The widespread availability of femtosecond laser sources has proven to be a boon to nonlinear microscopy in that such sources provide a high peak intensity of light in tandem with modest average power which may be kept below the damage threshold of the sample being studied. The dependence of nonlinear signal generation on the intensity of incident light is discussed further in Section 2.1. Over the last few decades, nonlinear microscopy has emerged as a powerful tool not only for imaging but also for 3-dimensional motion tracking [16], single molecule detection [17], the study of fundamental material parameters [18, 19, 20, 21, 22] as well as less idiomatic research including photothermal cancer treatment [23] and the conservation of painted artifacts [24]. The work presented in this thesis follows in the vein of research concerned with characterizing fundamental material parameters as outlined in the next two sections.

1.2 Motivation and goals

The work presented here focuses mainly on applications in microscopy with the third-order nonlinear processes third-harmonic generation (THG) and four-wave mixing (FWM). Discussed in greater detail in Chapter 2, these processes exhibit proportionality to E^3 and probe the third-order nonlinear optical susceptibility $\chi^{(3)}$. Unlike the second order susceptibility $\chi^{(2)}$, $\chi^{(3)}$ is non-vanishing in all materials. For this reason, third-order nonlinear processes are immanently applicable to characterizing diverse materials. Though all third-order nonlinear processes rely upon the interaction of four photons in a material, works in the literature distinguish third-harmonic generation (THG) from other four-wave mixing (FWM) processes. This distinction between THG and FWM equally follows from differences in relevant theory and in application and emphasizes that THG and FWM probe different material parameters. Paradigmatic applications of TH microscopy include imaging of material interfaces [25, 26] and material anisotropy [27]. Interpreted broadly, typical applications in TH microscopy may be considered to probe the geometry of the material under study. In contrast, FWM microscopy borrows heavily from FWM spectroscopy, most familiarly CARS, to recast known electronic and vibrational material resonances into contrast enhancement for imaging. Again interpreting broadly, typical applications in FWM microscopy deal with using tunable laser sources to probe material resonances. The basic concepts behind the work presented in the remainder of this thesis follow along the lines of these stereotypes of TH and FWM application. With TH microscopy we hope to probe fundamental geometries of oxide thin films with application to laser-induced damage studies. With FWM microscopy we hope to probe the effects of material resonance and relate them to time domain behavior of FWM signals. In addition, we consider the femtosecond laser sources implemented for both TH and FWM microscopy and optimize them where possible. A final application presented in this thesis has implications for both TH and FWM microscopy: temporal wave-

form synthesis for optimization of nonlinear signal generation. The remainder of this section is dedicated to a concise discussion of the motivation and goals for the applications of TH and FWM microscopy presented in this thesis.

Motivation for TH microscopy of dielectric oxide thin films. TH microscopy presents the potential to serve as a unique diagnostic tool for investigating dielectric oxide thin films. Such films are renowned for their demonstrated ability to comprise high damage threshold optical coatings for use in high energy laser applications. However, current high energy lasers are capable of damaging every material known to science. While this will always be true if the beam cross section is allowed to be small enough, simple beam expansion represents one way to simultaneously increase overall laser energy while decreasing the laser fluence and circumventing material breakdown. With this in mind, the improvement of oxide films supports both further development and miniaturization of high energy laser systems. Due to the complex interplay of physical processes involved in optical damage, the study of laser-matter interactions in oxide films is firmly entrenched in the realm of empirical science and as such makes use of diverse data, including imaging, to aid improvement of the films. Production of high quality films has reached a level such that physical processes within the amorphous films may be characterized through deterministic femtosecond pulse damage studies. Indeed, fs laser-induced damage threshold (fs LIDT) studies represent the primary method of interrogation in support of developing phenomenological models [28, 29, 30, 31, 32] to explain optical damage in such films. Optical imaging has also played an important role in fs LIDT studies by revealing different morphologies of damage growth [33, 34] and suggesting the development of laser induced vacancy defects that may serve as damage initiation sites under vacuum conditions [35, 36]. Though fs LIDT studies suggest the presence of material modification prior to damage it is not yet clear whether such modification results in a permanent source of imaging contrast. Based on previously

demonstrated uses of TH microscopy and the properties of the films themselves, we suggest that TH microscopy may provide distinctive information related to several aspects of oxide film study.

A first area of interest is the suitability of TH microscopy for producing high contrast images following laser-induced damage of the films. Nascent oxide films and their substrates are expected to exhibit highly isotropic material symmetry. As will be discussed in Section 2.2.2, third-harmonic from circularly polarized illumination (THCP) results in the suppression of signals from isotropic media. For this reason, any laser exposures of the film which result in anisotropic material modification may serve as a source of contrast in THCP images. Furthermore, as previously demonstrated for anisotropy in the form of biogenic crystals [27, 18] and gold nanorods [37], such images are expected to yield extremely high contrast due to nearly background free detection. If true, THCP may offer significant advantages over traditional techniques used to interrogate laser damage exposures. Also, THCP imaging may be able to detect material modification that occurs in exposures below damage threshold, thus answering the open question concerning formation of permanent material modification prior to damage formation.

A second area of interest is the potential for TH imaging to characterize the nascent films themselves. The high damage threshold of oxide films allows TH imaging with relatively high incident power[†] in order to generate detectable signals even from weak sources of anisotropy. Considering the properties of oxide films in view of underlying theory for THCP, oxide films appear to present an ideal candidate for such high-sensitivity THCP microscopy. In this way it may be possible to image very small intrinsic anisotropy in the films themselves. Believed to be the research

[†]For reference, the damage threshold of biological samples (under tight-focusing conditions) is typically reached between several mW and tens of mW's of near-infrared femtosecond illumination, while oxide films allow imaging with several hundred mW using the same laser sources.

attempt with closest proximity to this assertion, THCP has been applied previously to characterizing broad spatial scale (several mm) anisotropy of surface layers in bulk semiconductors (GaAs, Si) [38].

A third area of interest is the potential for TH imaging to be implemented while a damage experiment is running. Previously, TH has shown the ability to serve as a local online monitor for optical breakdown in polymethyl methacrylate (PMMA) thick films (50 μm) [39]. It may also be applied to oxide thin films to monitor the formation of material modification leading to damage while the experiment is ongoing.

Taking all of these considerations into account, TH imaging seems to hold great promise for interrogation of oxide films. Even though TH imaging exhibits the potential to characterize oxide films before, during and after exposure to high fluence laser radiation, no one has yet undertaken a comprehensive study of the usefulness of TH imaging to this end. For these reasons, we desire to evaluate the sensitivity and utility of TH microscopy to sources of contrast encountered in high quality oxide thin films. Additional details concerning laser damage studies and oxide thin films are presented in Section 4.1.

Motivation for FWM microscopy time dependent measurements. Making use of femtosecond pulses, FWM microscopy has the potential to make possible the study of femtosecond scale material dynamics including electronic and vibrational dephasing in combination with spatial resolution $\approx$ 1 μm. However, current techniques in FWM specialize in either high resolution time domain measurements or high resolution spatial measurements and little work has been done to evaluate the extension of high spatial resolution techniques to time domain measurements and vice versa.

FWM techniques aimed at high resolution temporal measurements rely on the

angular separation of beams in illumination and in detection therefore making it impossible to implement them without partially sacrificing the resolution capabilities of high numerical aperture microscope objectives. As a figure of merit, the BoxCARS technique [40] shown in Fig. 1.1 has made an attempt to implement spatially separated detection in microscopy in order to simplify spectral filtering, however it is limited to a spatial resolution of several microns. Such limited resolution is put in context when considering that imaging of cells and intracellular components regularly requires spatial resolution $\leq$ 1 μm. Another non-microscopy FWM method for high resolution time domain measurements, this one based on photon echoes[41], makes use of angular separation of three or more femtosecond pulses with variable time delay in order to probe solute-solution energy transfer and complicated molecular dynamics[42, 43]. A similar technique has been employed for three pulse CARS interrogation of vibrational dephasing in acetone [44] and benzene [45]. However, all of these techniques are limited in spatial resolution because they sacrifice the benefits of a highly corrected microscope objective by necessitating either multiple long focal length lenses or multiple beams underfilling a microscope objective. Unfortunately, powerful techniques for investigating the effects of dephasing with high resolution ($\pm$ 1 fs) do not adapt themselves well to microscopy.

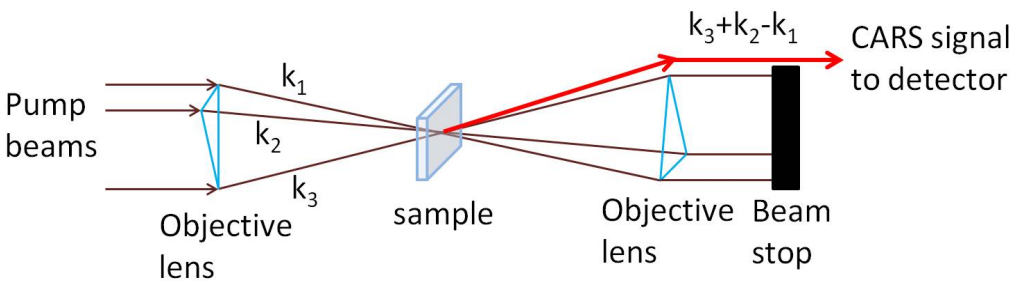

Figure 1.1: Schematic of the BoxCARS setup with spatially separated detection of the CARS signal.

In high spatial resolution FWM imaging it is well established, following from

results with FWM spectroscopy [46], that FWM microscopy may yield high contrast images with chemical specificity based on signal enhancement via vibrational [47, 48] and electronic resonances [49, 50, 51] even within living cells [52]. Used extensively, CARS microscopy routinely demonstrates spatial resolution on a cellular or subcellular scale ($\leq$ 1μm). However, what if one desires not only to exploit these resonances to enhance imaging contrast, but also to explore the transient behavior of these resonances in combination with microscopic spatial resolution? For coherent processes such as FWM, this amounts to measuring the effects of characteristic material dephasing times.

We suggest that instead of adapting techniques from temporal studies to high resolution imaging, it is worth investigating the types of temporal information a standard FWM imaging technique may provide. We consider the common case of two source collinear excitation in a FWM microscope. In principle, simply varying the delay between the two incident pulse trains is enough to provide information on the presence of finite material response times on the order of the pulse durations or longer. It's not immediately clear what type of information is evident in such inter-pulse delay scans, but they may provide a method of simultaneously imaging with $\approx$ 1 μm spatial resolution and differentiating chemical species via characteristic material response times.

Motivation for temporal waveform synthesis. The signal yield of any nonlinear optical process exhibits strong dependence on the temporal profile of the excitation pulse. Fittingly, temporal shaping of femtosecond pulses has long been used to optimize signals from nonlinear processes. Of interest here is the optimization of nonlinear optical signals via synthesis of arbitrary temporal waveforms. By interpreting the resulting waveforms, one may gain insight into both the underlying physics of the nonlinear process as well as the sum dispersion present in the beam path.

Two things have been clear since the onset of temporal pulseshaping. First, temporal pulse shaping is most readily implemented by control in the spectral domain. This reflects the fact that no electronic techniques exist that are capable of modulating the temporal behavior of femtosecond pulses directly. Such spectral control over temporal behavior may be as simple as inserting a slab of dispersive material into the beampath, though more useful apparatuses include prism compressors to control dispersion [53, 54, 55] and spatial light modulators (SLMs) composed of many liquid crystals to directly control the phase of spatially separated spectral components (Fig. 1.2). Second, even when one knows what temporal pulse shape to apply to an experiment[†] it's not always clear what spectral phase compensation needs to be implemented to produce that shape in the region of interest. This reflects the reality that factors such as aberrations and high order dispersion may complicate even simple optical setups. To complicate matters further, perhaps the most intriguing applications of temporal pulse shaping involve systems where the optimal pulse shape itself is unknown. Such applications include coherent control of chemical reactions [56] and the enhancement of imaging contrast in resonant systems [57, 58].

Regardless of the complexity of the pulse shape involved, whenever the optimal spectral phase compensation is unknown it has become typical practice in the literature to implement an SLM and a learning algorithm in order to find the proper spectral phase compensation [59]. One well established technique to determine the optimal phase compensation to produce a given pulse shape is called multiphoton intrapulse interference phase scan (MIIPS) [60, 61, 62]. However, this technique requires the desired pulse shape to be known. Since our interest in pulse shaping is to optimize signals generated in the focal plane of a microscope via synthesis of arbitrary temporal waveforms, we turn to a genetic algorithm to iteratively opti-

[†]Here we are mainly concerned with maximizing a nonlinear signal in a material of interest. Such maximization is influenced by (1) the optical setup (dispersion, aberrations, etc.), (2) properties of the material and (3) characteristics of the nonlinear process itself.

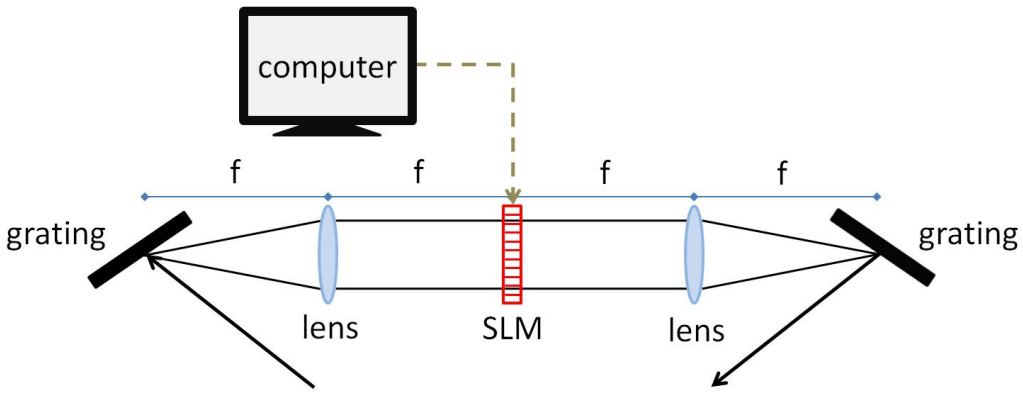

Figure 1.2: Schematic of a generic SLM based pulse shaper. A grating gives spatial separation of spectral components in the incoming beam. The spatially separated spectral components are controlled in phase and amplitude by the SLM liquid crystal pixel masks. The spectral components are recombined and a shaped temporal pulse exits.

mize the generated optical signals simply via parameterization of the SLM pixels. Although the current state of the art allows fully independent control of the phase, amplitude and polarization of spatially separated spectral components via four liquid crystal pixel masks [63], in this first attempt at temporal pulse shaping, we attempt phase control alone in our desire to develop a method that will work to optimize the temporal pulse profile automatically without any prior notion of the experiment involved.

Thesis goals. The goals of this thesis are:

1. To characterize regions of critical alignment in titanium:sapphire oscillator (Ti:S) and optical parametric oscillator (OPO) femtosecond laser sources, and to optimize and update both lasers for application in nonlinear microscopy.

2. To evaluate the sensitivity and utility of TH microscopy to sources of contrast encountered in high quality oxide thin films starting from the time of deposi-

tion and continuing through exposure to high fluence laser radiation and the creation of permanent material modification.

3. To investigate FWM microscopy signals as a function of the inter-pulse time delay between two excitation sources and to evaluate the usefulness of such signals for characterizing the dominant resonant response of the sample under study.

4. To develop a genetic algorithm capable of optimizing nonlinear optical signals by interfacing with a spatial light modulator for temporal waveform synthesis of femtosecond regime optical pulses.

1.3 Thesis outline

The main topic of this thesis is the characterization of material properties via third-harmonic (TH) and four-wave mixing (FWM) microscopy. This topic is discussed for three applications: (1) TH evaluation of dielectric oxide thin films used in fs laser-induced damage threshold studies. (2) A two pulse method for determining the dominant resonant process present in FWM interactions. (3) A genetic algorithm to optimize nonlinear signal generation via temporal waveform synthesis.

Chapter 2 conveys several details of nonlinear optics relevant to this thesis. We begin with an introduction to nonlinear microscopy by outlining nonlinear signal generation in tandem with mathematical and photon energy-level descriptions of several nonlinear processes highlighted throughout this manuscript. Subsequently, we recall the merits of i) TH with circularly polarized illumination (THCP) for isolating optical signals from anisotropic media and ii) polarization control in FWM microscopy for isolating optical signals from resonant media. THCP is used extensively for investigating inherent and induced anisotropy of the oxide thin films in Chapter 4. The

FWM polarization control scheme is implemented to confirm the results of modeling resonant FWM signals in Chapter 5.

Chapter 3 highlights the optimization of two preexisting femtosecond laser sources, a titanium sapphire oscillator (Ti:S) and an optical parametric oscillator (OPO) for application to nonlinear microscopy. The Ti:S previously exhibited double pulse output where normally the repetition rate of the laser would prescribe only one pulse. Such pulse behavior is undesirable in that it decreases the peak intensity of the laser output and weakens subsequent nonlinear signal generation. Following the determination of a suitable replacement for the outcoupler and pump focusing lens, the Ti:S output power, spectral bandwidth, pulse duration and pulse behavior are all improved. Careful alignment of the crystal position and end mirror also enable increased modelocking stability. These improvements prove to be critical for enabling sensitive measurements at the detection limit of our TH microscope. The OPO spatial mode output is improved from $\mathrm{TEM}_{0,n}$, where routinely $n > 4$, to $\mathrm{TEM}_{0,0}$ facilitating the removal of an intracavity knife's edge which results in nearly doubled output power.

The measurements in Chapter 4 center upon TH microscopy investigation of dielectric oxide thin films. The study of such films holds great interest for researchers involved in fs laser-induced damage threshold (fs LIDT) studies, film deposition, and micro- and nano-patterning with fs pulses. We first characterize the TH microscope itself by determining the spatial resolution and minimum polarization ellipticity in the sample plane. The polarization ellipticity is of interest because of its role in limiting the microscope's sensitivity to anisotropy in the case of THCP imaging. Prior to interrogation of thin films we examine THCP sensitivity to both colloidal gold nanoparticles and nanoindentations in fused silica. Respectively, these measurements serve to estimate the minimum size of detectable anisotropy and to confirm imaging sensitivity to induced material strain, both of which hold importance

for fs LIDT studies. Subsequent sections consider high quality thin films exposed to high fluence laser radiation for cases both below and above damage threshold. From these exposures we compare TH imaging results with conventional far field microscopy techniques commonly employed to study laser damage in thin films. For exposures above damage threshold, THCP imaging is shown to exhibit significantly larger dynamic range and is able to uniquely identify modification in the remaining material. Additionally, TH with linearly polarized illumination (THLP) of the same exposures shows a singular potential to quantify the depth of material removal. For exposures below damage threshold, THCP alone produces high contrast images of induced material anisotropy. This confirms the presence of a previously speculated long lived material change prior to the formation of optical damage. A section is dedicated to TH investigation of nascent thin films. In these films, features unique to THCP imaging are compared with several types of data and are found to correlate with strain in the film. An additional section presents the observation of a reversible material change in a film of relatively high absorption at laser fluences achievable with our TH microscope. Such an effect highlights the value of TH microscopy for on-line monitoring of transient material effects during both fs LIDT studies and routine operation of high energy laser systems.

In Chapter 5, both of the lasers optimized in Chapter 3 are implemented for two color FWM microscopy. Two color illumination generates two spectrally resolved FWM signals in the visible and IR respectively. The primary focus of this chapter is the analysis of these two FWM microscopy signals as they depend on the inter-pulse time delay between the two illumination sources. The effect of resonant media on the two FWM signals is monitored for several solvents (methanol, ethanol, propanol, butanol, hexane). These inter-pulse delay scan measurements reveal a delay separation between the visible and IR FWM signal peaks. This delay separation is shown to be material specific. It is hypothesized that the delay separation between visible and IR FWM signals is due to the presence of a resonant material process with charac-

teristic time probed by the two fs sources. To confirm this hypothesis we implement mathematical modeling of inter-pulse delay scan measurements with the inclusion of resonant processes for: visible FWM signals produced by coherent anti-Stokes Raman scattering (CARS) and visible stimulated parametric emission (SPE), and IR FWM signals produced by coherent Stokes Raman scattering (CSRS) and IR SPE. The results of modeling suggest that inter-pulse delay scan measurements probe a characteristic vibrational dephasing time in the CARS process. This result is further confirmed by repeating inter-pulse delay scan measurements while implementing a polarization control setup for suppression of resonant CARS signals.

Chapter 6 discusses the development and application of a genetic algorithm implemented in LabVIEW to interface with a spatial light modulator (SLM) and to optimize nonlinear signal generation via temporal waveform synthesis. Two versions of the algorithm are presented: one with fully independent control of the SLM pixels and another where the values of the pixel mask are determined by implementing polynomials up to order nine. Preliminary results confirm the ability to optimize SH and TH nonlinear signals. For benchmarking, we demonstrate that our results with SH signals compare favorably with a commercially available software for generating bandwidth limited pulses based on the phase retrieval technique multiphoton intrapulse interference phase scan (MIIPS). Subsequent sections feature optimization of TH microscope signals for samples of bulk fused silica and gold islands.

Chapter 7 summarizes the work presented in this thesis and discusses the potential implications for future work.

Chapter 2

Nonlinear Microscopy

The goal of this chapter is to introduce the reader to a few key features of nonlinear optical signals which make them attractive for microscopy applications. These features can be characterized as either generic ⇒ features present for all nonlinear processes (i.e. 3-dimensional sectioning), or specific ⇒ features present for a given process (i.e. third-harmonic generation (THG) at interfaces). This chapter includes an overview of several key nonlinear processes referenced throughout this manuscript, as well as specifics of relevant theory found useful in the subsequent chapters' applications.

2.1 Nonlinear vs. Linear signals

In the case of linear optics, signals derive their source from a material polarization, P, induced by the incident electric field, E, where the constant of proportionality between the two is given by the linear susceptibility, $\chi^{(1)}$. This is expressed as

$$P(t) = \chi^{(1)} E(t) \tag{2.1}$$

where, for simplicity, we temporarily omit the vector nature of P and E as well as the tensor nature and frequency dependence of $\chi^{(1)}$. In a generalization of Eq. (2.1) for the case of nonlinear optics, P can be expanded in a power series of the incident electric field and may be written as

$$P = \chi^{(1)}E + \chi^{(2)}E^2 + \chi^{(3)}E^3 + ... = P^{(1)} + P^{(2)} + P^{(3)} + ... \tag{2.2}$$

where P and E implicitly depend on time. While always valid in the frequency domain, Eq. (2.2) may be considered valid in the time domain only for the case of instantaneous response in a material without loss or dispersion.

Nonlinear optical signals derive their source from the induced material polarization P. Considering that the optical signals we collect are time averaged due to finite electronic instrument response times, detection of the nth-order nonlinear signal may be written as

$$S^{(n)} \propto \int \left[P^{(n)}\right]^2 dt = \int \left[\chi^{(n)}E^n\right]^2 dt. \tag{2.3}$$

A closer look at Eq. (2.3) reveals the important facts that nth-order nonlinear signals scale proportional to I^n, where I is the instantaneous optical intensity, and probe a spatially localized $\chi^{(n)}$. A geometrical example elucidates why this is so important for nonlinear microscopy.

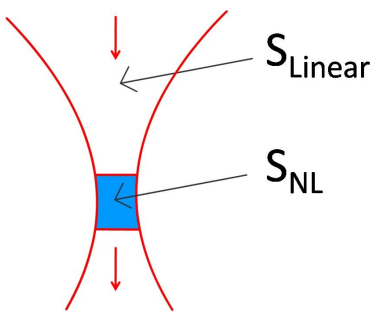

Figure 2.1: Optical signals produced near the focus of a Gaussian beam.

Consider the focused Gaussian beam shown in Fig. 2.1. The resultant linear signals scale with optical power and are generated throughout the extent of the beam, while nth-order nonlinear signals scale as I^n, and are dominantly generated in a region around the focus of the beam. The axial extent of this region is approximately the confocal parameter of the beam, which along with the beam waist estimates the ellipsoidal volume of signal generation. Approximating this volume as a point, we see that adjacent points begin to map out a distribution of $\chi^{(n)}$ in 3-dimensional (3D) space. This is fundamental to nonlinear imaging microscopy and may be expressed mathematically as

$$S^{(n)}(x,y,z) \propto \int \left(\chi^{(n)}(x,y,z)E^n\right)^2 dt. \tag{2.4}$$

Nonlinear signal generation is inherently applicable to 3-dimensional imaging and relies on point by point image construction. Typically, a computer is used to coordinate sample scanning and data collection.

2.2 Nonlinear processes for microscopy

Figure 2.2 shows the photon energy-level diagrams[†] of second-harmonic generation (SHG), sum frequency generation (SFG), third-harmonic generation (THG), and four-wave mixing (FWM), which are referenced throughout this manuscript. These diagrams indicate a transfer of energy from incident photons to a signal photon that occurs as a single quantum-mechanical process. For the process of THG, three fundamental photons are annihilated and simultaneously one photon is created with three times the energy. The solid line indicates a ground state while the dashed lines represent virtual levels. For the experiments that follow, the center wavelengths,

[†]This is the naming convention used in Boyd [15].

λ_c, of the observed incident lasers and the predicted signal fields are presented in Table 2.1. Although the titanium sapphire oscillator (Ti:S) and optical parametric oscillator (OPO) both are tunable laser sources, this table includes only the center wavelengths most commonly implemented for each.

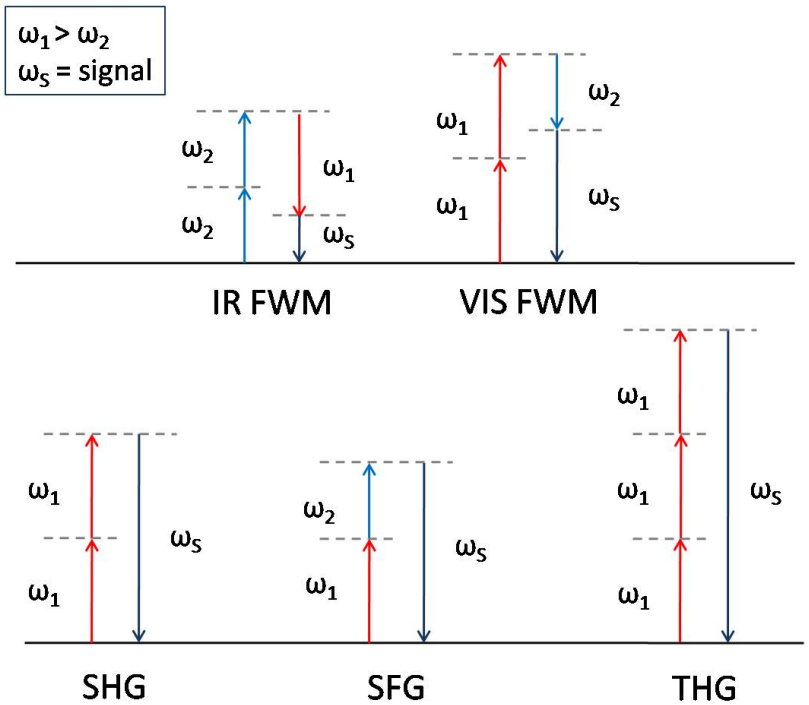

Figure 2.2: Photon energy-level diagrams corresponding to SHG, SFG, THG, visible FWM and infrared FWM.

source or process	Ti:S	OPO	SHG Ti:S	SHG OPO	SFG	Ti:S THG	IR FWM	Visible FWM
$\lambda_c(nm)$	787	1025	394	513	445	262	1469	639

Table 2.1: Central wavelengths of Ti:S and OPO laser sources as well as resulting SHG, SFG, THG, IR FWM, and Visible FWM optical signals.

When considering the efficiency of nonlinear signal generation, the induced material polarization must follow from processes where both energy and momentum are

conserved. However, meeting these fundamental requirements alone does not necessitate efficient signal generation. Often, the geometry of both the nonlinear material and the focusing conditions plays a defining role in nonlinear signal generation. For instance, it is well known that SH signals are generated only in noncentrosymmetric media [15]. For that reason, SHG is often used in combination with other imaging processes to reveal areas of noncentrosymmetric crystallinity, particularly in biological samples [64]. Less commonly known are the parameters effecting TH signals. However, since $\chi^{(3)}$ is non-vanishing for all materials, TH is of great interest for probing material characteristics.

Consider the case for efficient THG. Equations (2.5) and (2.6) express energy conservation and momentum conservation respectively, where ω_1 is the frequency of the incident field, ω_s is the frequency of the signal field and the k_i indicate momentum vectors for the four photons involved in this process.

$$\hbar\omega_s = \hbar 3\omega_1 \tag{2.5}$$

$$\Delta k = \vec{k}_1 + \vec{k}_2 + \vec{k}_3 - \vec{k}_4 = 0 \tag{2.6}$$

In order to achieve a maximal optical intensity and thereby the largest nonlinear signal, we require focused laser beams. Figure 2.3 illustrates how the momentum vectors with a positive wave mismatch can lead to efficient THG in the focus of a Gaussian beam. For a collimated Gaussian beam, the difference between the sum of incident momentum vectors and the signal momentum vector, the so-called phase mismatch, is required to be positive, $\Delta k > 0$, so that upon focusing (which results in an angular spread of momentum vectors), $\Delta k = 0$ and THG is allowed by momentum conservation. Obviously a positive phase mismatch is desirable to enable efficient TH signal generation in the focus of a Gaussian beam, yet, one more condition must be satisfied in order to produce net TH signals. For a linearly polarized focused Gaussian beam in an isotropic bulk media, the TH generated before and after the beam waist destructively interfere, resulting in zero net THG [25].

However, when axial symmetry is broken by either an interface or an anisotropic media, TH signals are generated efficiently [65, 18]. In fact, the same effect occurs for all higher order odd-harmonic nonlinear signals. As a classic illustration of exploiting this behavior for imaging, TH microscopy is used to create high contrast images of thin cell membranes without the need for staining.

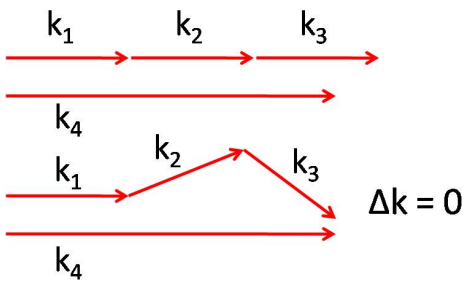

Figure 2.3: Momentum vector diagrams for THG. Identical amplitude incident (k_1, k_2, k_3) and signal (k_4) momentum vectors for two distinct cases. Above: incident momentum vectors in a collimated Gaussian beam. Below: the same beam is focused resulting in an angular spread of momentum vectors.

Using the two examples of SHG and THG in review, if one were to simultaneously image a sample by detecting SHG and THG, the collected signals would construct a 3D image of both noncentrosymmetric crystallinity and interfaces that pass through the focal volume of the incident beam. Stated another way, the image would partially map a distribution of $\chi^{(2)}(x, y, z)$ and $\chi^{(3)}(x, y, z)$ in the sample.

2.2.1 Third-harmonic applicability to thin films

As just mentioned, TH optical signals may be generated efficiently by inserting a material interface into the focal volume of a linearly polarized focused beam. While noting that this effect primarily relies upon breaking the axial symmetry required for destructive interference of TH signals, we have not specifically mentioned where the majority of signals are generated. In general, one may calculate the generated

TH field as a function of axial position, z, with Eq. (2.7) [27],

$$E_{3\omega}(z) = \frac{3i\omega\chi^{(3)}E_{\omega}^{3}}{2cn_{3\omega}} \int_{-\infty}^{z} \frac{e^{i\Delta k z'}}{[1 + i(z'/z_0)]^2} dz' \tag{2.7}$$

where c is the speed of light, z_0 is the Rayleigh range of the focus, Δk is the cumulative phase mis-match and $\chi^{(3)}$ and $n_{3\omega}$ represent the third-order susceptibility at the fundamental frequency and the index of refraction at the TH frequency for the material involved.

Of particular interest for application in Chapter 4, we desire to know the dominant source of TH signals produced when a thin film on a substrate is present in the focal volume of the TH microscope. One of our collaborators, who has developed a sophisticated model based on Eq. (2.7) to account for spherical aberration and clipping of the incident beam by a focusing objective, has kindly provided Fig. 2.4 for inclusion here. This phasor diagram plots the real and imaginary parts of the generated TH field as a function of z for a typical HfO_2 film (200 nm) on fused silica substrate. Clearly, the total generated field ($E_{3\omega}$) is dominated by the contribution from the film alone ($E'_{3\omega}$). In general, the relative contribution from an arbitrary thin film must be confirmed on a case by case basis. However, for the HfO_2 (hafnia) and Sc_2O_3 (scandia) films of thickness 100-200 nm on fused silica substrates which are interrogated in Chapter 4, the signal from the film is expected to dominate the total signal [66]. This allows us to interpret TH signals with the appropriate source in mind.

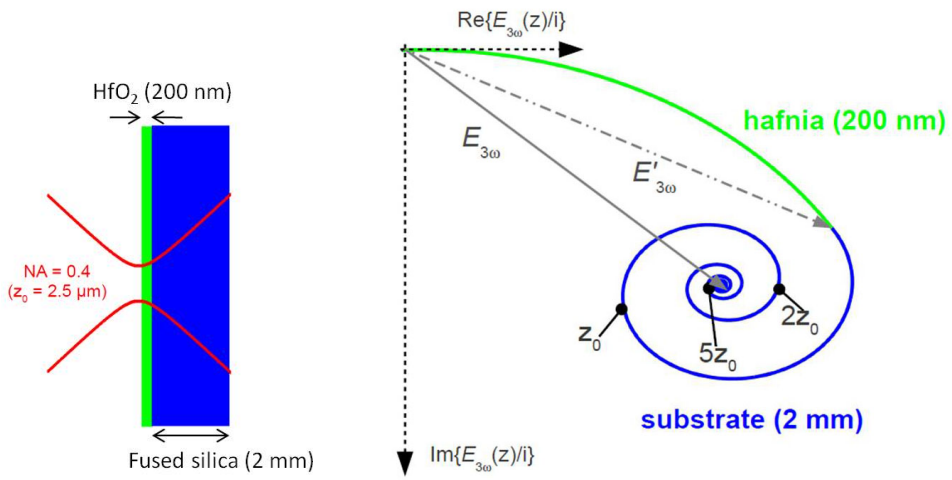

(a) (b)

Figure 2.4: (reproduced courtesy of Cristina Rodriquez[66]) Calculated phasor diagram of the net TH field generated for a hafnia thin film on fused silica substrate as a function of position in the propagation direction.

2.2.2 Implications of third-harmonic generation with circularly polarized light

From Section 2.2, we know that TH microscopy is typically used to image near interfaces. However, by implementing circularly polarized illumination, TH microscopy is readily extended to further isolate the source of TH signals. TH signals generated by circularly polarized illumination are generated from anisotropic features alone, whether near a material interface or deep within the bulk. Immediately, we see that third-harmonic with circularly polarized illumination (THCP) is innately useful for eliminating background optical signals in two ways: i) suppression of signals from isotropic media, ii) suppression of signals originating from interfaces alone. Both of these together make THCP readily applicable to nearly background free imaging of anisotropic anomalies in otherwise highly isotropic thin-film/substrate combinations.

To understand why THCP is sensitive to anisotropic features alone, first consider

Eq. (2.2). Recall that P is correctly written as a tensor equation to account for electric field polarization and anisotropic susceptibilities. For third-order polarization in the i direction (x, y, z coordinate axes) with D distinct permutations of the input field frequencies $(\omega_o, \omega_n, \omega_m)$, $P^{(3)}$ may be written generally as [15]

$$P_i^{(3)}(\omega_o + \omega_n + \omega_m) = D\Sigma_{jkl}\chi_{ijkl}^{(3)}(\omega_o + \omega_n + \omega_m)E_j(\omega_o)E_k(\omega_n)E_l(\omega_m) \tag{2.8}$$

where the input frequencies are arbitrary and may possess either positive or negative sign. Now considering the case of THG ($\omega_o = \omega_n = \omega_m = \omega$) and an isotropic material, Eq. (2.8) may be rewritten as

$$P_x^{(3)}(3\omega) \propto \chi_{xxxx}^{(3)}E_xE_xE_x + \chi_{xyyx}^{(3)}E_yE_yE_x + \chi_{xyxy}^{(3)}E_yE_xE_y + \chi_{xxyy}^{(3)}E_xE_yE_y. \tag{2.9}$$

We have assumed input fields in the x and y direction so that $E_z = 0$. Accounting for just the absolute equality of terms in isotropic media ($\chi_{xxxx}^{(3)} = \chi_{yyyy}^{(3)}$, etc.), the sum of terms in Eq. (2.8) is readily expressed by only the four terms remaining in Eq. (2.9) [15, 67]. In addition, we now consider the effects of a circularly polarized input field vector, $E = E_x + E_y = E + iE$ where $E_y = iE$. Noting that $(iE)^2 = -E^2$, evaluation of Eq.(2.9) yields

$$P_x^{(3)}(3\omega) \propto \chi_{xxxx}^{(3)}E^3 + E^3\left[-\chi_{xyyx}^{(3)} - \chi_{xyxy}^{(3)} - \chi_{xxyy}^{(3)}\right]. \tag{2.10}$$

However, the remaining four terms are not independent of one another. For isotropic media, $\chi_{xyyx}^{(3)} = \chi_{xyxy}^{(3)} = \chi_{xxyy}^{(3)} = \frac{1}{3}\chi_{xxxx}^{(3)}$ [67] and Eq. (2.10) becomes

$$P_x^{(3)}(3\omega) = 0. \tag{2.11}$$

Starting with Eq. (2.8) and using the same arguments, we reach the same result for the other $P_i^{(3)}(3\omega)$. Solving Eq. (2.8) generally for circularly polarized light, we find that TH signals are not generated in isotropic media. Applied to imaging, THCP signals indicate regions with anisotropy in $\chi^{(3)}$ where the isotropy condition $\chi_{xyyx}^{(3)} = \chi_{xyxy}^{(3)} = \chi_{xxyy}^{(3)} = \frac{1}{3}\chi_{xxxx}^{(3)}$ no longer holds. THCP previously has been implemented to image gold nanorods and birefringent biological specimens and to differentiate sub-domains of anisotropy [27, 18, 37].

2.2.3 Optical isolation of resonant four-wave mixing signals via polarization scheme

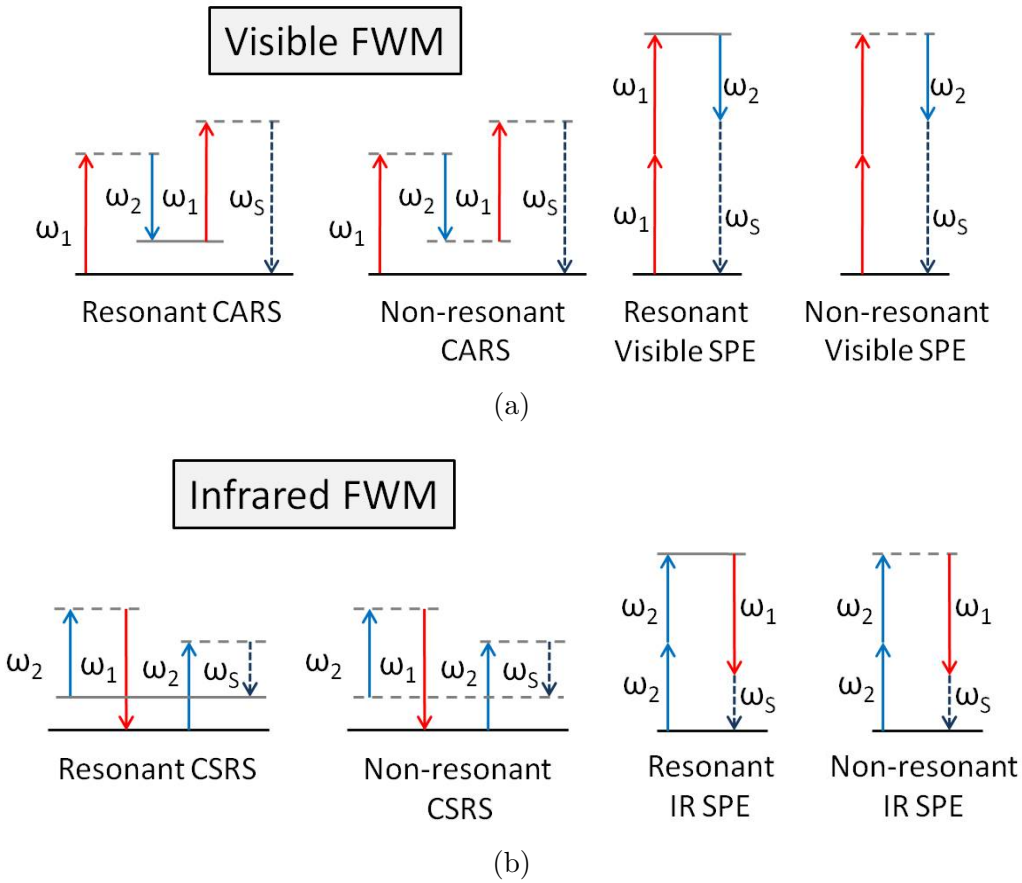

Figure 2.5: Resonant and non-resonant FWM signal processes which result in identical signal frequencies (a) in the visible and (b) in the infrared. Dashed lines indicate virtual energy levels. Solid lines represent real energy levels.

The energy level diagrams of Fig. 2.2 illustrate how sample illumination with the two laser sources implemented in this work leads to the generation of two FWM signal frequencies, one in the visible and one in the IR. However, what is not conveyed in these simple diagrams is that each signal may be generated by multiple processes within a material. Figure 2.5 shows how several processes, both resonant and non-resonant with energy levels in the sample, may contribute to the total signal at a

given frequency. In addition to CARS and CSRS, we now include stimulated parametric emission (SPE) processes in our discussion of FWM. Since FWM microscopy with chemical specificity relies upon resonant signals to enhance imaging contrast, suppressing background signals generated from nonresonant interactions represents a common obstacle in the field. Often, problems arise when the percentage of resonant molecules is small enough that the contribution from nonresonant interactions dominates the total signal. Several techniques have been developed to isolate resonant FWM signals. For the work in Chapter 5 we make use of a polarization control technique to isolate resonant IR SPE signals.

The development of the IR SPE polarization scheme presented here followed from previous work with CARS. CARS is a classic example of microspectroscopy where tunable laser sources allow molecular vibrational resonances to be probed. Groundwork was laid when polarization CARS (P-CARS) spectroscopy was first demonstrated in the late 1970's as a way to isolate resonant CARS signals [46] and enhance the detection of weak Raman active vibrational modes in benzene. Polarization CARS later was extended to microscopy and was demonstrated first as a means of enhancing vibrational contrast of the protein amide I band within unstained epithelial cells [47]. In analogous fashion to P-CARS, an IR SPE polarization scheme was developed for microscopy with the capability to isolate resonant IR SPE signals corresponding to electronic material resonances [51]. These previous works all took advantage of isolating the desired FWM signal by suppressing the relatively large nonresonant contribution at identical signal wavelength. Here we also make the observation that isolating IR SPE signals with a polarization scheme may simultaneously suppress resonant visible FWM signals corresponding to CARS.

The following explanation of the IR SPE polarization scheme proceeds from the derivations in references [46, 47, 51]. Isolation of resonant IR FWM signals is possible by polarization control when considering that the third-order material polarization

for IR FWM (cf. Eq. (5.8)) may be decomposed into contributions from nonresonant and resonant processes.

$$\vec{P}^{(3)} = \vec{P}_{NR} + \vec{P}_R \tag{2.12}$$

For linearly polarized input fields E_2 (OPO) and E_1 (Ti:S) separated by angle ϕ as shown in Fig. 2.6, the x and y components of P^{NR} may be written as

$$P_x^{NR} = 3\chi_{xxxx}^{NR} E_2^2 E_1^* \cos\phi \tag{2.13}$$

$$P_y^{NR} = 3\chi_{yxxy}^{NR} E_2^2 E_1^* \sin\phi \tag{2.14}$$

where recalling the notation for tensor susceptibilites, χ_{yxxy}^{NR} is the nonresonant third-order susceptibility produced in the y direction (cartesian coordinates) for incident fields in the x, x and y directions. In the same way, the x and y components of P^R may be expressed as:

$$P_x^R = 3\chi_{xxxx}^{R} E_2^2 E_1^* \cos\phi \tag{2.15}$$

$$P_y^R = 3\chi_{yxxy}^{R} E_2^2 E_1^* \sin\phi. \tag{2.16}$$

The value of the third-order susceptibility for nonresonant processes, χ^{NR}, is approximated to be real and frequency independent. Therefore the sum of x and y components of P^{NR} leads to a linearly polarized nonresonant signal field, $E_{S,NR}$, oriented at angle α with respect to E_2. In the presence of material resonance, the third-order susceptibility, χ^R, is complex and frequency dependent. In light of this, we may consider the sum of Eqs. (2.15) and (2.16) to be analogous to the sum of two fields oscillating with the same frequency but different amplitude. P^R then possesses elliptical polarization. The FWM signal field generated by the sum of P^{NR} and P^R, $E_{S,total}$ of Fig. 2.6, then also must be elliptically polarized. Immediately, we see that detection of optical signals perpendicular to the orientation of $E_{S,NR}$ results in signals that theoretically depend on P^R alone. However, in practice there always exists

some nonzero extinction ratio for linearly polarized light due to depolarization, and detection of some nonresonant signals in the perpendicular direction is unavoidable. Here, the dominant sources of depolarization are expected to be uncompensated birefringence in the optics due to broad bandwidth pulses and polarization scrambling for tight focus conditions [47]. Considering Eqs. (2.13)-(2.16) along with the nonzero extinction ratio r of P^{NR}, we can deduce the conditions that optimize the contrast ratio of signals due to P^{R}.

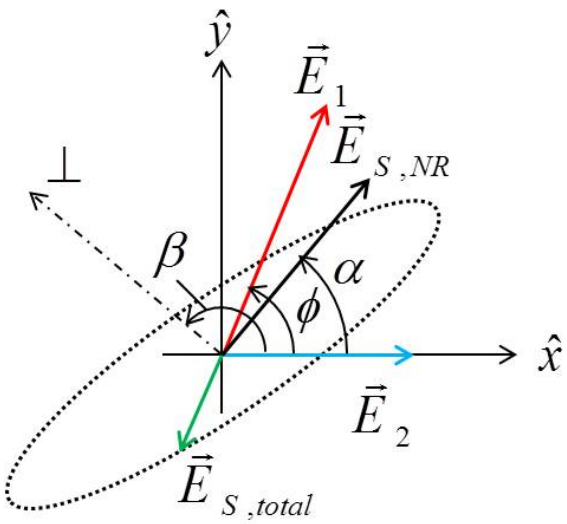

Figure 2.6: FWM polarization scheme for resonant signal isolation. Linearly polarized incident fields, E_2 and E_1, result in elliptically polarized signal, $E_{S,total}$, with a linearly polarized component exclusively due to nonresonant processes, $E_{S,NR}$.

For many materials, the ratio of the two remaining nonzero elements of the susceptibility tensor follows from Kleinman symmetry [7] as

$$\rho_{NR} = \chi^{NR}_{yxxy}/\chi^{NR}_{xxxx} = 1/3. \tag{2.17}$$

Noting that

$$\tan\alpha = \rho_{NR}\tan\phi = 1/3\tan\phi, \tag{2.18}$$

the total expression for P^{NR} with linear polarization at angle α is given by

$$P^{NR} = 3\chi^{NR}_{xxxx} E_2^2 E_1^* \cos\phi / \cos\alpha. \tag{2.19}$$

The resulting (background) linearly polarized nonresonant contribution to the total signal may be blocked by placing a polarization analyzer in the optical detection path perpendicular to $E_{S,NR}$ making angle β with respect to E_2. The resonant contribution in the perpendicular direction is

$$P_\perp = 3E_2^2 E_1^* \chi^R_{xxxx}(\cos\phi \sin\alpha - \rho_R \sin\phi \cos\alpha) \tag{2.20}$$

where $\rho_R = \chi^R_{yxxy}/\chi^R_{xxxx}$. Then assuming the extinction ratio is r for the nonresonant signal, the contrast ratio for resonant signals in the perpendicular direction may be written as

$$rP_\perp^2/(P^{NR})^2 = r(\chi^R_{xxxx}/2\chi^{NR}_{xxxx})^2(1 - \rho_R/\rho_{NR})^2 \sin^2 2\alpha. \tag{2.21}$$

To maximize the contrast ratio, we choose $\alpha = 45°$, and through Eq. (2.18) we determine the necessary angle between incident fields, $\phi \approx 71.6°$. This technique allows for the efficient isolation of resonant IR SPE signals.

Chapter 3

Femtosecond laser sources for microscopy

The nonlinear microscopy techniques detailed in the remainder of this thesis rely upon two preexisting femtosecond laser sources built by previous graduate students: a titanium sapphire oscillator (Ti:S) and an optical parametric oscillator (OPO) [68]. The goal of this chapter is to characterize regions of critical alignment in these Ti:S and OPO femtosecond laser sources, and to optimize and update both lasers for application in nonlinear microscopy. Specifically, we seek to instruct the reader as to how a systematic study of critical alignment regions in existing femtosecond laser sources may help to improve the respective source's i) output pulse behavior (single pulse instead of double pulse), ii) average power, and iii) output mode ($TEM_{0,0}$ desired). All of these improvements benefit nonlinear microscopy techniques.

The Ti:S output previously was characterized by a chaotic shift between single pulse and double pulse behavior on a timescale of minutes to hours. Compared to single pulse output, double pulse output has reduced peak intensity and thereby reduces any nonlinear signals produced by the beam. Single pulse output with im-

proved average power (peak intensity) is sought in order to increase nonlinear signal generation when the Ti:S is applied to nonlinear microscopy.

The OPO formerly required the use of an intracavity knife edge to enact $TEM_{0,0}$ transverse mode output. Using such a knife edge reduced the average output power by approximately half. A reduction in output power (peak intensity) of the beam leads to a reduction in any nonlinear signals produced by the beam. Therefore, a method for enacting $TEM_{0,0}$ output without a reduction in power is sought when the OPO is applied to nonlinear microscopy.

3.1 Overview of femtosecond laser sources for microscopy

Consider the case where nonlinear signals are generated in the diffraction limited focal volume of a nonlinear microscope. In order to yield a maximum nonlinear signal, one would choose an illumination source that exhibits high peak intensity and short wavelength (smaller diffraction limited spot size). However, nonlinear microscopy is typically transmission microscopy where the signal wavelengths are often harmonics of the excitation source. Requiring both sample transmission and detectability of harmonic signals, nonlinear microscopy is typically limited to source wavelengths in the visible and near-infrared (NIR). Additionally, it is clear that in order to avoid damage to the sample, the ideal illumination source would combine high peak intensity with modest average power in a high repetition rate ultrashort pulse laser. A survey of the literature reveals typical parameters for femtosecond sources often used in nonlinear microscopy, Table 3.1. The Ti:S and OPO parameters shown in Table 3.1 are for the sources used in the following work after optimization as detailed in the next two sections.

pulse source	Spectral range	Pulse duration	Mean Power or pulse energy	Repetition rate
Ti:S	770-800 nm	>45 fs	1.42 W	113.3 MHz
OPO	980-1300 nm	> 70 fs	<75 mW	113.3 MHz
Cr:LiSAF [69]	770-950 nm	> 9 fs	<100 mW	100 MHz
Cr:Forsterite [21]	1170-1345 nm	> 65 fs	≈ 200 mW	100 MHz
Er:Fiber oscillator [70]	1550 nm	50 fs	≈ 120 mW	37 MHz

Table 3.1: Comparison of optimized Ti:S and OPO to typical spectral range, pulse duration, mean power and repetition rate for several types of femtosecond sources often used in nonlinear microscopy .

3.2 Optimization of femtosecond titanium sapphire oscillator

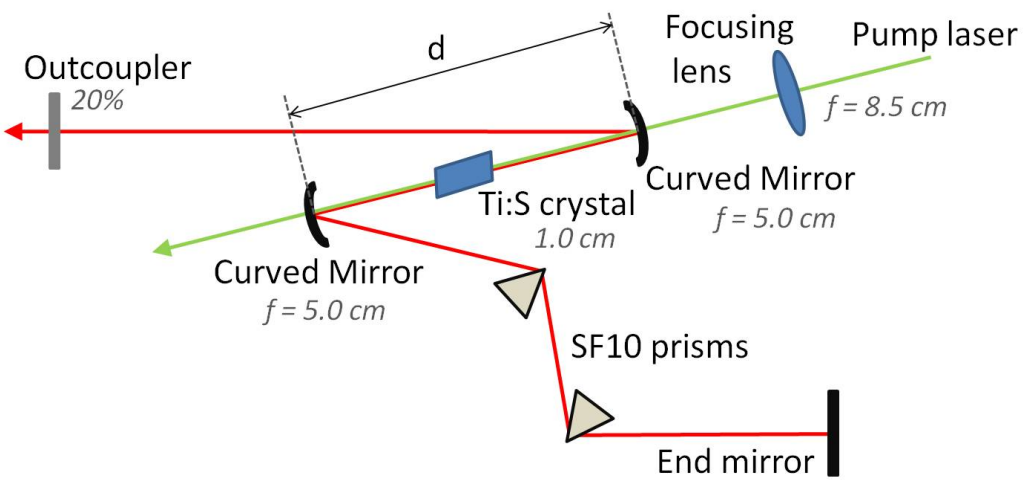

Figure 3.1: Layout of the Kerr lens modelocked Ti:S oscillator.

An diagram of the cavity layout of the asymmetric cavity Kerr lens modelocked Ti:S oscillator used throughout the work presented in this thesis is shown in Fig. 3.1. A 532 nm frequency doubled Nd:Vanadate laser (Coherent Verdi V-8, 7.00 W) pumps

a titanium doped sapphire crystal (10 mm length) which emits broadband fluorescence (700 - 1000 nm) peaked at 790 nm. The cavity is dispersion controlled via a prism pair (SF10) used to negate positive group velocity dispersion (GVD) introduced by the crystal and mirrors [71]. Pulses arise from fluctuations in the intracavity power and are selectively prefered for gain due to Kerr lensing in the crystal [72]. Following optimization, the result is a modelocked (19 nm bandwidth) train of pulses of 45 fs duration at 1.42 W average power and 787 nm central wavelength with a repetition rate of 113.3 MHz.

Owing to the nonlinear nature of both Kerr lensing and thermal lensing present in this type of oscillator, an analytical description of the cavity dynamics is abandoned in favor of numerical modeling which places two cavity modes, continuous wave (CW) and modelocked, in competition for gain [73, 74]. It is both observed and modeled [73] that for a Kerr lens modelocked laser with soft aperture, the modelocking process is most preferred near the center of CW stability regions of the laser. In an attempt to increase modelocking stability and output power, a systematic study of a few stability regions was undertaken.

Previously, our Ti:S oscillator displayed double pulse behavior, where the output pulse train is characterized by two pulses where normally (as prescribed by the repetition rate of the laser) there would be only one. Double pulse behavior reduces the peak intensity of the laser and thereby reduces subsequent nonlinear signal generation. For this reason, we sought to make the output behavior single pulse.

Double pulse modelocked output may indicate that the intracavity peak power of a single pulse exceeds the critical power of self focusing which can lead to pulse splitting [75]. One solution to this problem is to introduce an additional cavity loss by increasing the outcoupler transmission. If chosen correctly, the outcoupler may also lead to an increase in the average output power of the oscillator. The goal is to find an appropriate outcoupler that negates double pulse behavior while

increasing the modelocked power output. For outcouplers in the range of 13% to 25% transmission, the average power and pulse behavior of the Ti:S oscillator were observed for comparison and are plotted in Fig. 3.2. For a combination of single pulse modelocked output and increased average power, the original 13% outcoupler was permanently replaced with a 20% outcoupler. Note that after the 20% outcoupler was chosen, the pump focusing lens was changed, from f = 10 cm to f = 8.5 cm AR coated, in order to increase both the transmission of the pump laser through the lens and the fluence of the pump within the crystal. This yielded an increase in average CW and modelocked power and the output behavior remained single pulse.

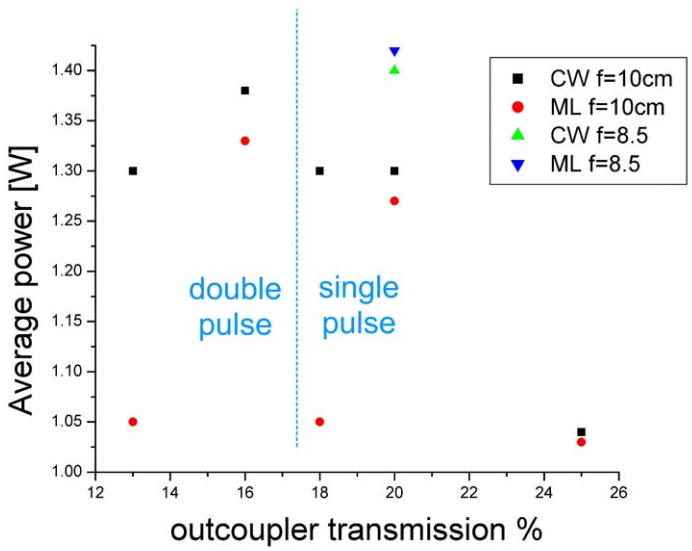

Figure 3.2: CW and modelocked average power of the Ti:S oscillator for 13%, 16%, 18%, 20%, 25% transmission outcouplers. Also shown is the CW and modelocked average power for the 20% outcoupler achieved after changing the pump focusing lens from f = 10.0 cm to f = 8.5 cm.

Once single pulse output behavior was achieved, we sought to optimize the modelocked output power of the oscillator by investigating two critical alignment regions. First, the distance d between folding mirrors (cf. Fig. 3.1) was adjusted over a few mm while monitoring the CW power. Such an alignment is accomplished by

translating together the crystal, second folding mirror (curved mirror nearest prisms) and pump focusing lens. This keeps the focal volume of the pump at a constant position in the crystal and maintains a constant distance between the focusing lens and the mirror being moved. This also requires that the entire cavity be realigned for maximum CW power for each step in d. The results with a 20% outcoupler are shown in Fig. 3.3a. Optimum modelocking stability is achieved for $d = 111.75$ mm[†], which is slightly detuned from maximum CW power in this stability region. The need for this detuning likely indicates the effect that Kerr lensing (arising from pulsed behavior) imposes on the stability of the cavity[76]. For a 16% outcoupler, Fig. 3.3b, the CW power has a maxima at the same position as that of the 20% outcoupler.

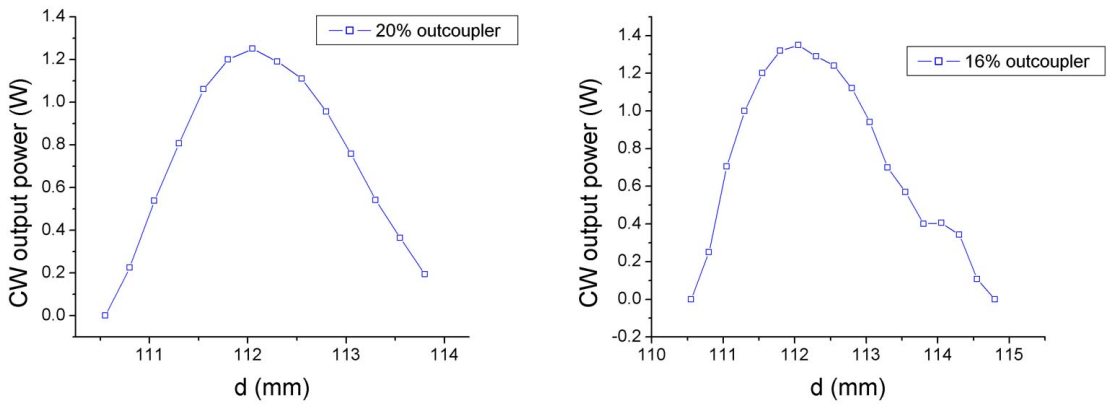

(a) (b)

Figure 3.3: CW power versus the distance, d, between folding mirrors in the Ti:S cavity for (a) 20% outcoupler, (b) 16% outcoupler.

A second alignment region of interest depends on the horizontal alignment of the end mirror. From Fig. 3.1 we see that the spectral components of the laser arrive with spatial separation on the end mirror. Ascribable to that fact, we find that fine alignment of the end mirror has an impact on both the overall power and

[†]Measured with a vernier caliper.

the center wavelength of the output pulses. To map this stability region, we first align the cavity for absolute maximum CW output power[†]. Next, the end mirror horizontal alignment knob is walked incrementally in one direction (clockwise or counterclockwise). For each incremental motion on the end mirror, the outcoupler is aligned for maximum CW power. If modelocking is observed, the power and spectrum are recorded. From this data, Fig. 3.4, we find that for the most stable modelocking ($>$ 24 hours duration), the modelocked average power (1.42 W) exceeds the CW average power (1.41 W). Experimentally, this stability region is observed to be by far the most useful for finding the highest power stable modelocking behavior of the oscillator. This may be owed to the fact that alignment of the end mirror in the horizontal direction finely tunes the cavity alignment to a specific wavelength range in the spatially separated spectrum incident upon it. The assumption is that when this range is centered upon the minimum GVD wavelength[*] of the cavity, the highest modelocked power results. This same assumption motivates piezoelectric control of the end mirror in the horizontal direction for phase stabilized laser oscillators [77, 78].

In summary, an existing Ti:S oscillator has been improved by i) eliminating double pulse output by moving to a higher output coupler, and ii) mapping two stability regions which aid in finding the maximum power for stable modelocking. Additionally, mounts of both the second folding mirror and the focusing lens were replaced to improve mechanical stability. The net effects of these improvements can be found in Table 3.2. Highlights include the improved modelocking power, 1.35 - 1.42 W, and the elimination of double pulse behavior, which both lead to higher intensity applied to nonlinear microscopy. For reference, the output spectrum of the optimized Ti:S laser is presented in Fig. 3.5.

[†]This includes aligning the distance between folding mirrors, d.

[*]This amounts to fine tuning the GVD. GVD is primarily controlled by aligning the prisms and minimizing the pulse duration of the laser output as measured by a technique such as autocorrelation or FROG.

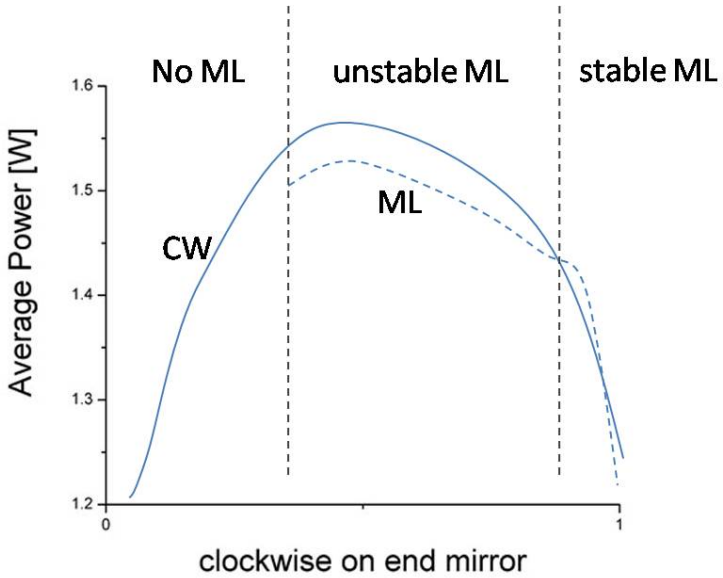

Figure 3.4: CW and modelocked power as a function of horizontal end mirror position. The laser is operated at 1.42 W ML in the stable ML region.

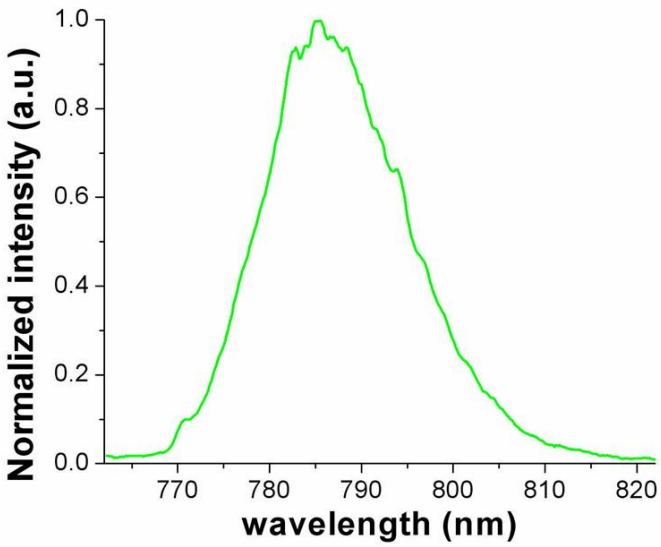

Figure 3.5: Typical spectrum of the Ti:S laser following optimization.

	Max Power CW (W)	Max Power ML (W)	Modelocked bandwidth (nm)	τ_p (fs)	λ_c (nm)	pulse behavior
before	1.50	1.35	16	70	785	chaotic single-double
after	1.57	1.42	19	45	787	single

Table 3.2: Ti:S oscillator characteristics before and after optimization.

3.3 Optimization of femtosecond optical parametric oscillator (OPO)

A layout diagram of the OPO is shown in Fig. 3.6. An extensive explanation of its construction and operation can be found in Dr. Xuejun Liu's dissertation [68]. The OPO is synchronously pumped (1.11 W) by the Ti:S source described in section 3.2, and yields a train of pulses with > 70 fs duration, < 75 mW average power at 1025 nm, and 113.3 MHz repetition rate. The cavity contains a prism pair (SF10) to compensate GVD in the cavity. A piezo stage finely controls the optical length of the cavity to match the repetition rate to that of the Ti:S. A knife is mounted on a vertical translation stage and can be inserted partially into the intracavity mode in order to control the output mode. A $TEM_{0,0}$ output mode is desirable in order to produce a circular spot with Gaussian transverse profile in the focus of a lens. Applied to microscopy, an incident $TEM_{0,0}$ mode then becomes important for achieving optimal transverse resolution of the microscope.

Previously, the OPO exhibited a propensity for spatial mode operation of $TEM_{0,n}$ (with n>4), when aligned for maximum power and maximum tuning range. By inserting the knife's edge into the intracavity mode, $TEM_{0,0}$ output could be achieved but at a cost of half the output power (i.e. 45 mW to 28 mW). A solution for achieving $TEM_{0,0}$ output without this reduction in power is desired. Knowing that higher order spatial modes often result from operating a cavity near instability, an assessment of cavity stability was required. The critical alignment proved to be the axial alignment of the end mirror. The output power and mode results for alignment of the end mirror in the axial direction (and subsequent alignment of the outcoupler to maintain cavity length) are shown in Fig. 3.7. The end mirror stage is kept at 11.28 mm to yield $TEM_{0,0}$ output. Indeed, the OPO was previously operating near cavity instability at 11.56 mm. The result is to provide $TEM_{0,0}$ output without a

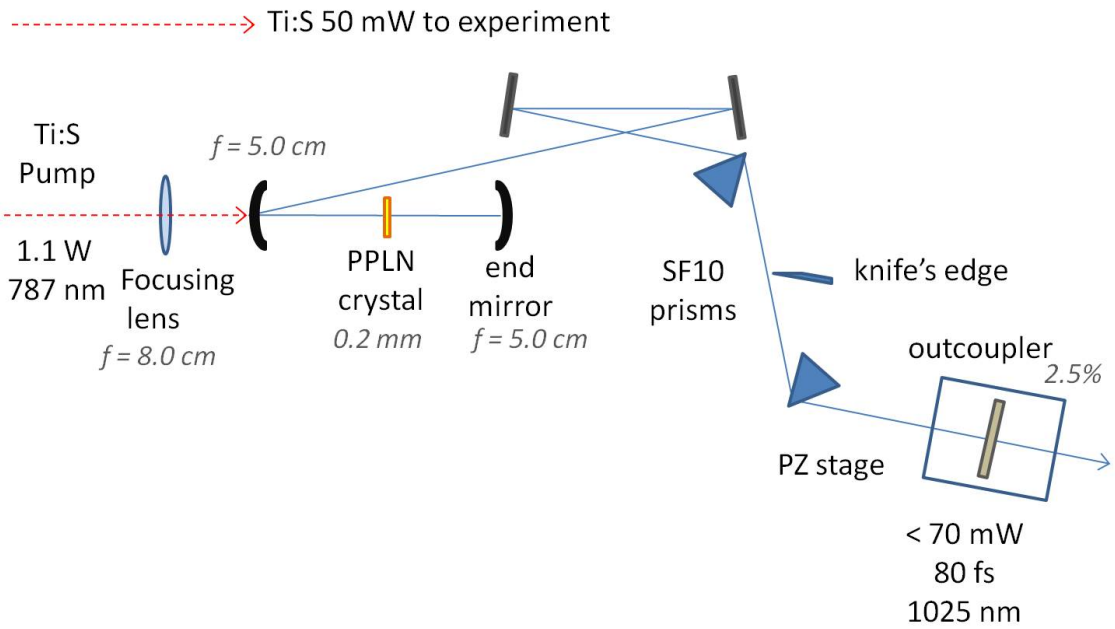

Figure 3.6: Layout of the femtosecond pulse OPO.

reduction in average power. This alignment may improve the output mode by virtue of overlapping, within the periodically poled lithium niobate (PPLN) crystal, the focus of the pump beam with that of the counterpropagating beam reflected by the end mirror. This is likely because the PPLN crystal is the only cavity component with structural variation in the vertical direction.

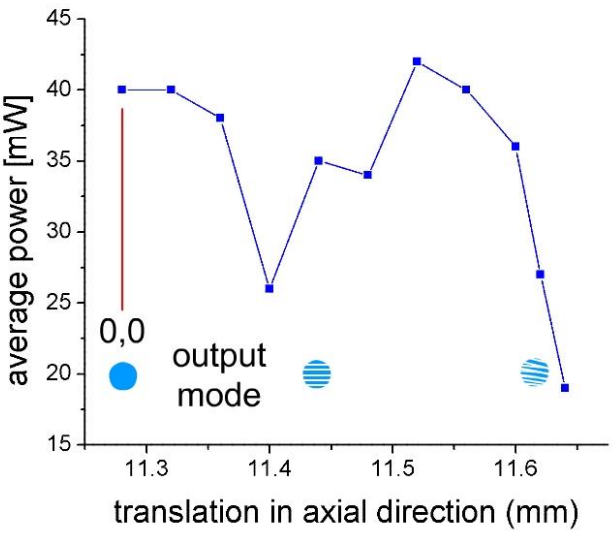

Figure 3.7: Output power and mode of the OPO as a function of end mirror position.

Chapter 4

Third-harmonic microscopy of transparent optical thin films

The goal of this chapter is to evaluate the sensitivity and utility of TH microscopy to sources of contrast encountered in high quality oxide thin films starting from the time of deposition and continuing through exposure to high fluence laser radiation and the creation of permanent material modification. As a scanning far-field method of imaging, TH microscopy represents a relatively fast and comparatively simple all-optical technique which provides information typically only accessible through more complex measurement techniques. Compared with such complex techniques, which generally provide information on a broad spatial scale, TH microscopy adds the capability of distinguishing spatially localized material characteristics.

4.1 Overview of thin film samples and laser damage studies

The next several decades certainly will be shaped on a global scale by advances in energy production, by the ubiquity of light-weight high-strength advanced materials and by the landscape of international defense. However, what may be overlooked today is the critical role played by high energy laser systems in facilitating progress in these areas and others. Indeed, the successes and failures of current projects such as the national ignition facility at Lawrence Livermore National Laboratory ($> 1.8\ MJ$), and the free-electron laser at Thomas Jefferson National Accelerator Facility ($> 14\ kW$) have direct implications for the viability of nuclear fusion reactors, carbon nanotube production and ship based missile defense systems. At present, these and other high energy laser systems are limited in part by the availability of optics capable of withstanding the immense laser fluences necessary to sustain high energy output. For this reason the study and improvement of coatings comprising these optics is paramount to the success of such high energy laser projects. Promising high damage fluence optical coatings are already made from dielectric oxide thin films, however improvement remains necessary if they are to support further advances in high energy laser applications. The characterization of such films via TH microscopy, with an outlook toward improvement, is the central topic of study for the remainder of this chapter. However, before considering the merits of TH microscopy, let us first examine a few fundamentals of laser damage studies that provide additional motivation for the work completed here with TH.

Femtosecond pulse laser-induced damage threshold (fs LIDT) studies represent a primary method for analyzing the optical quality of dielectric oxide thin films currently of interest for high fluence optical coatings (HfO_2, Sc_2O_3, Ta_2O_5, SiO_2, TiO_2). This reflects the fact that the quality of films produced by a variety of deposition

processes has reached a sufficiently high level that damage studies with femtosecond laser pulses are highly deterministic with respect to laser fluence. These studies thereby probe fundamental parameters of the films and provide crucial information concerning the mechanisms of damage. When considered together with data from optical microscopy, electron microscopy, atomic force microscopy, X-ray diffraction, absorption measurements and other methods of characterizing thin films, fs LIDT studies provide a wealth of information that when properly interpreted may help lead to the production of higher quality optical thin films.

The definition of optical damage in itself has been a matter of debate since the inception of optical damage studies with the advent of the first Q-switched lasers in the 1960s. Most generally, the damage threshold is defined to be the incident fluence of light for which either a) a minimum incremental amount of material (a single atom/molecule) is ablated from the material, or b) the material suffers a permanent change. In practice, the evaluation of either such definitions remains impractical and the damage threshold is often evaluated by observing a minimum incremental increase in scattering from the sample under study. It should be noted that this scattering method of evaluating the presence of optical damage has been applied throughout the work detailed here. In addition, since it is not clear that all types of permanent material modification effect the damage threshold of a material, we adopt the terminology of Mero[79], using the term "incubation" to refer to a laser-induced material change not yet resulting in macroscopic destruction of the optic. Though such incubation sites are of interest for the dire role they play in leading to catastrophic damage they remain ill-studied and poorly characterized. Historically, this is due in part to the lack of an appropriate method of interrogation. TH microscopy is presented here as one method that is well suited to interrogating such incubation sites. High quality films and their substrates are largely amorphous and are then assumed to display highly isotropic behavior. Therefore any laser-induced material modifications resulting in anisotropy are expected to be readily imaged via

TH microscopy with circularly polarized illumination as outlined in Section 2.2.2.

The formation of optical damage is thought to hinge upon the presence of a critical electron density, N_c, in the conduction band of the material under study [80]. This critical electron density corresponds to the density at which the plasma frequency of the material matches the laser frequency and signals the transition within the material from transparent to highly absorbing behavior. Compared to laser damage studies with pulses a few 10s of picoseconds and longer, which are dominated by thermal damage mechanisms (melting, vaporization, thermoelastic stress fracture), laser damage studies with femtosecond pulses rely upon the interplay of additional electronic damage mechanisms such as Coulomb explosion [81] and plasma formation [82]. Due to the complexity of the problem, fs LIDT studies abide mainly in the realm of empirical science. Even so, experiments and simulations agree that band gap, multi-photon absorption, avalanche ionization, native trap states, and laser-induced trap states (Fig 4.1) all play a role in determining the damage threshold of dielectric oxide films [28, 29, 30, 31, 32]. Thus, fs LIDT studies probe the population distribution of electrons within the specific energy band structure of thin film materials.

Interestingly, one major precipitate of fs LIDT studies is the observation of different damage threshold fluence values for single-pulse (F_1) and multiple-pulse (F_S) exposures of the same sample as shown in Fig. 4.2. The relationship $\mathrm{F}_S < \mathrm{F}_1$ is broadly interpreted to indicate a memory effect of the material. That is to say that the reason for a decreased damage threshold fluence under multiple pulse illumination relates to a material alteration caused by one pulse that persists until the arrival of the following pulse(s). In repetition, this cumulative effect lowers the damage threshold fluence of the sample. This effect is shown to be invariant for pulse repetition rates between 1 Hz and 1 kHz, indicating a fairly long lived material alteration. Indeed, it's possible that the material modification is permanent even for

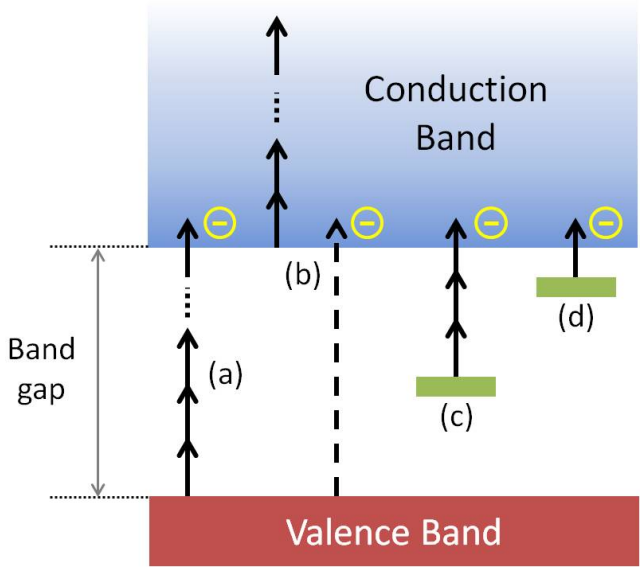

Figure 4.1: Four processes relevant to phenomenological modeling in fs LIDT studies that contribute to promotion of electrons to the conduction band: (a) multi-photon absorption, (b) avalanche ionization, (c) multi-photon absorption from a deep trap, (d) linear absorption from a shallow trap.

laser exposures prior to damage. If this is the case, traditional imaging techniques have failed to indicate its presence.

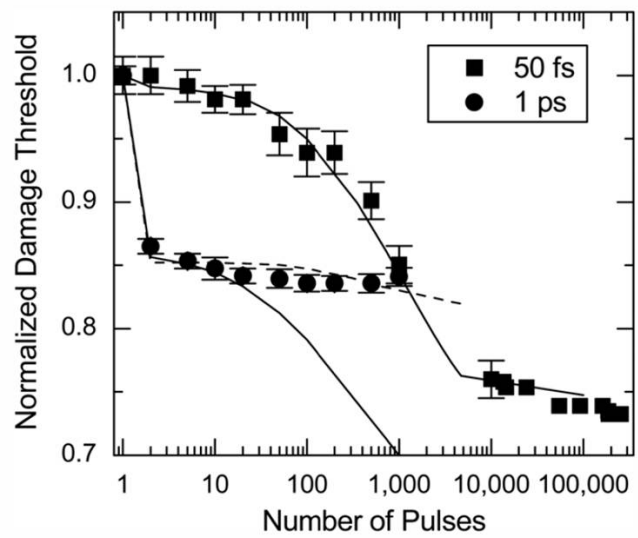

Figure 4.2: (Reproduced courtesy of Luke Emmert and Duy Nguyen[83]) Experimentally obtained damage threshold data normalized to the single-pulse value. Measurements are for HfO_2 film with two different pulse durations.

4.2 Experimental setup

The setup for TH microscopy is shown in Fig. 4.3. A Ti:S laser pulse train (787 nm, 45 fs, maximum 340 mW incident on focusing objective) propagates through a preexisting optical scanning section which enacts square raster-scanning in the focal plane of the focusing objective (Leitz Wetzlar, 20×, 0.4 NA). The Ti:S pulses are prechirped with a prism compressor [54, 71] so that a minimum pulse duration is achieved in the sample plane. As observed in Chapter 6 this minimum duration is not necessarily bandwidth limited. TH optical signals generated within the sample are gathered by a collection objective (OFR 20×, 0.4 NA, UV) which directs both the TH and linear optical signals to the detection path for spectral separation via dichroic mirror (HR 266 nm) and interference filter (Edmund Optics NT67-811 265 nm). TH signals are detected by a photomultiplier tube (PMT: Hamamatsu H10721-01) with variable gain. Simultaneously, reflection signals at 787 nm are detected via confocal

alignment to a single mode fiber coupled to an amplified silicon detector (Thorlabs PDA36A). The scanning section and data collection are coordinated via computer [84]. Insertion of a quarter-wave plate (QWP) (Casix zero-order 800 nm quartz-MgF_2) before the scanning section allows for adjustment between linear and circular polarization of the fundamental field in the sample plane. Careful alignment[†] of this QWP yields a TH signal originating in the focal volume where anisotropy in the material is the dominant source of contrast. Here the 0.4 NA focusing objective is used for the convenience of having a long working distance ($\approx$ 10 mm) and is necessary for working with thick samples.

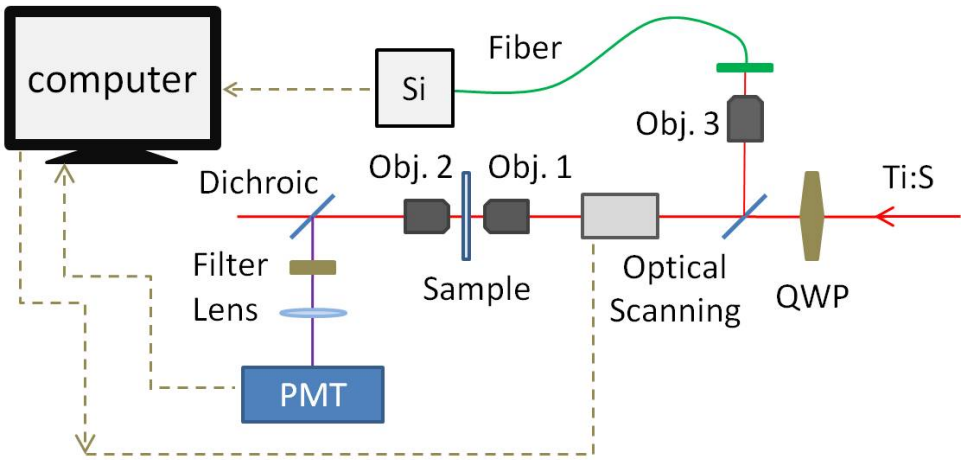

Figure 4.3: Diagram of the TH microscopy setup.

4.2.1 Spatial resolution of the TH microscope

The spatial resolution of this TH microscope defines the limits of accurately quantifiable spatial features in the captured TH and reflection images. For a radially symmetric beam, the resolution is defined in two spatial directions: transverse $\Rightarrow$ in the plane of the image, and axial $\Rightarrow$ perpendicular to the plane of the image. The

[†]High contrast imaging often requires QWP alignment within $\approx 0.1^\circ$ [27].

transverse resolution is estimated to be approximately the diameter of the spot size, twice the Gaussian beam waist, w_0.

$$w_0 = \frac{3\lambda_0}{2\pi NA} \tag{4.1}$$

The axial resolution is estimated to be approximately twice the Rayleigh range of the beam, $2\rho_0$ [12].

$$\rho_0 = \frac{n\pi w_0^2}{\lambda_0} \tag{4.2}$$

The measured values of axial and transverse resolution will differ from their estimates in part because of deviation from a perfect Gaussian beam profile in the focus of the microscope. Limited by the hard aperture of the focusing objective, a non-Gaussian diffraction pattern is present in the focal plane. Additionally, Eq. 4.1 assumes an infinitesimally thin lens without aberrations. Clearly, that is not the case here with a compound lens microscope objective.

Using the approximation given in Eq. (4.1) [85] for w_0 as a function of numerical aperture (NA), with NA = 0.4 and center wavelength λ_0 = 787 nm, we calculate $2w_0$ = 1880 nm = transverse resolution. Using Eq. (4.2) [86] where the index of refraction n = 1 for air, the center wavelength λ_0 = 787 nm, and the beam waist w_0 = 939 nm, we calculate $2\rho_0$ = 7.0 μm = axial resolution.

Compare these calculations with measurements of the experimental resolution shown in Figs. 4.4 (axial) and 4.5 (transverse). The axial resolution for TH is measured to be 9.0 μ m by scanning the focus axially through a 100 nm HfO_2 thin film on a fused silica substrate and recording the resulting TH signals. Of course, the focus passes through two interfaces, air-HfO_2 and HfO_2-fused silica, but this is assumed to have negligible effect on the measurement owing to the small optical separation between these interfaces. The transverse resolution for reflected light is measured to be 1.50 μm by scanning the focused beam in a perpendicular line across a sharp ($\approx$ 10 nm) gold edge and monitoring the reflected signal. These values of axial and

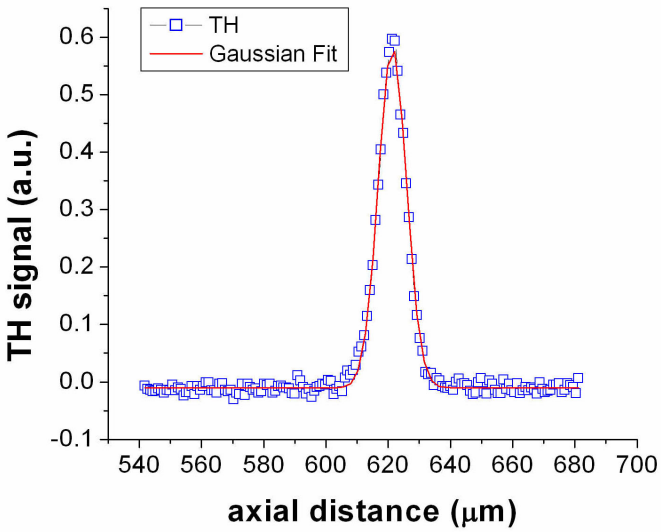

Figure 4.4: Measured TH signals and gaussian fit for an axial scan of the focal volume through an air-fused silica interface. The FWHM (9.0 μm) constitutes a measure of the axial resolution of this microscope.

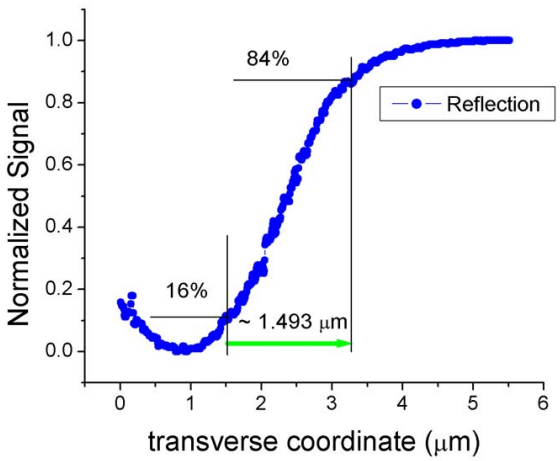

Figure 4.5: Measured reflection signals for a line scan across a sharp ($\approx$ 10 nm) etched gold edge. The distance ($\approx$ 1.5 μm) between 16% and 84% of the normalized height of the curve (FWHM of the differentiated curve) constitutes a measure of the transverse resolution of this microscope for reflection imaging.

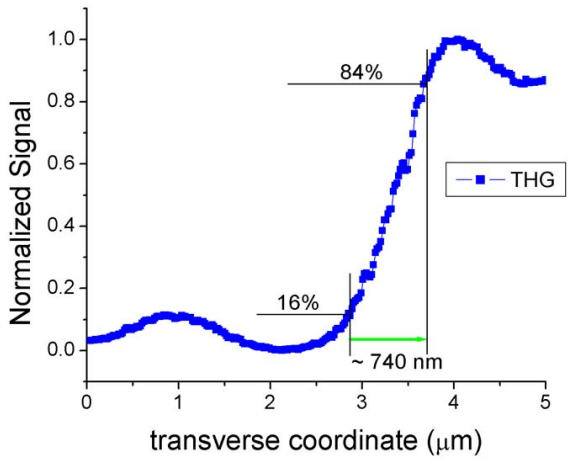

Figure 4.6: THG signals for a line scan progressing left to right from a gold film, across a sharp (≈ 10 nm) etched gold edge and onto a glass substrate. The distance (≈ 740 nm) between 16% and 84% of the normalized height of the curve (FWHM of the differentiated curve) constitutes a measure of the transverse resolution of this microscope for THG imaging.

transverse resolution compare closely with the estimated values. Interestingly, TH data, Fig. 4.6, collected simultaneously with the reflection data of Fig. 4.5 indicates a transverse resolution of ≈ 740 nm. The reduction in resolution from reflection to TH measurements likely is due to the reduced half width of the transverse beam profile for I^3 dependency of the TH signal. Theoretically for Gaussian beams, I^3 dependence should lead to $1/\sqrt{3} \approx 0.58$ reduction in the FWHM of the measured transverse resolution. For perfect Gaussian beams we would expect $1500 \times 0.58 = 870$ nm transverse resolution in the TH signal.

4.2.2 Residual polarization ellipticity in the sample plane

From Section 2.2.2 we know that TH signals vanish for purely isotropic media under circularly polarized illumination. Typically, this relationship is exploited by THCP

imaging to create contrast from areas of localized anisotropy in otherwise highly isotropic media. It has been shown that contrast gained via THCP can be highly sensitive to QWP alignment. In the case of [27], misalignment of the QWP by as little as 0.1° destroyed what contrast was gained by using THCP signals. In part this is due to complications arising from the application of broad spectral width fs pulses (typically >10 nm FWHM) with a QWP designed to work at a single wavelength. Due to chromaticity in birefringent phase retarders, the entire spectrum of such pulses is not equally retarded in phase. The result is that by rotating the QWP, the sum field never reaches circular polarization but only alternates between linear polarization and elliptical polarization. By using zero order waveplates instead of multiple order waveplates this effect largely can be negated. Indeed, zero order waveplates of double crystal construction (often quartz-MgF_2) may exhibit nearly achromatic behavior with only minor polarization error due mainly to misalignment of the crystal axes [87]. A recently developed model allows for the design of broadband achromatic waveplates based upon multiple birefringent media and optimization over an entire range of wavelengths rather than at one specific wavelength [88]. Such a waveplate would be ideal for working with broadband fs pulses since the spectral energy distribution of such lasers is fairly uniform around a central wavelength. Currently however, some ellipticity is unavoidable when using a commercially available double crystal birefringent QWP. Noting that residual ellipticity in the fundamental field which drives the TH process leads to an increase in undesired background THLP signals from interfaces between isotropic media, we desire to characterize the extent and effect of such ellipticity.

The residual ellipticity of the incident illumination in the sample plane may be determined by monitoring TH signals as a function of QWP angle. This assumes that the elliptical field may be considered as a superposition of two electric fields, one circularly polarized and one linearly polarized, where only the linearly polarized field generates TH signals. By rotating the QWP we transfer energy between these

two coherent electric fields.

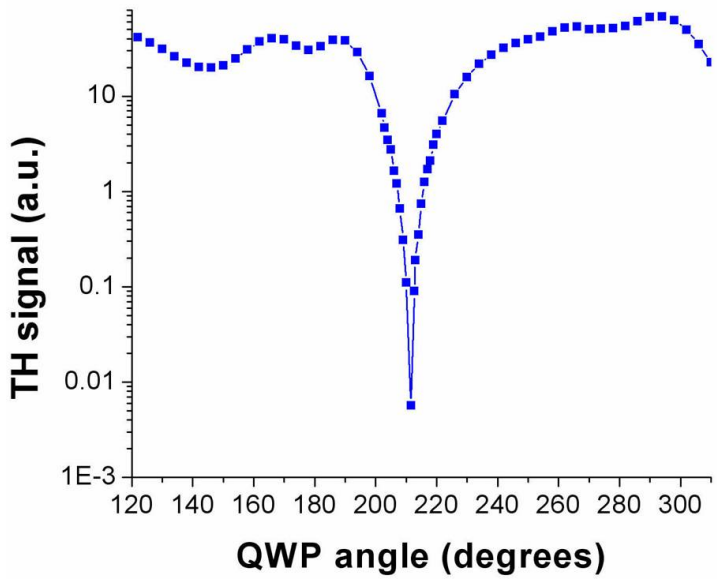

Figure 4.7: TH signals from 110 nm hafnia thin film on fused silica as a function of quarter-wave plate orientation. The minimum occurs when the incident field is nearest to circular polarization.

For the TH microscope in Fig. 4.3 we examine the sensitivity of THCP signals to QWP alignment. Using a sample of 100 nm hafnia film on fused silica substrate, which exhibits both the largest TH signal and the largest reduction in TH signals of any sample employed here, TH signals are recorded as a function of QWP angle (Fig. 4.7). The reduction in TH signals from linear polarization to supposed circular polarization is $\approx 16,000 : 1$. Accounting for the I^3 dependence of TH signals, that indicates a decrease of approximately $25\times$ in the power corresponding to the linearly polarized field. The total average optical power is conserved (≈ 320 mW), since the energy is only transferred from the linearly polarized field to the circularly polarized field. A $25 : 1$ reduction in power corresponding to the linearly polarized field suggests that the residual power attributed to the linearly polarized field is only $320/25 \approx 13$ mW. For this QWP alignment, TH signals equal the noise floor of our setup. In this case, TH signals exceed the noise only when the power attributed to

the linearly polarized field is greater than 13 mW. This value is confirmed simply by attenuating linearly polarized light focused into the sample and observing the resultant TH signal. Recall that this sample was chosen because it results in both the largest TH signals and the largest change in TH signals for QWP alignment. Therefore, for all samples interrogated in our setup are not limited in THCP contrast by residual ellipticity in the incident beam.

4.3 Spatial sensitivity: Imaging of individual colloidal gold nanoparticles

Metallic nanoparticles and semiconductor QD's show great promise as labels for multiplexed optical detection. Their output is tunable based on size (resonance) effects. TH signals have also shown sensitivity to nanoparticles and effectively serve as an additional signal wavelength which is size independent. Here we study these nanoparticles (of known size) because they may be considered to mimick defects in thin films known to lower the damage threshold fluence by initiating damage processes [35, 36].

Although THCP has been applied to investigate diverse sources of material anisotropy, it remains to be demonstrated an estimate of the minimum size of anisotropy which still leads to detection of a resolution limited spot upon illumination with the types of fs NIR lasers typically employed in multiphoton imaging. To this end, presented here are THCP images of individual 10 nm colloidal gold nanoparticles (Nanopartz Inc., A11-10 in H_2O) spin-coated[†] onto a fused silica substrate. Individual nanoparticles are confirmed by comparing image data to the expected diameter dependent signal scaling. TH microscopy previously has been applied to

[†]Thanks to Travis Savage and Dr. Eric Carnes for their expertise and equipment which made spincoating these samples possible.

image metallic nanoparticles, but never before by making use of circularly polarized illumination to suppress background signals from the surrounding isotropic media. Previous attempts were limited either to imaging aggregate structures of nanoparticles with contrast highly dependent on precise plasmon resonance conditions [19], or to imaging of individual nanoparticles under linearly polarized illumination with a novel setup based on detecting dipole emission to enhance contrast [89]. In the latter case, inherent background noise limited detection of individual nanoparticles to sizes > 40 nm. In the present case, we interrogate gold nanoparticles of 10 nm diameter which present off-resonant plasmon behavior and limit plasmon enhancement of the TH signals [90]. It is presumed that material anisotropy, specifically the polycrystalline structure of gold, is the dominant source of TH signal.

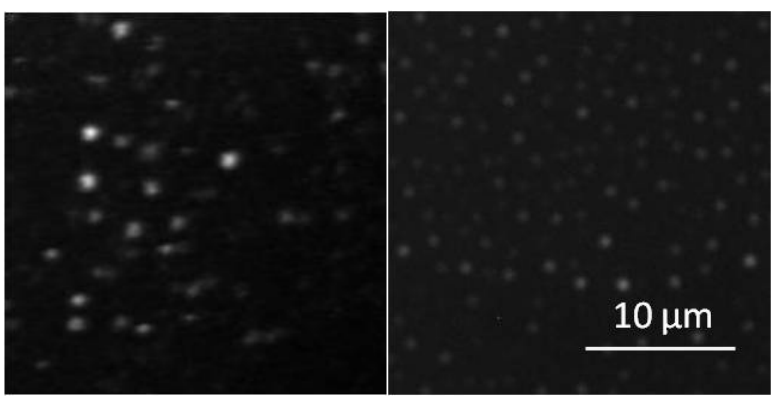

(a) (b)

Figure 4.8: (a) THCP image and (b) dark field image of individual 10 nm colloidal gold nanoparticles.

Figure 4.8 shows both THCP and dark field images of the spin-coated 10 nm gold nanoparticles. Using THCP (65 mW illumination) enables ready detection of individual 10 nm nanoparticles with signal to noise ratio (S/N) $> 100 : 1$. From both images in Fig. 4.8, the same process outlined in [89] is implemented to construct histograms of the distribution of local signal maxima in order to corroborate a particle size distribution consistent with individual particles. A co-localization technique

with Gaussian fit[†] is used to distinguish individual signal centers and to determine the local background and thereby the normalized maximum intensity of each spot. Local background must be accounted for because of uneven illumination in the image. Plotting histograms of these normalized maximum intensities, see Figs. 4.9 and 4.10, confirms a dominant monomodal Gaussian distribution consistent with scattering from individual nanoparticles. According to the expected signal scaling with particle diameter $\propto d^2$ and $\propto d^{0.5}$ for dark field and TH, respectively [91, 90], we extract $\Delta d/d$ of 0.121 and 0.125 respectively. These values agree well with the manufacturers data sheet quoting $\Delta d/d = 0.12$ with Δd being the standard deviation of the particle diameter.

Note that Rayleigh scattering predicts a d^6 scattering signal dependence for 10 nm particles illuminated at visible wavelengths. However, we must account for surface plasmon effects for these gold nanoparticles. The TH signal scaling $\propto d^{0.5}$ assumes off-resonance illumination of a neutral conducting sphere and was previously calculated for 10 nm gold nanoparticles illuminated by a Ti:S laser [90]. For on-resonance illumination of nanoparticles they calculate TH signal scaling $\propto d^{2.5}$. The d^2 dependence of the dark field signal is within the range previously observed for plasmon resonance enhanced white light scattering of metallic nanoparticles [91]. The TH image was chosen to show the presence of rare hot spots which are presumed to indicate aggregates of particles. From these measurements, we assert that detection of gold nanoparticles ≥ 10 nm in diameter is easily accessible with our setup. To the author's knowledge, these are the smallest individual metallic nanoparticles imaged via any TH technique.

[†]Thanks to Peter Relich and Dr. Keith Lidke for their time and for use of their image processing software.

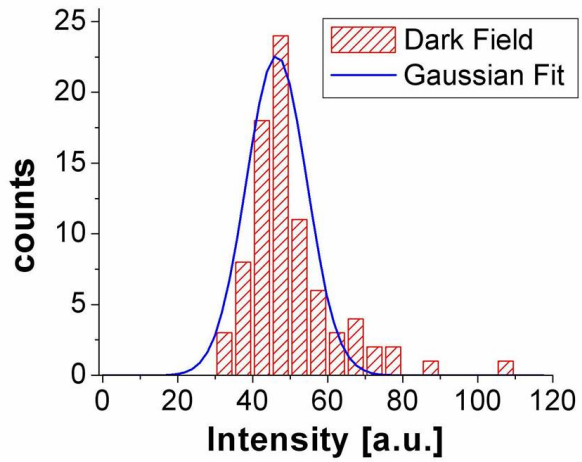

Figure 4.9: Histogram with gaussian fit of normalized maximum intensities from a dark field image of 10 nm colloidal gold nanoparticles.

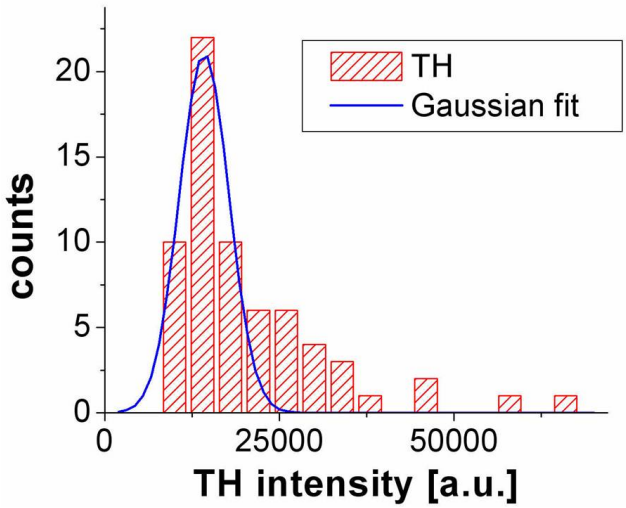

Figure 4.10: Histogram with gaussian fit of normalized maximum intensities from a THCP image of 10 nm colloidal gold nanoparticles. Signal intensities above 40,000 are assumed to indicate aggregate structures.

4.4 Sensitivity to material strain: Imaging of nanoindentations in fused silica

Laser induced stress leading to fracture is commonly observed in oxide thin film damage for single pulse exposures slightly above damage threshold. Images of such

fracture are discussed in Appendix A. It is also possible that laser induced stress may lead to permanent material strain even prior to damage. Noting that strain represents a type of anisotropy, THCP microscopy offers great potential for imaging induced strain in highly isotropic materials like oxide thin films. In this capacity, THCP imaging may lend insight into both the role that strain may play in incubation, as well as the extent of residual strain following damage formation. Since the applicability of THCP to imaging induced material strain has not been demonstrated previously, we seek to characterize THCP sensitivity to areas of known induced stress. For this purpose we turn to mechanical nanoindentation as a finely controlled method of applying stress (force per area) and inducing permanent strain (deformation).

Quality fused silica is highly isotropic, and even at the detection limit of our system does not yield THCP S/N > 1. For this reason, fused silica lends itself well to studying anisotropy induced via mechanical nanoindentation. Here we have used a steel Berkovich tip pyramidal nanoindenter[†] (142.3° angle, Micro Materials Ltd. NanoTest) to apply variable loads to fused silica and to simultaneously record depth versus load data. The average depth versus load curve for ten separate 200 mN indentations, Fig. 4.11, reveals a plastic depth of 869 nm ($\pm$ 5 nm) corresponding to a load of $\approx$ 96 mN. The plastic depth is the maximum depth of indentation for which no permanent deformation remains in the material after unloading. For nanoindentations with 100 mN load, the residual deformation of each indentation has a depth of $\approx$ 17 nm. Such 17 nm nanoindentations are easily revealed (Fig. 4.12) in THLP, THCP and dark field images. Most notably, while THLP reproduces the shape of the indent, as confirmed by dark field, TH with circular polarization reveals three distinct signal centers offset from the corners of the indenter. Since THCP is expected to be sensitive to anisotropy indicative of material strain, these three spots may indicate regions of localized strain. This effect has been observed previously in

[†]Thanks to Michael Sheyka for his expertise, time and help with nanoindenting. Also, thanks to Stoney Haver for his help in coordinating the nanoindentation efforts.

500 mN nanoindentations of quartz via Raman microspectroscopy [92] and was measured to indicate strain due to residual compressive stress. Since these spots appear near resolution limited, we cannot determine the exact size or shape of the strain centers. Neither TH nor dark field yielded optical signals from nanoindentations with loads corresponding to depths less than the plastic depth.

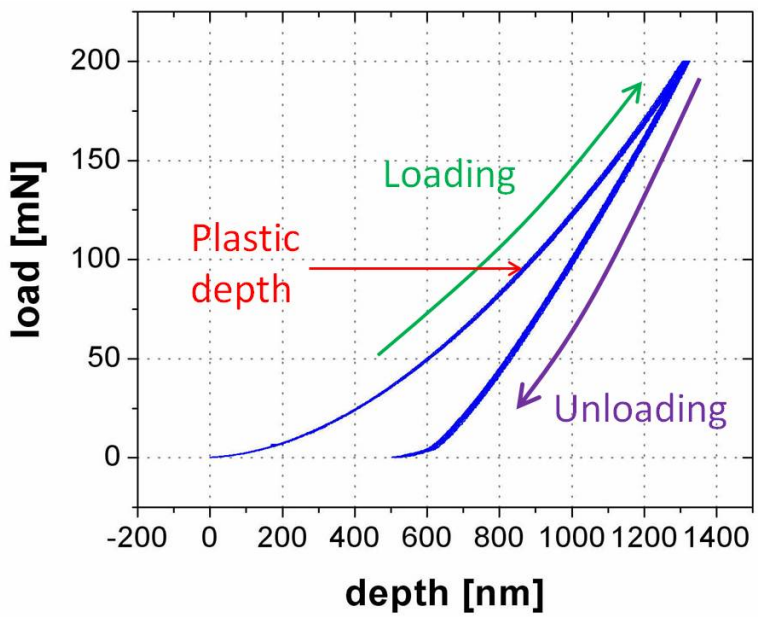

Figure 4.11: Average depth vs. load curve for ten 200 mN indentations in fused silica. The plastic depth of 868.7 nm ± 5.1 nm, corresponds to a load ≈ 96 mN.

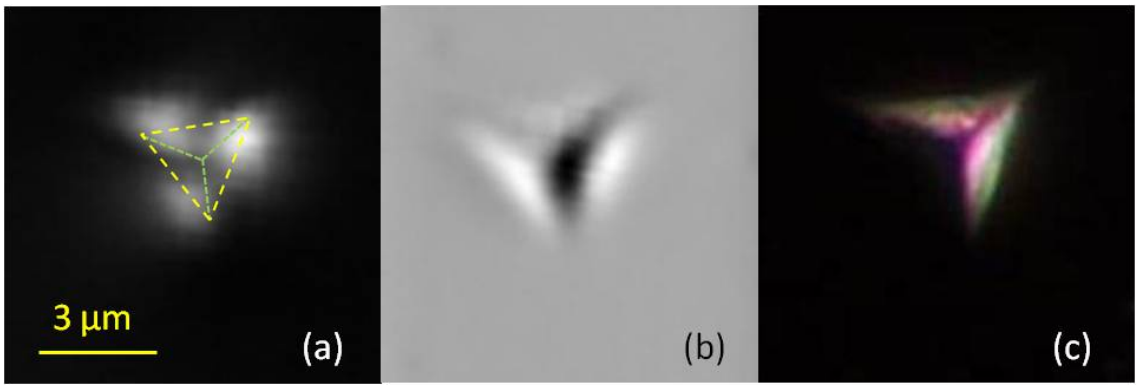

Figure 4.12: (a) THCP, (b) THLP, and (c) dark field images of the same 100 mN nanoindentation. The overlaid triangle indicates the relative outline of the THLP image.

4.5 High dynamic range of third-harmonic signals in thin film laser damage

Optical microscopy is often employed in thin film laser damage studies for characterizing the morphology of damage spots. Sensitive techniques such as Nomarski and dark field microscopy lend insight into the mechanisms of damage and may even provide estimates of quantitative data such as the depth of material removal. While it is clear that laser damage may induce changes in the films' behavior with respect to transmission, reflection, scattering, and birefringence, it's not immediately obvious how these potential sources of contrast relate to the measured optical signals which ultimately limit the usefulness of the microscopic techniques based on these sources of contrast. Bright field, dark field, Nomarski, TH, and polarization imaging all provide complementary information as outlined in Appendix A and therefore all may be considered indispensable. However, the sensitivity of each technique may vary greatly, even for the same sample, and ultimately limits the range of applicability for each technique. One measure of sensitivity is the dynamic range of the generated signals. The dynamic range is simply the ratio of the largest measured

signal to the smallest measured signal. In many cases the smallest measured signal may be considered equal to the inherent signal noise, where the signal noise itself is determined by the background signals which are characteristic for each specific imaging technique.

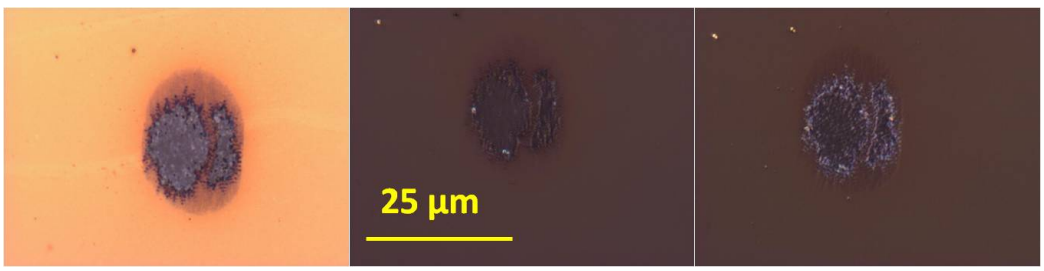

(a) (b) (c)

Figure 4.13: (a)Bright field, (b)polarization and (c)Nomarski images of multi-pulse damage in alumina capped hafnia taken with the maximum dynamic range of each technique.

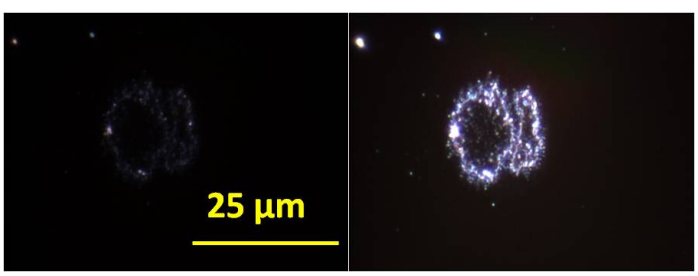

(a) (b)

Figure 4.14: Dark field images of multi-pulse damage in alumina capped hafnia with (a)1x and (b)8x relative gain on the detector to capture signals across the total dynamic range.

For a typical damage exposure in 100 nm hafnia film with 10 nm alumina cap layer, we compare the dynamic range of optical signals for several techniques often used to investigate thin film laser damage. An Olympus BX60 microscope with variable gain CCD camera (Lumenera Infinity 2) provides the bright field, polarization, Nomarski and dark field images in Figs. 4.13 and 4.14. The TH microscope

of Fig. 4.3 provides the THCP images in Fig. 4.15. In all cases, first the detector gain is set so that the largest detected signal within the laser exposure is kept below the saturation level of the detector. When the minimum signal within the exposure is simultaneously greater than zero, that single image contains the entire dynamic range of measured signals. This is the case for bright field, polarization and Nomarski imaging techniques. However, if the minimum signal is zero for the first image, as is the case with dark field and THCP, the gain must be increased and subsequent images collected until the minimum signal from within the laser exposure is nonzero. Knowing the relative gain factor for each image, we may then calculate the total dynamic range by multiplying the largest signal in the first image by the gain factors and dividing by the smallest signal in the last image collected. The dynamic range of each imaging technique is shown in Table 4.1. THCP images reveal by far the largest dynamic range for this thin film laser damage spot. It should be noted that both polarization and THCP images utilize birefringence as a source of contrast. However, THCP exhibits a much larger dynamic range. This suggests that THCP may be superior in dynamic range due to both the nearly background free signals collected from this highly isotropic sample and an enhanced sensitivity to birefringence. Assuming this to be the case, THCP images offer a clear advantage in terms of sensitivity to the study of damage morphology in highly isotropic thin films.

Imaging Technique	Bright field	Nomarski	Polarization	Dark Field	THCP
dynamic range	4.6 : 1	5.8 : 1	6.7 : 1	760 : 1	10^6 : 1

Table 4.1: Dynamic range of signals from images of laser induced damage in alumina capped hafnia dielectric film for several far field microscopy techniques.

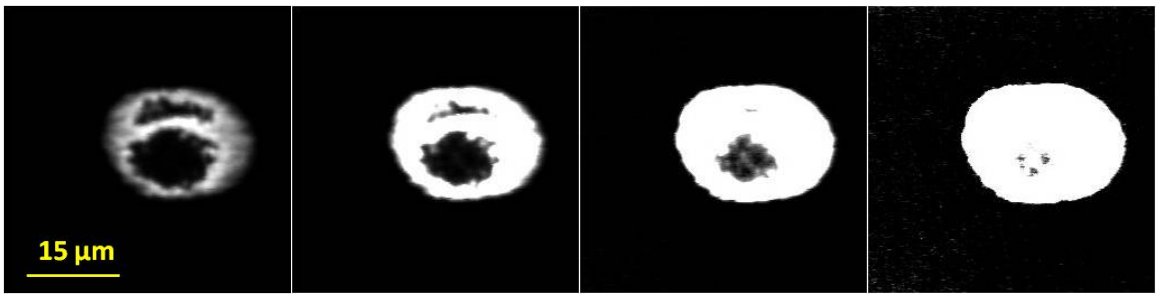

(a) (b) (c) (d)

Figure 4.15: (a)-(d) THCP images of multi-pulse damage in alumina capped hafnia with increasing gain on the PMT detector to capture signals across the total dynamic range. From left to right the gain increases by a total factor of ≈ 200.

4.6 Third-harmonic application to laser damage morphology

The study of laser damage morphology is chiefly concerned with characterizing the shape, size and structure of laser induced material changes. These properties lend insight into the mechanisms of damage and often provide qualitative feedback to the impact of several factors including environmental effects (such as damage in a vacuum $< 10^{-5}$ Torr [35]), the illuminating beam profile and sample annealing [93]. Several techniques may be used in tandem to study damage morphology; optical microscopy, electron microscopy and atomic force microscopy constitute the techniques most commonly used.

Figure 4.16 shows a simplified progression of characteristic changes in the laser exposed film as the fluence of incident light is increased. At laser fluences below the material's damage threshold, material modifications may be formed that last anywhere from picoseconds to months to years. Such modifications are known to include color center formation, self-trapped excitons and laser induced chemical modifications. When optics must be removed from a damage experiment prior to in-

vestigation, only long lived material modification is studied. Near the laser damage threshold fluence catastrophic physical changes occur to the optic including fracture and material ablation. Above the damage threshold fluence a considerable amount of material is ablated, possibly exposing the substrate. Study of these heavily damaged spots, including the quantification of material removed, also may be of specific interest for laser micro-patterning.

THCP and THLP offer unique information when applied to laser damage morphology of thin films. THLP probes $\chi^{(3)}$ and may be used to measure the extent of film removal. THCP images laser induced anisotropy directly in these otherwise isotropic films. From Sections 4.3, 4.4 and 4.5 it's clear that THCP may provide high dynamic range sensitivity to nanoscale anisotropy and induced strain, two effects known to play a role in LIDT studies. This section focuses on applying THLP and THCP imaging to thin film laser exposures above damage threshold. Section 4.7 deals with their application to predamage material modification.

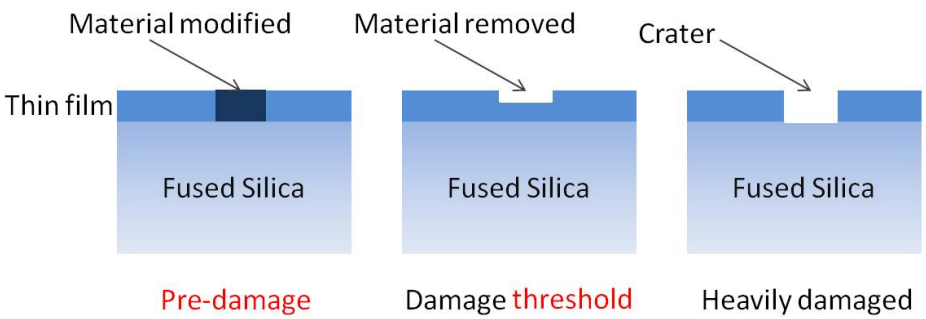

Figure 4.16: A simplified progression of observed damage morphology.

Before continuing further, I must pause to extend my thanks to Dr. Carmen Menoni and her group at Colorado State University for providing the thin film samples used throughout this work. Additionally, I'm indebted to Duy Nguyen who performed all of the laser damage experiments on the samples interrogated here. Without them the following work would have suffered greatly.

The following data are for a hafnia thin film on fused silica substrate. The film has an optical thickness of $\lambda/4$ at 800 nm (110 nm physical thickness, ion beam sputtering deposition) so that the highest intensity in the standing wave is at the film-substrate interface. For a 20 μm beam diameter incident on the film, the single pulse damage fluence was measured to be $F_1 = 0.48$ J/cm^2 for a 50 fs pulse with center wavelength 800 nm [94]. Using the TH microscope described in section 4.2, images of the heavily damaged spot are recorded for three different techniques: confocal reflection, THCP, and THLP.

Let's review what is expected of each imaging technique. The reflection images are expected to show a distribution in reflection coefficient. This implies that areas with increased roughness (scattering) or increased transmission may appear darker than the average surface value. The THLP images are expected to show a distribution in $\chi^{(3)}$ for signals dominated by the contribution from the HfO_2 film. The THCP images are expected to show a distribution in $\chi^{(3)}$ for signals dominated by anisotropy. Since the film and substrate are assumed to be isotropic, this signal should be indicative of laser induced material modification characterized by an anisotropic $\chi^{(3)}$ tensor.

Consider the images in Fig. 4.17 taken of a heavily damaged ablation crater. For all three imaging techniques, the cross sections taken at the line indicated in Fig. 4.17a are shown in Fig. 4.18. Consulting these cross sections we can attempt to decipher the information displayed in the three images. For this heavily damaged spot, the film is expected to be completely ablated, thereby exposing the fused silica substrate beneath. Reflection signals across the damage spot fall near the edge, but rise again in the center. THLP signals decrease sharply moving into the spot but rebound slightly near the middle. THCP signals rise dramatically near the edge of the spot and reach a minimum in the middle of the spot. With no signal generated in the unexposed areas of the film, it is clear that THCP signals indicate some laser induced material modification around the spot that leads to anisotropy. This anisotropy is

likely the result of either induced strain or melting and subsequent crystallization of the material. These three signal patterns support the hypothesis that the film was ablated down to the fused silica substrate. The rise in the reflection signal in the center of the exposure is interpreted as reflection from exposed fused silica. The THLP signal in the center of the exposure is interpreted as THLP from the air-fused silica interface. This is further confirmed by flipping the sample over to record THLP signals from the air-fused silica interface directly. The resulting ratio of signals from the air-hafnia interface and the air-fused silica interface, $\approx 6:1$, matches the ratio of signals outside and inside the exposure. Combining the qualitative and quantitative interpretation of all three signals we infer the sample topography of Fig. 4.19. The damage exposure leads to complete film ablation in the center of the spot with laser induced anisotropy evident in the film remaining around the edges of the spot. Viewing several multi-pulse exposures above damage threshold, it becomes clear that both ablation and material modification leading to anisotropy occur preferentially in the center of the exposure as expected for a transverse Gaussian beam profile.

The preceding discussion may be considered an easiest case scenario since such a heavily damaged spot was expected to exhibit complete ablation of the film. However, it allows us to clearly understand the expectations from THLP and THCP images. Let us now consider what types of information can be gleaned from an exposure above damage threshold where it is unclear how much material has been ablated.

The following data are for a hafnia thin film with alumina cap layer on fused silica substrate. The hafnia film has a physical thickness of 100 nm, while the alumina cap layer is just 10 nm thick. The addition of a thin cap layer with higher bandgap than the underlying film has been shown to increase the damage threshold of such films considerably [94]. However it's not clear why or how such a cap effects the ablation process. Again, using the TH microscope described in Section 4.2, images of the exposed spot are recorded for three different techniques: confocal reflection, THCP,

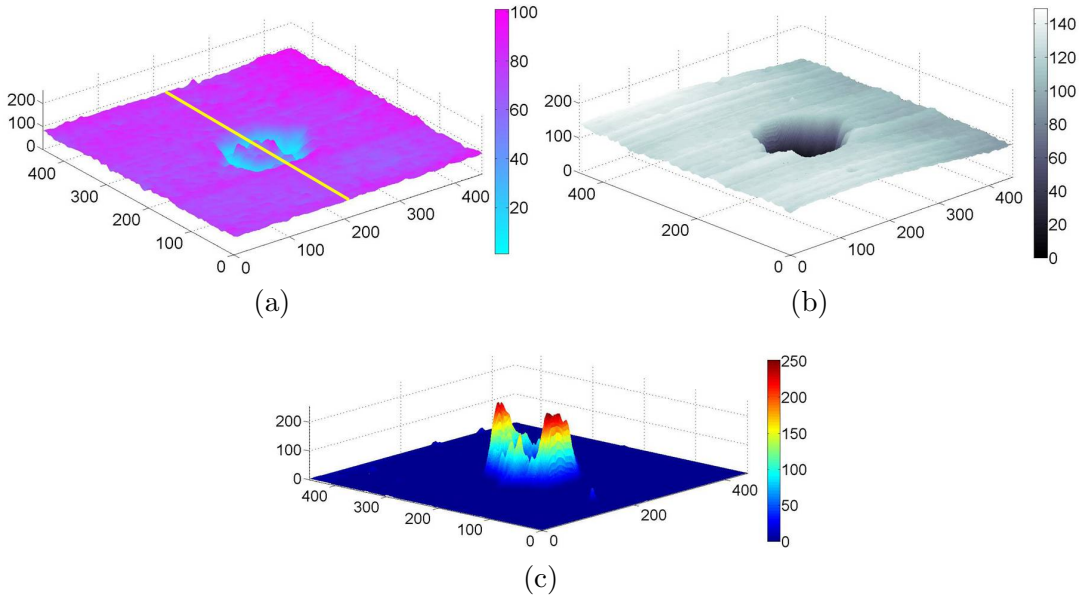

Figure 4.17: Surface plots of the measured optical signals for (a)reflection, (b)THLP and (c)THCP images of a multi-pulse damage crater in 110 nm hafnia thin film on fused silica substrate. The line in (a) indicates the location of the cross section taken from each of the three images.

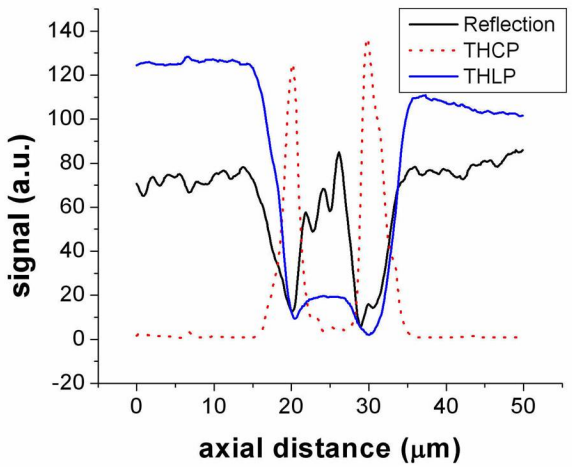

Figure 4.18: Cross sections of reflection, THLP and THCP signals from a multi-pulse damage crater in 110 nm hafnia thin film on fused silica substrate.

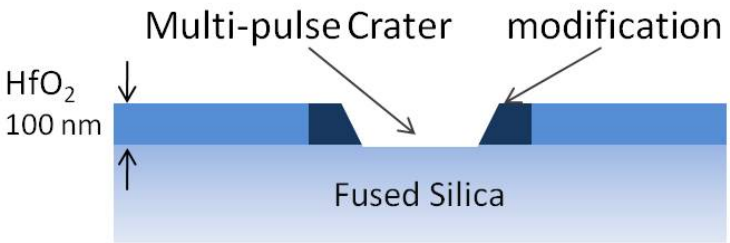

Figure 4.19: The inferred sample topography for a multi-pulse damage crater in 110 nm hafnia thin film on fused silica substrate.

and THLP.

Consider the images in Fig. 4.20 taken of a multi-pulse damage spot. For all three imaging techniques, the cross sections taken at the line indicated in Fig. 4.20a are shown in Fig. 4.21. The ratio of reflection signals outside and inside the exposed spot is too large ($\approx 8:1$) to indicate reflection from a smooth surface of either hafnia ($< 5:1$ expected) or fused silica ($\approx 5:1$ expected) even when accounting for multiple thin film reflections. Reflection signals must be interpreted to indicate the presence of a rough scattering surface in one of the films. THCP signals are similar to the previous case and indicate laser induced anisotropy around the perimeter of the exposure. Interestingly, it appears that no laser induced anisotropy remains in the center of the exposure. Consulting the THLP signals may indicate why this is so. Comparing THLP signals inside and outside of the exposure, it's clear that the THLP signals are largest in the center region where THCP signals vanish. Since THLP probes $\chi^{(3)}$ directly and noting that $\chi^{(3)}_{FusedSilica} < \chi^{(3)}_{alumina} < \chi^{(3)}_{hafnia}$, the simplest conclusion is that the alumina cap layer is entirely removed but some of the underlying hafnia remains. If the hafnia layer were entirely removed thereby exposing the substrate, one would expect THLP signals similar to Fig. 4.18 which decrease inside the exposure. It's possible that this simple conclusion may be verified by ongoing research within our group [66] via either simulation of TH signals as a function of film thickness or simultaneous measurement of TH signals in reflection.

Such simulations require a fairly sophisticated model that accounts for multiple thin film reflections, NA of the focusing objective, and clipping of the incident light at the entrance aperture of the focusing objective, but they promise to supply quantitative data about material removal. From just the data presented here we infer the sample topography shown in Fig. 4.22. Apparently, the alumina cap layer is removed entirely in the interior of the exposure. Clearly, laser induced anisotropy remains around the edge of the exposure. It's not possible to say if or how much of the hafnia layer has been ablated, but certainly the substrate is not exposed.

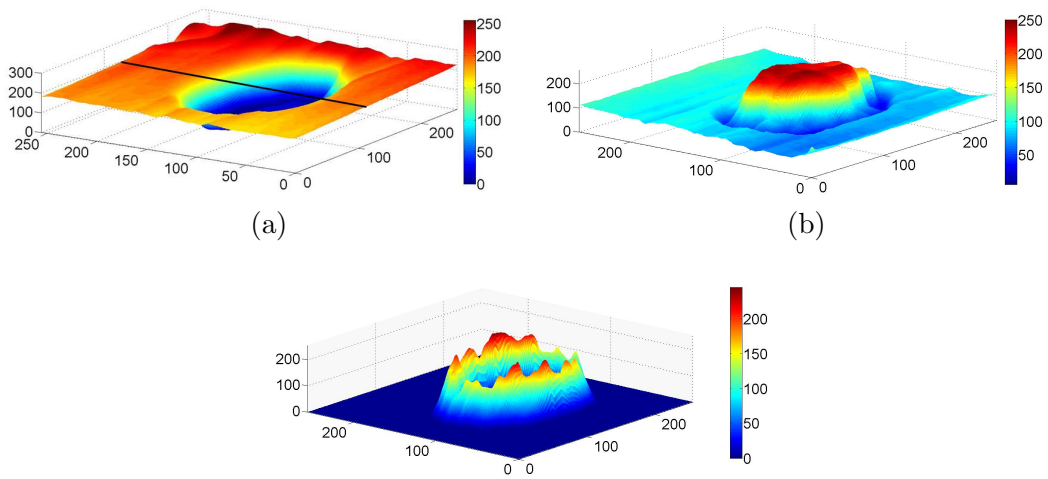

Figure 4.20: Surface plots of the measured optical signals from (a)reflection, (b)THLP and (c)THCP images of a multi-pulse damage exposure in alumina capped hafnia thin film on fused silica substrate. The line in (a) indicates the location of the cross section taken from each of the three images.

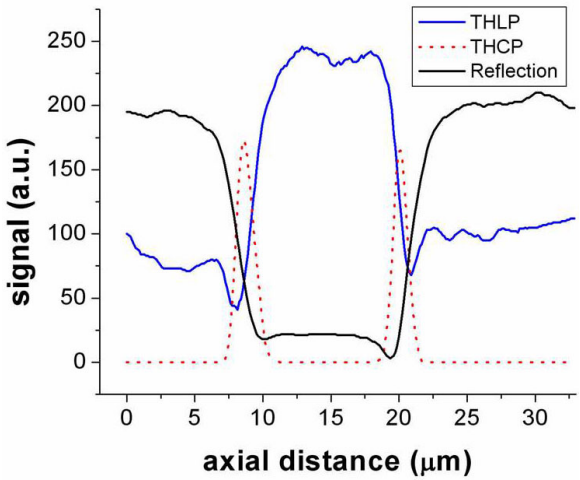

Figure 4.21: Cross sections of reflection, THLP and THCP signals from a multi-pulse damage exposure in an alumina capped hafnia thin film on fused silica substrate.

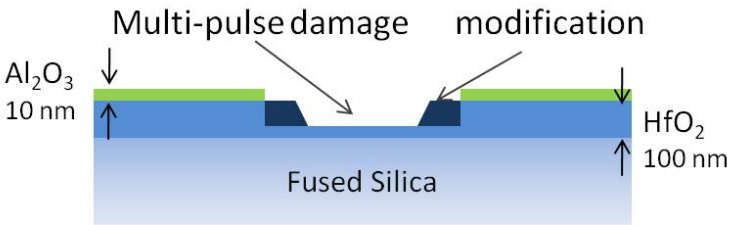

Figure 4.22: The inferred sample topography for a multi-pulse damage exposure in an alumina capped hafnia thin film on fused silica substrate.

4.7 Third-harmonic application to laser-induced material modification prior to damage

TH microscopy provides clear advantages over Nomarski and other sensitive imaging techniques in terms of dynamic range, sensitivity to material modification and sensitivity to material removal when applied to the study of laser damage morphology. The question now becomes, does TH microscopy indicate the presence of material modification before damage occurs?

We examine a pattern of exposures near damage threshold where the position of pre-damage exposures is determined with reference to clearly damaged marker spots. Figure 4.23 shows images of pre-damage laser induced material modification for an incubated spot (50 fs, 0.39 J/cm^2, 1 KHz, 3 minute exposure, 25 μm diameter focus). Such incubation spots were found to create contrast in only THCP, Nomarski and polarization images. Figure 4.23 shows Nomarski (a) and THCP (b) images of the same pre-damage exposure in a 110 nm hafnia thin film on fused silica substrate. Corresponding cross-sections are shown in (c) and (d) respectively. The THCP image yields much higher S/N ratio, $\approx 210:1$, than both Nomarski and polarization, $\approx 2.3:1$ and $\approx 2.2:1$ respectively. The THCP contrast is significant when one considers that such a spot likely would be overlooked with the other techniques had we not known the position of the exposure. Nomarski and polarization techniques essentially both yield images with nominal contrast bordering on unusable.

This answers the long standing question about whether permanent material modifications exist prior to damage formation. Though we haven't observed any laser exposure spots where THCP is the only technique that creates contrast, thus far we have probed only spots with long lived modifications. Perhaps smaller changes in material anisotropy are short lived and must be sought while a damage experiment is ongoing. This is where THCP may provide truly unique insight due to it's potential

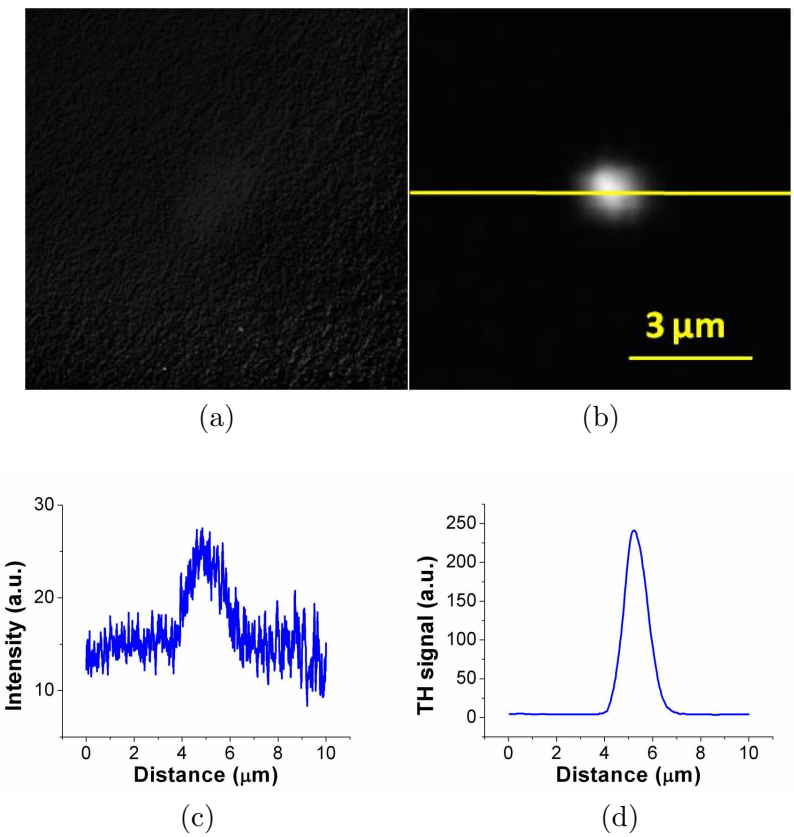

Figure 4.23: (a)Nomarski and (b)THCP images of a predamage multi-pulse exposure in 110 nm hafnia film on fused silica substrate. The line in (b) indicates the location of cross sections shown in (c) and (d) of Nomarski and THCP respectively.

to probe the material while damage experiments are running.

4.8 Third-harmonic application to inherent properties of high quality thin films

THCP in reflection was previously demonstrated as a way to examine large order (several mm) anisotropy in opaque semiconductor films [38], but here we apply it to localized anisotropy in transparent films via microscopy. At the detection limit of our system, maximum laser power ≈ 320 mW at the sample and maximum gain on the PMT $\approx 10^6$, THCP is able to image features in the nascent films themselves. For all the nascent films scrutinized here, THCP alone creates contrast. Other techniques known to exhibit high sensitivity for thin film interrogation (Nomarski, polarization, dark field, THLP) all fail to reveal any features from the films. For example, compare the Nomarski, THCP and dark field images of a nascent 100 nm hafnia film in Fig. 4.24.

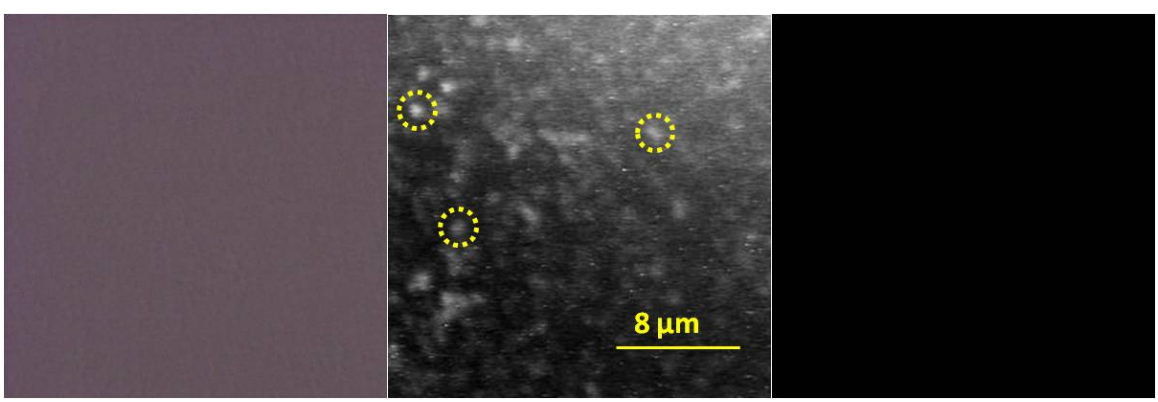

(a) (b) (c)

Figure 4.24: (a)Nomarski, (b)THCP and (c)dark field images of 110 nm hafnia film at the detection limit for each technique. Circled regions in (b) indicate localized material anisotropy in the nascent film.

By both translation of the sample and comparison with images of the fused silica-air interface (Fig. 4.25) we confirm that the structures observed for nascent

film samples originate in the film alone. Single THCP images of two scandia films, S1 and S2, deposited by ion beam sputtering (IBS) under different partial pressures of oxygen [95] are shown in Fig. 4.26 (a) and (b). To quantify the clear difference in appearance we calculate the RMS variation in THCP signal for each film after averaging series of 10 images and subtracting the background, Fig. 4.26 (c) and (d). Background subtraction is necessary to counter uneven illumination and should yield a more accurate RMS variation. Table 4.2 shows the resulting THCP RMS variation for three scandia films along with the partial pressure of oxygen during deposition, residual stress in the film and RMS in the atomic force microscope (AFM) images. Note that while TH RMS distinguishes between the films, AFM measurements of RMS surface roughness do not vary significantly between the films. Comparison of THCP (Fig. 4.26c) and AFM (Fig. 4.27) images for film S1 also suggest no spatial correlation between the two data types. It does not appear that TH signals simply indicate a surface roughness. However, the THCP RMS roughness does correlate with the stress in the film as determined by macrostrain measurements. Macrostrain is a measure of a film's ability to deform the substrate and is determined via Michelson interferometry. We must infer that the localized structures present in THCP images lead to a macroscale deformation of the sample.

Following the same technique to inspect high quality (damage fluence > 0.40 J/cm^2) hafnia films reveals the presence of similar structures. For example, processing the THCP image of Fig. 4.25a yields a THCP RMS variation of 3000 (a.u.). Compared to other techniques used to investigate material stress and crystallinity, such as X-ray diffraction, THCP imaging is a relatively simple all optical method that has the advantage of localized spatial inspection. Furthermore, THCP imaging adds the potential to provide monitoring of thin films during the deposition process if one desires to monitor or mitigate the formation of such features.

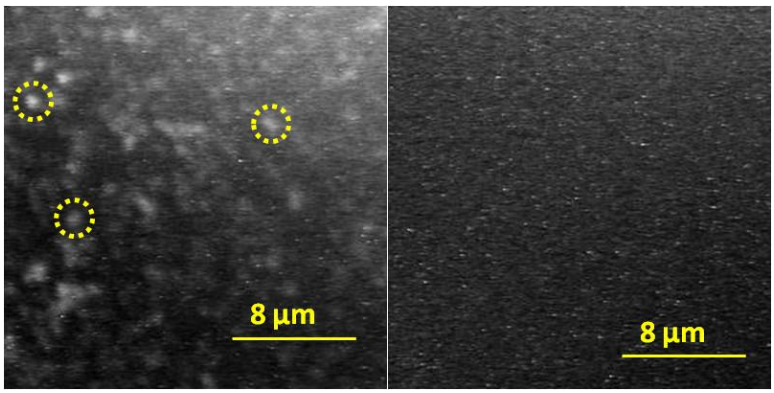

(a) (b)

Figure 4.25: THCP images of (a) the air-film interface and (b) the air fused silica interface for the 100 *nm* hafnia sample shown in Fig. 4.24.

	S1	S3	S2
O_2 partial pressure [torr] [96]	4.0 E-5	1.7 E-5	5.0 E-6
TH RMS [a.u.]	4300	4700	2300
Stress [GPa] [96]	1.20	1.19	0.85
AFM RMS [nm] [96]	0.7	0.7	0.6
Absorption @1064 nm [ppm] [97]	37.6	27.5	10.5
Absorption @532 nm [ppm] [98]	4000	2900	980
Absorbance @296 nm [%] $\pm$ 0.5 [96]	5.7	3.6	1.0

Table 4.2: Comparison data for three scandia films grown by IBS deposition under different partial pressures of oxygen.

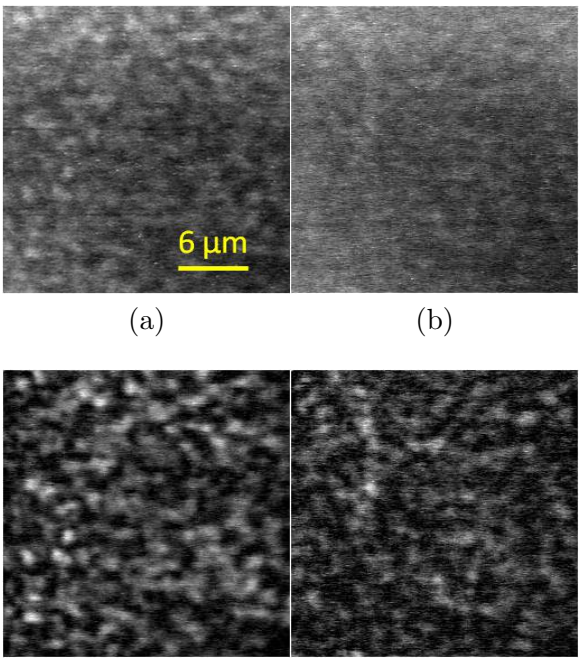

Figure 4.26: Single THCP images of (a) S1 and (b) S2 thin films taken at the detection limit. The average of ten such images with the background removed for (c) S1 and (d) S2 films.

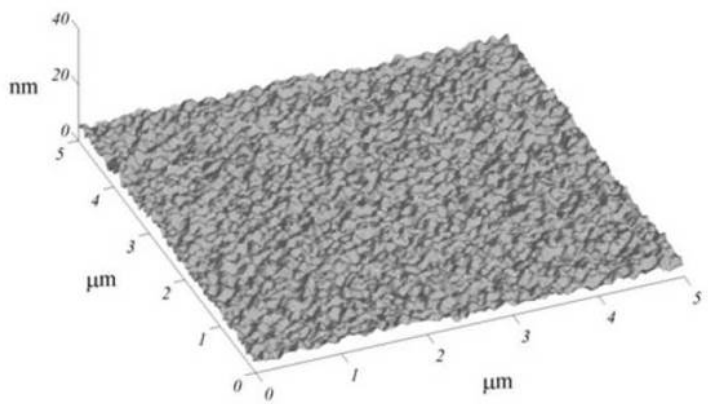

Figure 4.27: AFM image of scandia film S1. The RMS surface roughness is 0.7 nm.

4.9 Third-harmonic application to reversible material modification

For lower quality films, as assessed by relative absorption levels, laser-induced material modification is achievable using the same setup as for TH microscopy (cf. Fig. 4.3). A 20 minute exposure ($\approx$ 320 mW $\Rightarrow \approx 4.3\times10^8$ J/cm^2 total) of an 8×8 μm square in scandia film S1 from Section 4.8, leads to $\sim$ 16% decrease in THLP signal generation. Following this 'burning' process we observe reversible material modification with the THLP signal as shown in Fig. 4.28. The level of signal recovery is expressed as the ratio of signals inside the exposure to those outside the exposure as averaged within the two rectangles shown in Fig. 4.28a. This figure of merit is listed in Table 4.3 and shows almost full recovery of THLP signals after 29 hours. Interestingly, THCP signals display no change whatsoever throughout the entire process. Apparently this material modification effects the strength of $\chi^{(3)}$ and not its symmetry. It's not clear what type of material modification is indicated by this change in value for $\chi^{(3)}$. A preliminary hypothesis linked to the timescale of recovery [35] is that the effect may indicate diffusion of water from the air back into the film. The presupposition is that during exposure to sufficient laser fluence, some water content may be removed from the film. This is the only oxide film studied throughout the work presented in this manuscript for which the TH microscope setup was able to cause material modification.

This brief result is recalled here because of its implications for soliciting the need for TH investigation of thin films during laser damage studies. Even though this material modification still persists over a relatively long timescale, it points toward to need to examine the characteristic timescales of laser-induced modification associated with fs LIDT studies.

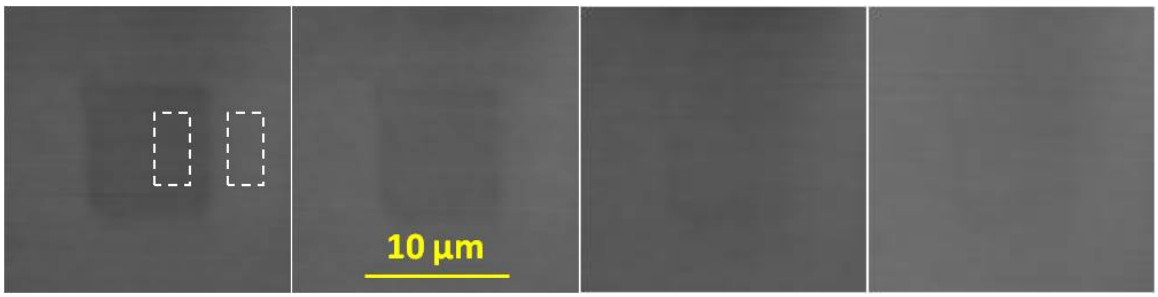

(a) (b) (c) (d)

Figure 4.28: THCP images of a 'burned' square in scandia taken (a) 10 seconds (b) 15 minutes (c) 115 minutes and (d) 29 hours after the end of exposure.

recovery time	10 s	15 m	115 m	29 hr
signal ratio inside/outside	0.84	0.89	0.92	0.95

Table 4.3: The ratio of THLP signals inside/outside the exposed square of Fig. 4.28 measured at four time intervals after the end of the exposure.

4.10 Chapter Summary

Many of the results here are currently featured in publication [99]. Compared with other far-field imaging modalities commonly employed to study thin films, TH microscopy displays significant advantages in regard to both potential sources of contrast and sensitivity to shared sources of contrast, in part owing to it's nearly background free signal with circularly polarized illumination. Presumably this helps TH microscopy to generate contrast where other techniques fail. THCP microscopy displays sensitivity to individual 10 nm gold nanoparticles as well as to the residual material strain following 100 mN ($\approx$ 17 nm) nanoindentation in fused silica. Both mimic effects known to influence the optical damage threshold of high quality thin films. THCP microscopy also provides high dynamic range imaging of laser-induced

material modification in hafnia thin films both pre- and post-damage, where conventional microscopies either fail to create contrast or display drastically reduced contrast. THCP microscopy also provides a method to inspect features related to macrostrain in nascent hafnia and scandia thin films. THLP displays its own unique benefits including sensitivity to the depth of material ablation and to reversible material modification. Certainly, TH microscopy should be pursued further in support of fs LIDT studies.

Chapter 5

Four-wave mixing microscopy with femtosecond resolution

The goal of this chapter is to examine a typical high spatial resolution FWM microscope with two source illumination to determine what information may be revealed on the time domain behavior of samples under study. In principle, by varying the delay between the two excitation pulses one may monitor the behavior of the two simultaneously produced FWM signals and gain insight into both the type of dominant resonant process present in the sample as well as the approximate timescale of the dominant resonant process.

5.1 Experimental setup

The setup for two color four-wave mixing (FWM) microscopy is shown in Fig. 5.1. 35 mW each of Ti:S (787 nm, 60 fs) and OPO (1025 nm, 100 fs) co-propagate and are focused (EC Plan-NEOFLUAR 20×, 0.5 NA objective) into a sample to generate FWM signals in the IR (1469 nm) and visible (639 nm). The FWM and fundamental

light is collected (EDSCORP 20×, 0.4 NA objective) and filtered through a series of dichroic elements to isolate IR and visible signals. The IR FWM signal is detected with an InGaAs femtoWatt photoreceiver (Newport, 2153), while the visible FWM signal is detected with a silicon avalanche photodiode (Hamamatsu, C5460-01). For samples of BK7, fused silica, methanol, ethanol, propanol, butanol, and hexane the resulting optical signals are quite small and necessitate lock-in amplifier detection of both electronic signals. For lock-in detection, the Ti:S beam is chopped at 415 Hz. Both the OPO and Ti:S are polarization controlled via half-wave plate (HWP) and quarter-wave plate (QWP) pair. The HWP is used to rotate the orientation of linear polarization and the QWP is used to compensate birefringence in the optics that would otherwise lead to polarization ellipticity. OPO and Ti:S beams are routinely polarized with extinction ratios 225:1 and 260:1 respectively following transmission through both objectives with no sample present. For polarization sensitive detection, a Glan-Thompson polarization analyzer (Thorlabs, extinction ratio 100,000:1) optionally may be inserted into the detection path after the second objective. The sample is mounted on a piezoelectric stage (Piezosystem Jena d-Drive) for imaging purposes, however here we are most concerned with femtosecond material dynamics probed by FWM signals as a function of the inter-pulse delay. A LabVIEW program coordinates data collection and movement of the motorized delay stage that adjusts the time delay between corresponding pulses of each laser source.

Inherent to nonlinear microscopy with two fs sources, the optical alignment and optimization of nonlinear signals is significantly more complex than in the case of nonlinear microscopy with a single source. In Fig. 5.1, note three critical aspects of this setup. First, the Ti:S and OPO beams are made to be collinear and to arrive perpendicular to the entrance aperture of the focusing objective. This implies that the two beams share a transverse spatial overlap in the focus of the objective. Second, a shared telescope is adjusted so that both beams slightly overfill the entrance aperture of the focusing objective. Along with the previous requirements, this implies

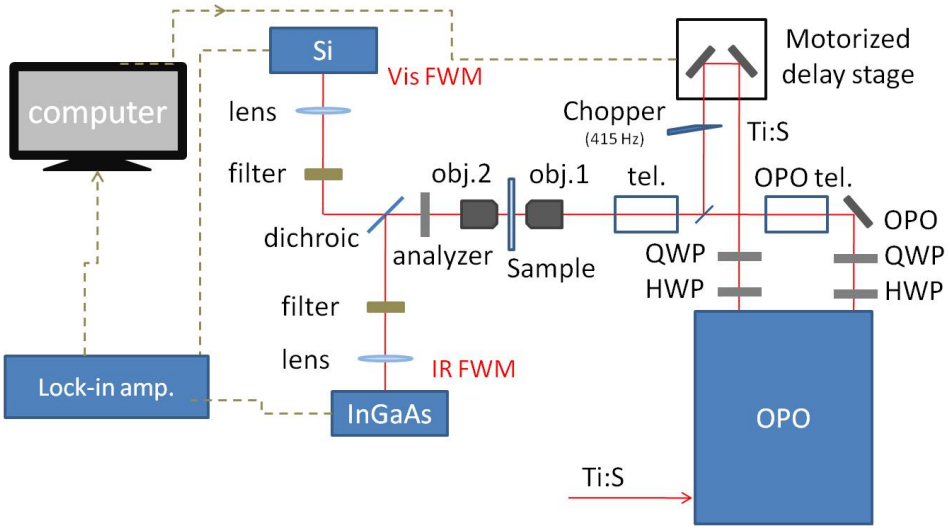

Figure 5.1: Diagram of the FWM microscopy setup.

a minimum transverse spot size in the focus of the objective. The OPO beam has an independent telescope which mainly controls the divergence of the propagating beam. The divergence of the OPO beam can be tuned to overcome chromaticity in the objective so that both beams share a common focal plane. Expressed another way, the two beams share an axial spatial overlap of foci. Third, the Ti:S beam path includes an optical delay line to control the relative temporal delay between corresponding OPO and Ti:S pulses. When Ti:S and OPO beams are aligned to yield minimum spot size with maximum transverse spatial, axial spatial, and temporal overlap, the largest nonlinear signals are expected. Ultimately, these parameters are all fine-tuned by maximizing the resultant nonlinear signals through optical alignment.

Given the short geometrical length of femtosecond pulses ($\approx$ 0.3 μm/fs in vacuum), an experimentally demanding step in aligning the FWM microscope comes while adjusting the Ti:S optical delay path to find the range of temporal overlap ($\approx$ 100 fs FWHM, 30 μm) of OPO and Ti:S pulses in the focus of the microscope. Careful measurement and calculation of optical path length estimates the appropriate zero delay position, d_0, of the Ti:S delay line to within a few millimeters. Beyond

that, d_0 may be found by scanning the inter-pulse time delay with a stepper motor (Newport CMA-25PP) and monitoring some nonlinear process which corresponds to the temporal overlap of both pulses. Ultimately, we monitor the visible and IR FWM signals generated by a sample in the focus of the FWM microscope. However, when first setting up the delay line, in order to avoid complications inherent with detection path alignment and lock-in detection, it is much more convenient and expedient to use an alternative approach.

Figure 5.2 shows the alternative optical setup used to find the approximate zero delay position d_z. Ti:S and OPO beams (35 mW each) are aligned spatially and then focused by a first lens (f = 10 cm) into a 0.01 mm thickness beta barium borate (BBO) nonlinear crystal which enables broadband phase matching. The crystal is used to generate second-order nonlinear effects of the incident fields, including second-harmonic generation (SHG) and sum frequency generation (SFG). A second lens (f = 5 cm) collimates the output resulting in a demagnification of the input beam radius. The beam then passes through a BK7 prism resulting in spatial separation of the incident wavelengths of light. A cylindrical lens (f = 10 cm) is then inserted to focus this signal light onto a paper screen, maintaining the spatial separation between wavelengths of light. Immediately present on the screen are spatially resolved signals corresponding to SHG of both the Ti:S (394 nm) and OPO (513 nm). Scanning the length of the Ti:S delay path to search for d_z, a third color appears between the SHG patterns which corresponds to SFG of the Ti:S and OPO (445 nm). This SFG signal is only present when Ti:S and OPO pulses are temporally overlapped and is taken to be maximum at d_z. This technique allows one to scan for the position of d_z at a rate of ≈ 1 mm/s. Searching for d_0 in the FWM microscope allows one to scan only ≈ 60 μm/s because of averaging in the lock-ins. Once d_z is found, d_0 is easily found in the FWM microscope.

Ultimately, the inter-pulse delay time was scanned (delay convention of Fig. 5.3)

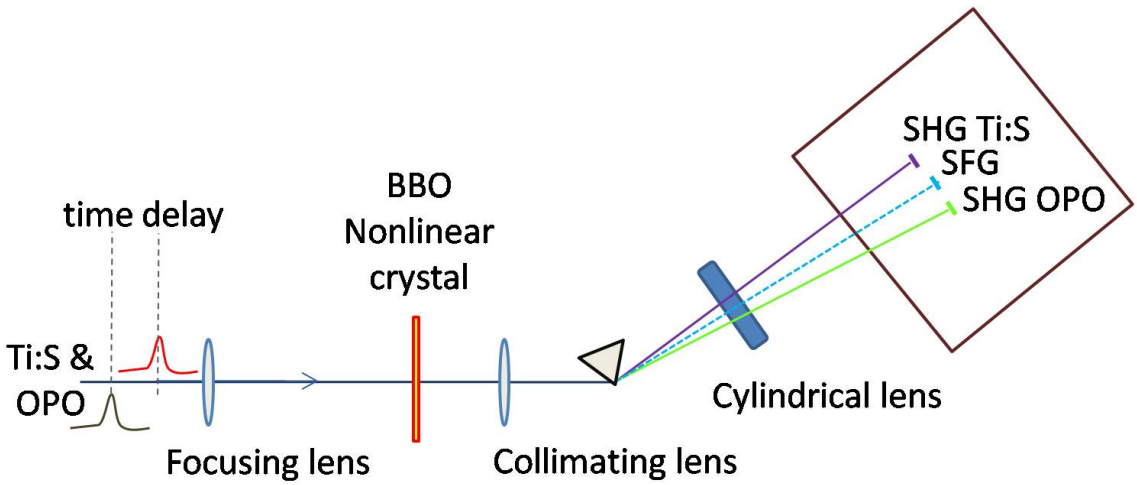

Figure 5.2: Optical layout of the method used to find zero delay between Ti:S and OPO pulses.

within a few hundred fs of d_0 resulting in IR FWM and visible FWM signals that correspond to moving one pulse past the other in time. Initially, these were expected to be simple cross-correlation signals, but proved to be more complicated.

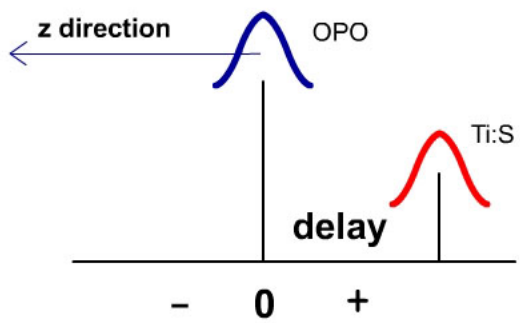

Figure 5.3: Inter-pulse delay convention. Delay is positive when the Ti:S pulse trails the OPO pulse to sample.

To aid in collecting FWM signal data versus the inter-pulse delay time, a LabVIEW program was written to coordinate motion of the delay scan motor and data capture from the lock-in amplifiers. Sequentially, this program moves the motor,

waits a set amount of time, and collects one data point per channel. In repetition, this constructs a data set of FWM signal data vs. inter-pulse delay time. The motor step size (0.3 μm minimum), number of total steps, and wait time between steps are all user defined. This program allows for arbitrary wait time between each step of the motor and its corresponding data acquisition. In practice, the minimum wait time enacted between successive motor steps is 500 ms. This practical limit allows three processes to happen. First, the motor must complete it's motion and come to rest. Second, any vibrations coupled into the optical system by mechanical contact with the motor must stabilize. Third, sufficient time must pass for the lock-in amplifiers to average the equilibrated signal before data capture can occur.

For typical lock-in time-constant values of 10-50 ms, data taken with 500 ms delay between successive motor steps accurately mimics data taken at much longer delays, 5-10 s, and thereby demonstrates it's efficacy, precluding any time scale effects that exceed several seconds in duration. It should be noted that time-constant values of 50 ms yielded minimum signal to noise ratios (S/N) of 110:1. More commonly, for both IR and visible FWM signals S/N $>$ 250 : 1. Increasing the time-constant value on the lock-in did not alter measurably the signal to noise ratio. It is suspected that the major contributor to the remaining noise is due to detection of scattered light from the chopped beam. This hypothesis is supported in part by observing that the absolute value of the noise level scales linearly with the power of the chopped beam even when the beam is blocked before entering the focusing objective.

5.2 Time dependent behavior of four-wave mixing signals

From Section 2.1, recall that in order to consider Eq. (2.2) to be valid in the time domain we must assume a material without loss or dispersion such that $\chi^{(n)}(\omega)$ may be considered to possess entirely real constant value independent of frequency. To understand why these conditions make Eq. (2.2) valid in the time domain, consider the first order term for the induced material polarization in the frequency domain:

$$P^{(1)}(\omega) = \chi^{(1)}(\omega)E(\omega). \tag{5.1}$$

To determine the material response as a function of time, $P^{(1)}(t)$, we Fourier transform the frequency domain expression of Eq. (5.1). Recalling that the Fourier transform of a product equals a convolution of the Fourier transform of each factor, we arrive at Eq. (5.2) where we have asserted the Fourier transforms of each factor: $\mathscr{F}[\chi^{(1)}(\omega)] = \chi^{(1)}(t')$ and $\mathscr{F}[E(\omega)] = E(t')$.

$$P(t) = \int_{-\infty}^{\infty} \chi^{(1)}(t')E(t-t')dt' \tag{5.2}$$

Now considering $\chi^{(1)}(\omega)$ for a lossless dispersionless material with frequency independent response, $\chi^{(1)}(\omega)$ = constant and it's Fourier transform must be a delta function, $\chi^{(1)}(t') = \chi_0^{(1)}\delta(t)$. Inserting this result into the convolution of Eq. (5.2) leads to

$$P(t) = \chi_0^{(1)}E(t) \propto E(t) \tag{5.3}$$

where $\chi_0^{(1)}$ is a constant 'weight' factor and $P^{(1)}(t)$ is shown to follow the driving electric field in a direct instantaneous manner.

Using similar arguments we may derive the time dependent material polarization for both visible and IR FWM processes with two source illumination (cf. Fig. 2.2)

where ω_1 and ω_2 correspond to the angular frequencies of the Ti:S and OPO respectively. Beginning with the frequency domain expression for visible FWM [15],

$$P(2\omega_1 - \omega_2) = 3\chi^{(3)}(\omega)E_1^2(\omega_1)E_2^*(\omega_2) \tag{5.4}$$

and assuming $\chi^{(3)}(\omega) = \text{constant}$, the polarization may be written in the time domain as [15]

$$P(t) \propto E_1^2(t)E_2^*(t). \tag{5.5}$$

This polarization depends on the overlap of two phase incoherent pulses and we may write the expression for material polarization as a function of the interpulse delay, τ:

$$P(\tau) \propto \int_{-\infty}^{\infty} \left[E_1^2(t-\tau)E_2(t)\right] dt \tag{5.6}$$

As expected, this describes the case for FWM in the approximation of instantaneous material response (with pulses much longer than the material response time) [100]. Accounting for the detection of optical intensity (cf. Eq. (2.3)), the detected visible FWM signals scale according to Eq. (5.7). Here the detector response is assumed constant because of the lock-in and is absorbed into the signal proportionality.

$$S_{VFWM}(\tau) \propto \int_{-\infty}^{\infty} \left[E_1^2(t-\tau)E_2(t)\right]^2 dt \tag{5.7}$$

Following the same procedure for the case of IR FWM, where the frequency domain expression for the material polarization is given by

$$P(2\omega_2 - \omega_1) = 3\chi^{(3)}(\omega)E_2^2(\omega_2)E_1^*(\omega_1) \tag{5.8}$$

we arrive at Eq. (5.9).

$$S_{IRFWM}(\tau) \propto \int_{-\infty}^{\infty} \left[E_1(t-\tau)E_2^2(t)\right]^2 dt \tag{5.9}$$

For inter-pulse delay scan measurements, IR and visible FWM signals follow Eqs. (5.9) and (5.7) where E_i is approximated by a Gaussian shaped pulse envelope

$$E_i(t) = exp\left(-2ln(2)\frac{t^2}{\tau_p^2}\right) \tag{5.10}$$

where τ_p is the duration (FWHM) of the resulting temporal intensity profile. For the case of pulsed illumination, Eqs. (5.9) and (5.7) are conveniently expressed in terms of the time delay, τ, between Ti:S and OPO pulses using the convention of Fig. 5.3 where a positive delay indicates that the Ti:S pulse follows the OPO pulse in the direction of propagation. Numerical evaluation of Eqs. (5.7) and (5.9) using measured pulse durations of the Ti:S and OPO (60 fs, 100 fs), are shown in Fig. 5.4. We see that the IR and visible FWM signals share a common center and the FWHM of the IR FWM is slightly less than that of the visible FWM.

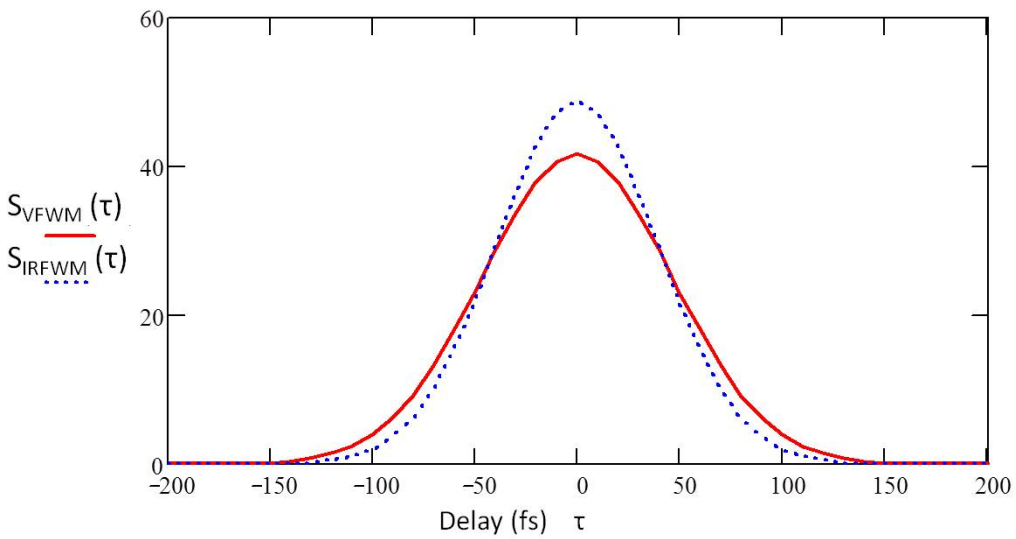

Figure 5.4: A numerical plot of visible and IR FWM signals predicted by Eqs. (5.7) and (5.9) for an interpulse delay scan of Ti:S (60 fs) and OPO (100 fs) pulses.

Figure 5.4 represents the case where a material has an instantaneous response to the incident waves E_1 and E_2, and the signal at a given delay, τ, is determined by the temporal overlap of the pulses. The effect of temporal overlap on the total signal

is shown pictorially in Fig. 5.5. The top plot shows both the individual components of Eq. (5.7) for inter-pulse delay $\tau = 50$ fs, $E_1^2(t-50)$ and $E_2(t)$, as well as their resulting product, $f(t) = E_1^2(t-50)E_2(t)$. The integrated area contained under the product $f(t)$, $A(\tau = 50$ fs$)$, gives the value of the simulated visible FWM signal for interpulse delay $\tau = 50$ fs as shown in the lower plot of Fig. 5.5.

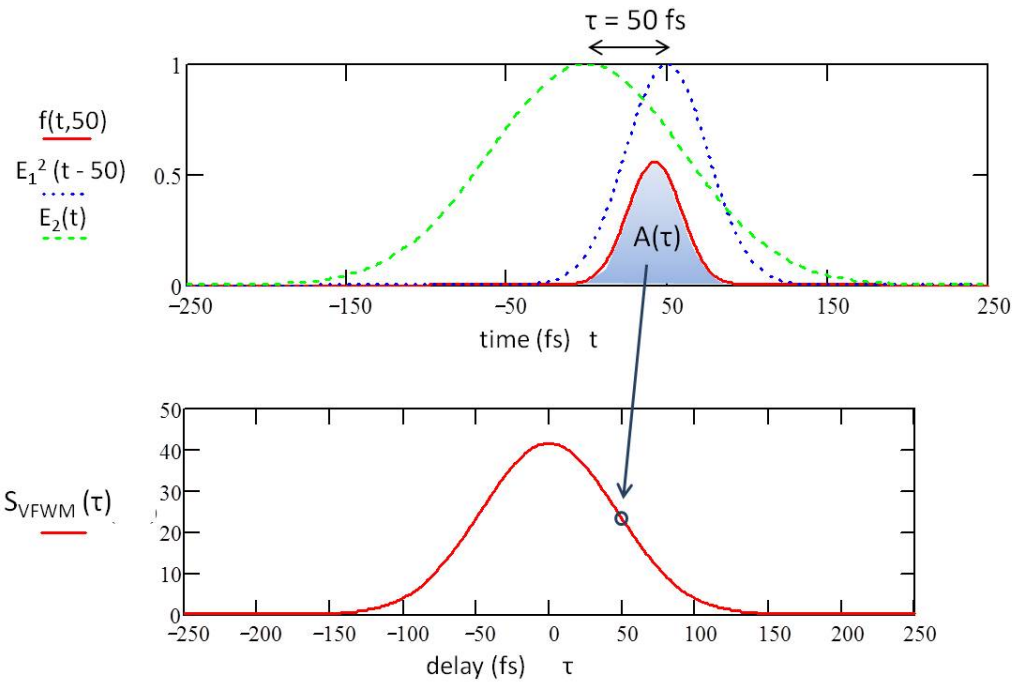

Figure 5.5: (top) Plots of E_1^2 and E_2 and their resulting product for a fixed inter-pulse delay, $\tau = 50$ fs. (bottom) Plot of visible FWM signal (cf. Eq. (5.7)) for an inter-pulse delay scan. The area $A(\tau = 50$ fs$)$, gives the value of the visible FWM signal at $\tau = 50$ fs.

5.3 Four-wave mixing inter-pulse delay scan measurements in solvents

Consider the results for an inter-pulse delay scan measurement, Fig. 5.6a, using the setup shown in Fig. 5.1 with a liquid butanol sample of thickness ≈ 340 μm contained between two pieces of BK7 coverglass. The delay is scanned over a range of 600 fs surrounding the supposed zero delay, d_0. The resolution of this scanning measurement depends on the minimum step enacted by the delay scan motor (0.3 μm, 1 fs.) For a double pass through the delay line, this resolution is 2 fs. The IR FWM and visible FWM signals have centers (peaks) that are clearly separated from one another along the delay axis. It should be noted that here and throughout the chapter, the delay scale shown for measurements is a relative one and does not indicate the position of true zero delay between the excitation pulses. This is chosen in order to stress the uncertainty in the position of zero delay for separated FWM signal peaks. Since these results deviate from the signals expected for instantaneous material response, Fig. 5.4, this suggests that butanol may exhibit a finite material response time probed by this experiment. If true, the induced material polarization can no longer be considered instantaneously dependent on the driving electric fields, but exhibits some memory of the fields arriving at earlier times. If one naively assumes that the true zero delay position lies between the two signal peaks, then using the delay convention of Fig. 5.3 it would be determined that the IR FWM signal has a maxima when the Ti:S pulse leads the OPO pulse to the sample. Conversely the visible FWM signal has a maxima when the Ti:S pulse trails the OPO to the sample. Such an assumption about d_0 is helpful for describing the relative delay of the Ti:S pulse, but awaiting forthcoming evidence, the absolute value of d_0 is briefly held in question.

To quantify the delay separation between optical signals, both IR and visible

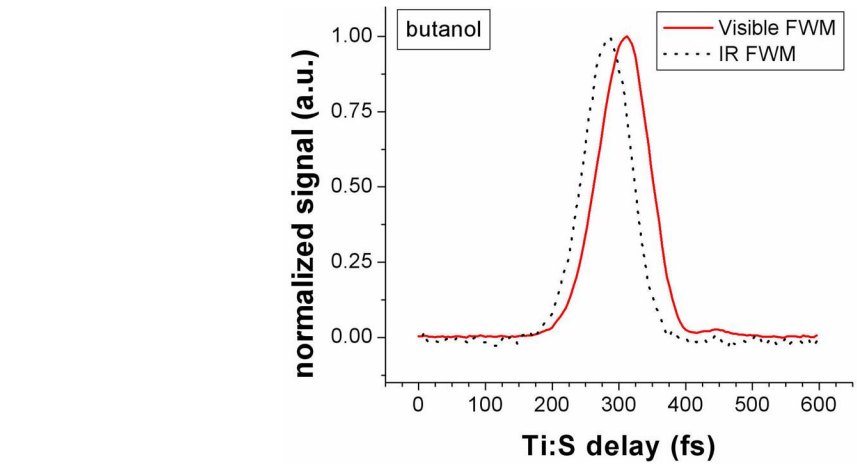

(a)

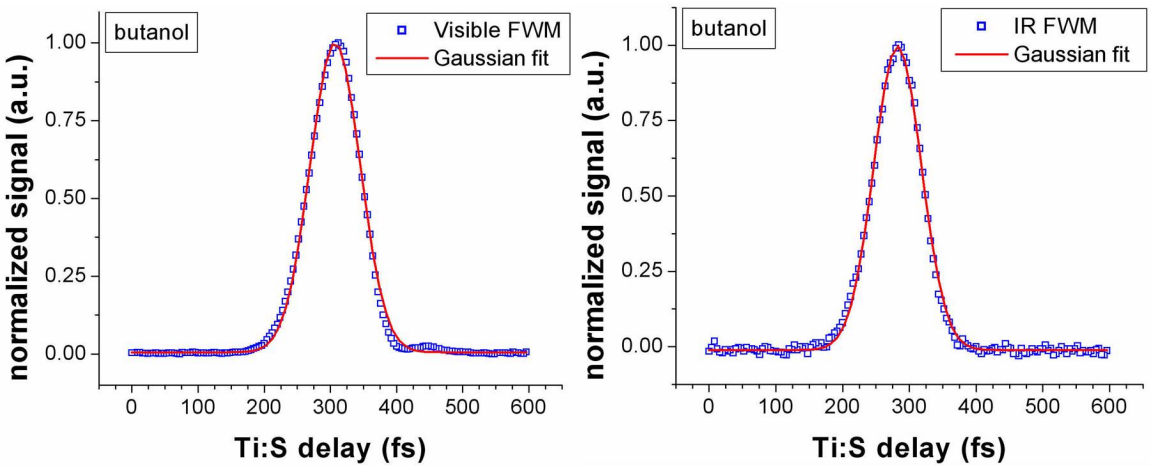

(b) (c)

Figure 5.6: (a) Delay separation (-24.8 fs) for an inter-pulse delay scan measurement in butanol. (b)Visible and(c) IR FWM signals with Gaussian fit for the same inter-pulse delay scan measurement.

FWM signals are shown to be well matched by a Gaussian fit, Figs. 5.6c and 5.6b respectively. As is expected from numerical evaluation of Eqs. (5.7) and (5.9), the measured IR FWM signal has slightly narrower FWHM (72 fs) than the visible signal FWHM (76 fs). From these Gaussian fits the signals' centers are obtained. For butanol the difference between IR and visible FWM signal centers is -24.8 fs.

The separation values of IR FWM - visible FWM signal centers for other samples are given in Table 5.1 for inter-pulse delay scans in fused silica and BK7 glass, as well as methanol, ethanol, propanol, butanol, and hexane liquid solvents. The solvents all display significant ($>$ 1 fs magnitude) IR-visible FWM delay separation where the absolute value of the separation is observed to increase with the number of carbon atoms in the molecule, cf. Fig. 5.7. Such dependence may be reliant on the second hyperpolarizabilities of these molecules as shown in [68]. In short, the alcohols were shown to display signal strength following from a bond additivity model where each bond contributes to the second hyperpolarizability. The results with hexane were similar but did not follow the same bond additivity model. The inference is that large second hyperpolarizabilitites (large signals) result from longer molecules, and longer molecules have larger inertia (longer characteristic material times) leading to a larger delay separation observed here. It is noted that the delay separation between these signals is observed to be constant regardless of both focal depth inside the material and the chirp of the Ti:S and OPO laser pulses.

Sample material	delay (fs) IR-Vis FWM
Fused Silica	-0.6
BK7	-0.9
Methanol	-18.9
Ethanol	-23.4
Propanol	-24.3
Butanol	-24.8
Hexane	-28.3

Table 5.1: FWM inter-pulse delay scan data for visible and IR signals in BK7, fused silica, PMMA, and sapphire. The IR-Vis delay is derived from Gaussian fits of data. All uncertainties $< \pm$ 1.5 fs.

From viewing the data for all the liquid samples on the same delay scale we can compare the absolute positions of both the IR FWM signals, Fig. 5.8a, and the

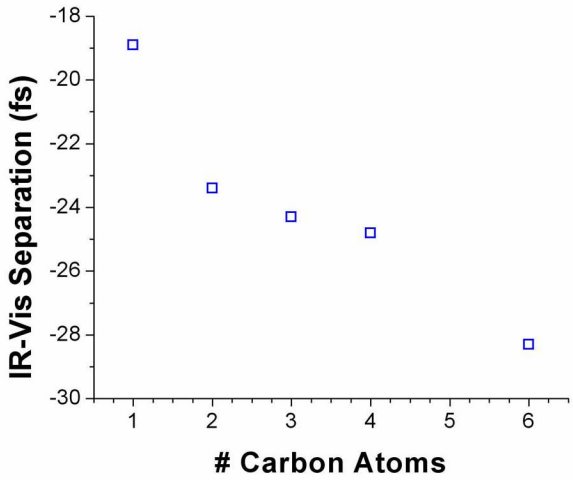

Figure 5.7: IR-Vis separation dependence on the number of carbon atoms in the solvent molecule.

visible FWM signals, Fig. 5.8b. Such comparison allows insight into both the true zero delay position and the type of resonant FWM process which probes a finite material response. It is observed that the IR FWM signals share a common center position to within the tolerance of jitter imposed by the motor from run to run ($\pm$ 2 fs). Since all IR FWM signals share a common center regardless of sample, this is designated as the true value of d_0. Additionally, it suggests that IR FWM signals do not display the effects of probing a finite material memory. For IR FWM, the total signal appears to be dominated by a material response following instantaneously from the driving fields. A resonant IR FWM process may occur but exhibits either insufficient strength (proportion of the total signal), or fast response compared to the pulse durations used here, $\ll \tau_p$, or both. In contrast, the visible FWM signals all shift toward positive delay and appear to be dominated by a resonant process probing a finite material response time of similar duration to the pulses used here.

Specifically, since the materials all respond on a fs time scale, the visible FWM signals probe a characteristic dephasing time of the solvents. Since a finite dephasing time must be linked to an energy level within the material, the probing of such a finite

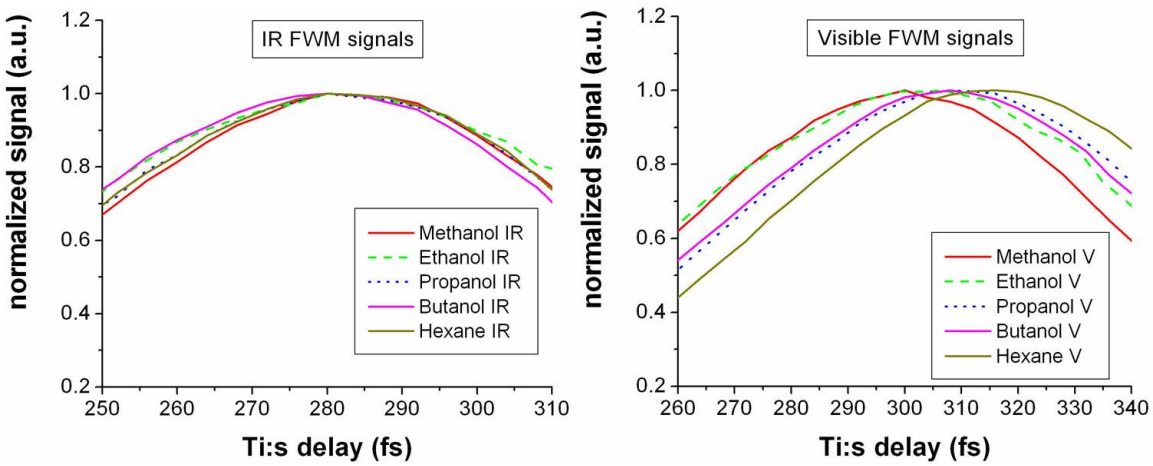

(a) (b)

Figure 5.8: (a) IR FWM signals from methanol, ethanol, propanol, butanol and hexane on the same scale. They share a common center to within ± 2 fs. (b) Corresponding visible FWM signals with solvent-specific center positions.

material response implies ordering of the photon interaction with respect to the level being probed. Four-wave mixing processes with explicit time ordering of the photon interactions are shown in Fig. 5.9. For example, the process of visible stimulated parametric emission (SPE) is described as follows. We assume only one energy level with non-instantaneous response. After two photon absorption of the Ti:S at 787 nm, the induced material polarization oscillates coherently for a duration described by the finite material response time, T. During this period of coherent oscillation by the ensemble of oscillating dipoles, the OPO photon interaction (1025 nm) and simultaneous signal photon generation can occur at any time. In order to examine which FWM process provides the correct delay response leading to a positive shift in visible FWM signals on the delay axis, numerical modeling is implemented again.

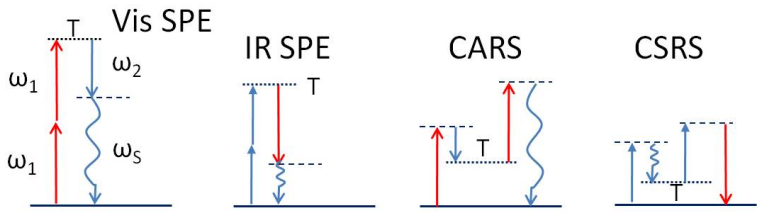

Figure 5.9: Photon energy level diagrams of resonant FWM processes with ordering of the photon interactions with respect to the level with finite response. Dotted lines indicate the presence of a material characteristic dephasing time, T, for visible stimulated parametric emission (SPE), IR SPE, coherent anti-Stokes Raman scattering (CARS), and coherent Stokes Raman scattering (CSRS.)

5.4 Resonant perturbation of the time dependent behavior of four-wave mixing signals

In what follows, we seek to model FWM signals corresponding to a finite material response in order to correlate the results of Fig. 5.8 with a resonant process generating the observed separation of IR-visible FWM signal centers. Since IR FWM signals seem to be dominated by processes with instantaneous material response, we must look for a visible FWM process which exhibits the proper time delay shift in signal center. Beginning with the equations for visible and IR FWM with instantaneous response, Eqs. (5.7) and (5.9) respectively, we discuss a perturbative approach to determining time dependent expressions for modeling inter-pulse delay scans in media with finite material response. These expressions are shown to be different for the processes of visible SPE, IR SPE, CARS, and CSRS.

It should be noted that FWM signals have been described generally for the cases where the pulse durations involved are either much shorter than or much longer than the characteristic response time of the material being probed [100]. The results presented here do not agree with either of those assumptions and likely represent the case where the pulse durations involved are nearly equal to the response time of

the material. This relationship between pulse duration and material response time presents considerable obstacles to the derivation of analytical solutions for the FWM signals. For this reason, we turn to an approach that starts with solutions to the instantaneous response case and includes a simple perturbation to include a finite material response time. To inform the perturbation we turn to what is known about CARS, which is certainly the most thoroughly studied FWM process, and apply those results to all the FWM processes examined here.

We know from Section 5.3, that Eqs. (5.7) and (5.9) describe visible and IR FWM signals for inter-pulse delay scans (cf. Fig. 5.4) when the time response of the material is instantaneous. Here we use a perturbative approach to include in these equations the effect of a material response corresponding to resonant (non-instantaneous) behavior of the material. Using the example of visible SPE, we show how one may include such a resonant response.

Suppose that the visible FWM process probes a finite material response time, T, at the two photon absorption level of the Ti:S (E_1, ω_1). This would be described by the visible SPE process shown in Fig. 5.9. To make it clear how T may be incorporated into the expression for visible SPE, it is helpful to rewrite the expression for instantaneous response (Eq. (5.7)) in terms of two coherent induced material polarizations

$$S_{VFWM}(\tau) \propto \int_{t_1}^{t_2} \left[E_1^2(t-\tau)E_2(t)\right]^2 dt \propto \int_{-\infty}^{\infty} \left[P_1 P_2\right]^2 dt \tag{5.11}$$

where $P_1 \propto E_1^2$ and $P_2 \propto E_2$. Immediately we see that the induced material polarization P_1 corresponds to two photon absorption of the Ti:S. In order to include a finite material response time typical of visible SPE, P_1 is no longer considered directly proportional to E_1^2, but is supposed to follow from the relationship

$$\left[\frac{d}{dt} + \frac{1}{T}\right] P_1 \propto E_1^2 \tag{5.12}$$

which describes adding 'inertia' with with characteristic time, T, at the level of two

photon absorption of the Ti:S laser, E_1^2. Such an approximation is used here for it's similarity in describing the inclusion of a dephasing time in the CARS FWM coupled amplitude equations [101]. Solving this linear first-order differential equation with the method of integrating factors, we find the time dependent expression for P_1,

$$P_1 \propto \int_{t_1}^{t} E_1(x-\tau)E_1(x-\tau)e^{\frac{x-t}{T}}dx \tag{5.13}$$

where x is another time variable. We now have expressions for P_1 for both instantaneous and finite material response:

$$P_1(t,\tau,T) \propto \begin{cases} E_1^2(t-\tau) & \text{for instantaneous material response} \\ \int_{t_1}^{t} E_1(x-\tau)E_1(x-\tau)e^{\frac{x-t}{T}}dx & \text{for finite material response, } T \end{cases} \tag{5.14}$$

Substituting Eq. (5.13) into Eq. (5.11) we obtain the equation for visible SPE signals in a material with finite material response corresponding to two photon absorption of the Ti:S (Fig. 2.5):

$$S_{VSPE}(\tau,T) \propto \int_{t_1}^{t_2} \left[\left(\int_{t_1}^{t} E_1(x-\tau)E_1(x-\tau)e^{\frac{x-t}{T}}dx \right) E_2(t) \right]^2 dt. \tag{5.15}$$

Examining Eq. (5.15), we note several important facts. First, as should be expected, when Eq. (5.15) is evaluated in the limit that $T \to 0$, it reduces back to Eq. (5.7) indicative of visible FWM signals from a material with instantaneous response. Second, considering fixed values of the inter-pulse delay, τ, and finite material response time, T, the effect of the inner integral is more readily understood. For this case, the last term in the inner integral, when $x = t$, corresponds to the contribution of E_1^2 found in the instantaneous response equation. For $x < t$, the inner integral includes a residual contribution of E_1^2 from all earlier times as well, indicating a so-called material memory with characteristic lifetime T.

To begin to examine the effect that this material memory impresses on visible SPE optical signals, we plot P_1, Fig. 5.10, for cases of both instantaneous and finite

material response according to Eq. (5.14). Compared to the instantaneous response of $E_1^2(t-\tau)$ (Eq. (5.10), Ti:S pulse duration $\tau_p = 60$ fs, $\tau = 0$), $P_1(t,\tau,T)$ for finite material response (Eq. (5.13), $\tau = 0$, $T = 60$ fs) exhibits both a positive shift of the peak position in time and a broadened asymmetric temporal profile. Consulting Fig. 5.5, we see that such a positive shift in P_1 leads directly to a negative shift in the visible FWM signal center. This becomes obvious when considering that the Ti:S pulse, E_1, must now lead the OPO pulse, E_2, to the sample in order for P_1 and E_2 to share a common peak at $t = 0$. This negative shift in visible FWM signal center does not correspond to the observed FWM signals in Fig. 5.8. To account for the observed results we also consider the effects of including a finite material response in IR SPE, CARS and CSRS processes. A more comprehensive analysis of visible SPE signals according to Eq. (5.15) continues in Section 5.4.1.

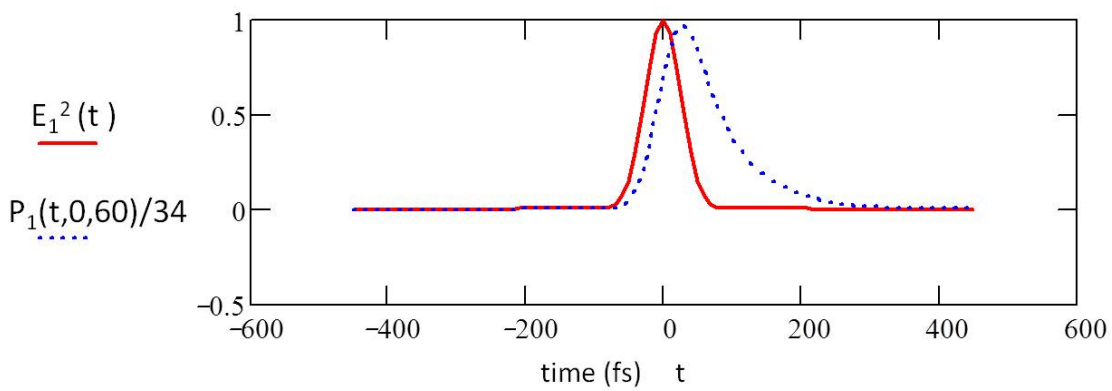

Figure 5.10: Comparison plots of P_1 for instantaneous material response ($E_1^2(t)$) and finite material response ($P_1(t,\tau,T)$) according to Eq. (5.14) in the time domain assuming $\tau = 0$ so that E_1 is centered at $t = 0$.

5.4.1 Mathematical model of finite material response in infrared and visible stimulated parametric emission

The preceding few paragraphs outlined how we reach the expression for visible SPE signals in a material with a finite response present for two photon absorption of the Ti:S: Eq. (5.15). Starting from Eq. (5.9) and applying the same arguments, we determine the expression for IR SPE signals in a material with finite response for two photon absorption of the OPO (Fig. 2.5):

$$S_{IRSPE}(\tau, T) = \int_{t_1}^{t_2} \left[\left(\int_{t_1}^{t} E_2(x) E_2(x) e^{\frac{x-t}{T}} dx \right) E_1(t-\tau) \right]^2 dt. \tag{5.16}$$

The form is identical to that of Eq. (5.15) except that we have solved

$$\left[\frac{d}{dt} + \frac{1}{T} \right] P \propto E_2^2 \tag{5.17}$$

for two photon resonance of the OPO.

A numerical evaluation of Eqs. (5.15) and (5.16) is shown in Fig. 5.11 for $T = 2$, 30 and 60 fs with Gaussian pulses E_1 and E_2 (cf. Eq. (5.10)) of duration $\tau_p = 60$ fs (Ti:S) and 100 fs (OPO) respectively. This model verifies that for a finite material response time, visible SPE displays a shift of the signal center toward negative delay, $\tau < 0$. A negative inter-pulse delay means that the visible SPE signal has a center (peak) when the Ti:S pulse leads the OPO pulse to the sample. Conversely, IR SPE displays a shift of the signal center toward positive delay, $\tau > 0$. These signals do not correlate to the observed IR-vis FWM signal separation of Fig. 5.8.

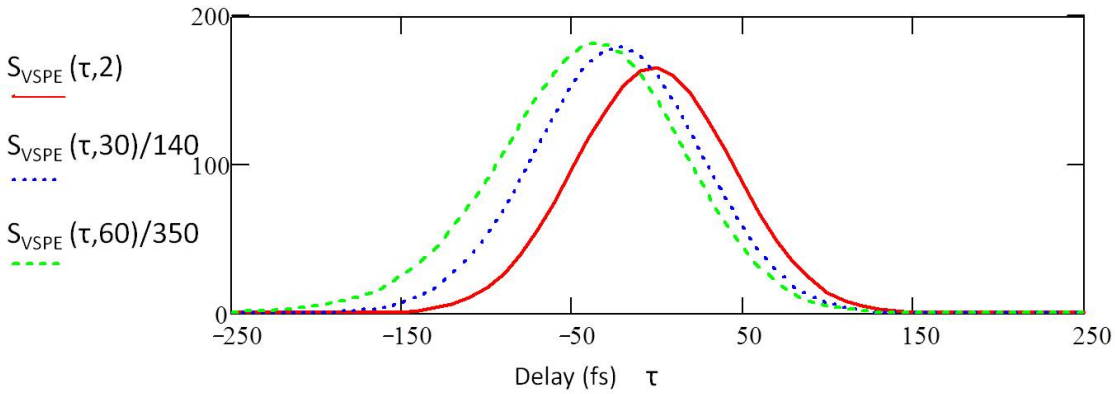

(a)

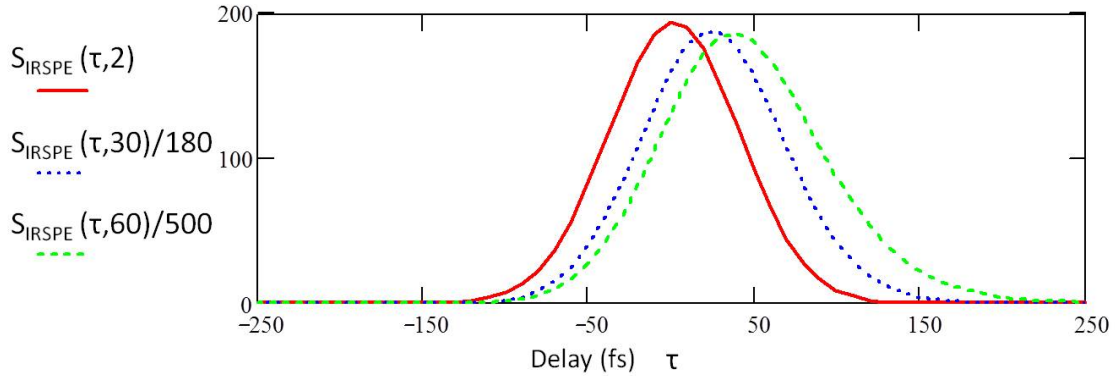

(b)

Figure 5.11: Numerical plots of (a)visible SPE and (b)IR SPE from Eq. (5.15) and Eq. (5.16) respectively for increasing values of the finite material response time: $T = 2,\ 30,\ 60$ fs.

5.4.2 Mathematical model of finite material response in coherent anti-Stokes Raman scattering and coherent Stokes Raman scattering

Starting from Eq. (5.7) for instantaneous response of visible FWM signals and applying the process outlined in Section 5.4, we determine the expression for CARS

signals in a material with finite response as shown in Fig. 5.9:

$$S_{SVIS}(\tau, T) = \int_{t_1}^{t_2} \left[\left(\int_{t_1}^{t} E_1(x-\tau) E_2(x) e^{\frac{x-t}{T}} dx \right) E_1(t-\tau) \right]^2 dt. \tag{5.18}$$

Again, the form is identical to that of Eq. (5.15) except that we have solved

$$\left[\frac{d}{dt} + \frac{1}{T} \right] P \propto E_1 E_2 \tag{5.19}$$

indicating a finite material response for simultaneous interaction of Ti:S and OPO photons. Starting from Eq. (5.9) for instantaneous response of IR FWM signals and substituting the same solution for Eq. (5.19) we derive the expression for CSRS signals in a material with finite response as shown in Fig. 5.9:

$$S_{SIR}(\tau, T) = \int_{t_1}^{t_2} \left[\left(\int_{t_1}^{t} E_1(x-\tau) E_2(x) e^{\frac{x-t}{T}} dx \right) E_2(t) \right]^2 dt \tag{5.20}$$

A numerical evaluation of Eqs. (5.18) and (5.20) is shown in Fig. 5.12 for $T = 3$, 30 and 100 fs with Gaussian pulses (E_1, E_2, cf. Eq. (5.10)) of duration $\tau_p = 60$ fs and 100 fs respectively. For a finite material response time, CARS displays a shift of the visible FWM signal center toward positive delay, $\tau > 0$. Conversely, CSRS displays a shift of the IR FWM signal center toward negative delay, $\tau < 0$. This model correlates with what we observe for inter-pulse delay scans. It appears that a finite material response corresponding to the CARS process accounts for the measured separation between visible FWM and IR FWM signals shown in Fig. 5.8. This model suggests a material dephasing time on the order of 100 fs for all the solvents inspected here.

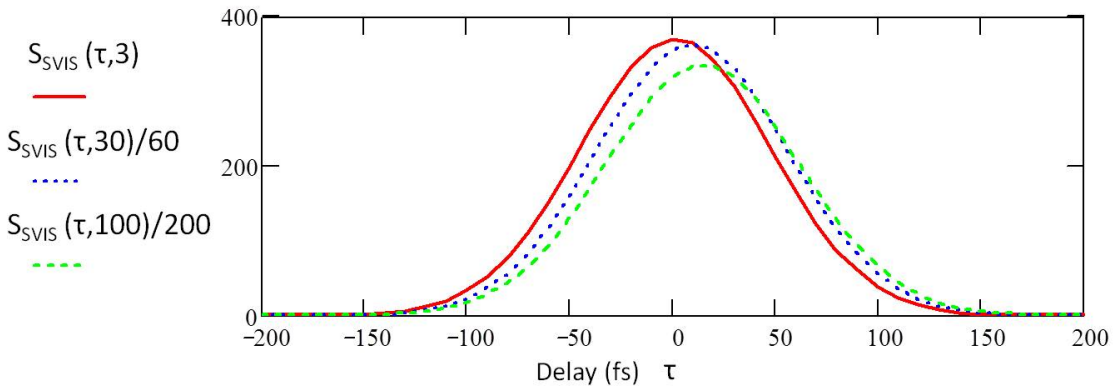

(a)

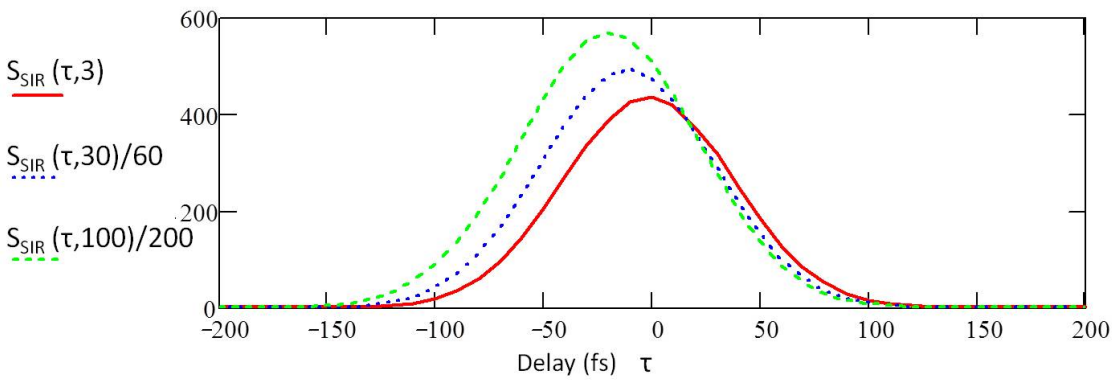

(b)

Figure 5.12: Numerical plots of (a)CARS and (b)CSRS from Eq. (5.18) and Eq. (5.20) respectively for increasing values of the finite material response time: $T = 3,\ 30,\ 100$ fs.

5.5 Determination of the dominant resonant four-wave mixing signal via stimulated parametric emission polarization scheme

For inter-pulse delay scans, the observed IR-visible FWM signal separation of Fig. 5.8 is predicted by modeling the visible FWM signal with a resonant CARS process

($T \approx$ 90-100 fs) as shown in Fig. 5.12. We may further confirm this resonant CARS process as the source of IR-visible FWM signal separation by recording inter-pulse delay scans while implementing the IR SPE polarization scheme [51] discussed in Section 2.2.3. Such a polarization scheme was developed in order to isolate resonant IR FWM signals from nonresonant IR FWM signals at identical signal wavelength for the benefit of enhanced imaging contrast of resonant media. However, it may also lead to suppression of resonant visible FWM signals. Even by partial suppression of visible FWM resonant signals we may expect to observe a decrease in the IR-visible FWM signal separation. Simultaneously, we may confirm that the IR FWM signals remain centered at the same delay position even when isolating signals from resonant IR SPE. This would indicate the case where a resonant IR SPE process is present, but with material response much shorter than the duration of the illuminating pulses, $T \ll \tau_p$, so that it does not result in a delay shift of IR FWM signal centers.

We repeat inter-pulse delay scans in methanol, ethanol, propanol, butanol, and hexane liquid solvents with the IR SPE polarization scheme of Fig. 2.6 where $\alpha = 45°$, $\phi = 71.6°$ and $\beta = 135°$ so as to yield maximal contrast in resonant IR SPE signals. For all samples, the resulting IR-visible FWM signal separation is negligible, $\approx$ -0.4 fs $\pm$ 0.4 fs. The interpulse delay scan for hexane with IR SPE polarization detection is shown in Fig. 5.13. For collinearly polarized excitation, inter-pulse delay scans in hexane exhibited the largest IR-visible signal separation of the solvents interrogated here, -28.3 fs (cf. Table 5.1). Using IR SPE polarization detection, the remaining IR-visible signal separation in hexane is negligible, -0.2 fs. By repeating the delay scan of Fig. 5.13 with no polarization analyzer in the detection path, we confirm in Fig. 5.14 that the IR FWM signals stay centered at the same delay value while visible FWM signals shift toward positive delay when CARS signals are not suppressed by the polarization analyzer. The plots in Fig. 5.14 are normalized for ease of interpreting the signal delay, however is should be noted that by implementing the IR SPE polarization scheme visible FWM signals decrease $\approx 19\times$ and

IR FWM signals decrease ≈ 3.9×. Apparently, the resonant contribution to visible FWM signals is very large.

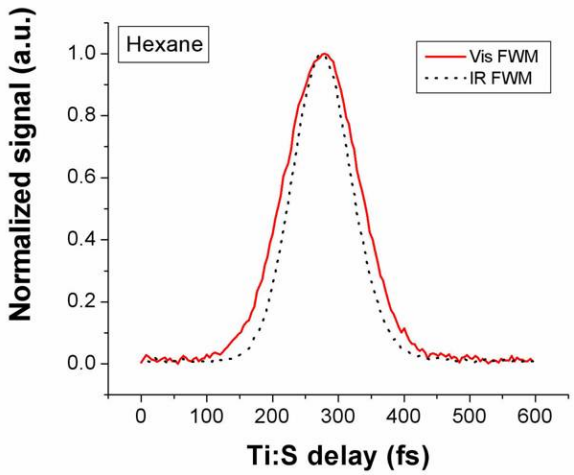

Figure 5.13: IR and visible FWM signals for an inter-pulse delay scan in hexane using the IR SPE polarization scheme of Fig. 2.6. The residual IR-visible FWM signal separation is negligible, ≈ -0.2 fs.

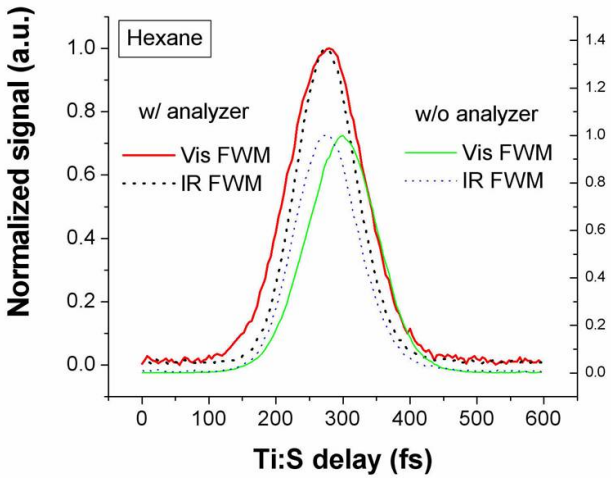

Figure 5.14: IR and visible FWM signals for inter-pulse delay scans in hexane using the IR SPE polarization scheme of Fig. 2.6 with and without the polarization analyzer in the detection path. The visible FWM signal shifts toward higher delay values when CARS signals are not suppressed.

5.6 Chapter Summary

A two pulse FWM microscopy setup was utilized to record IR and visible FWM signals for inter-pulse delay scans in BK7, fused silica, methanol, ethanol, propanol, butanol, and hexane. Delay scan measurements in the liquid solvents revealed characteristic IR-visible FWM signal separation when plotted as a function of delay between pulses. Supposing such signal separation to result from the presence of a finite material response probed by the delay scan experiment, we developed expressions for time dependent FWM signals corresponding to several resonant processes. Through modeling of resonant IR SPE, visible SPE, CARS and CSRS processes, we suggest that the observed IR-visible FWM signal separation corresponds to a resonant CARS process that probes molecular vibrational dephasing with characteristic time on the order of $\approx$ 90-100 fs for all solvents. Due to insensitivity in the modeling, it is not possible to more precisely estimate the characteristic time for each solvent. Through implementation of an IR SPE polarization scheme, we simultaneously isolate resonant IR SPE signals and suppress visible CARS signals. Subsequent inter-pulse delay scan measurements with and without the polarization analyzer confirm what we have modeled: the characteristic IR-visible FWM signal separation is due to the presence of a resonant CARS process in each solvent. Measurements indicate that the resonant contribution accounts for $\approx$ 95% of the total visible FWM signal. The resonant frequency probed in the CARS process is in the range 2770-3130 cm^{-1}, as defined by the spectral FWHM of the excitation sources, and likely indicates the net effects of several Raman active C-H stretch bands near 2950 cm^{-1}.

Chapter 6

Temporal waveform synthesis for nonlinear microscopy

The goal of this chapter is to demonstrate the development and implementation of a genetic algorithm capable of optimizing nonlinear optical signals by interfacing with a spatial light modulator for temporal waveform synthesis of femtosecond regime optical pulses.

6.1 Overview of femtosecond pulse temporal waveform synthesis for nonlinear microscopy

For femtosecond pulses of light, no electronic techniques exist that are fast enough to modulate temporal behavior directly. For this reason, the field of temporal waveform synthesis is typically concerned with controlling the temporal behavior of a pulse by modulating both phase and amplitude in the frequency domain. This is possible because the time domain expression and the frequency domain expression of fem-

tosecond pulses constitute a Fourier transform pair. Modulation in either domain directly effects the other.

The operating principle of modelocked lasers is perhaps the most familiar example for frequency domain synthesis of temporal waveforms. Modelocked lasers support the simultaneous oscillation of many longitudinal modes corresponding to different frequencies of light. When the relative phase between these modes is fixed over one round trip of the cavity, interference between the modes gives rise to a train of pulses. When the phase difference between all the modes of the laser is identically zero at periodically repeated points in time, a train of bandwidth limited pulses is generated. This corresponds to a flat spectral phase, $\phi(\omega) = constant$.

The expression for spectral phase, $\phi(\omega)$, proves to be most useful in describing the role of different components of optical dispersion on the temporal profile of a pulse. Optical dispersion arises because the phase velocity of a light wave ($v = c/n$) has a frequency dependent index of refraction ($n(\omega)$). Considering this frequency dependent index in terms of the applied optical path length difference for the modes of a modelocked laser, we note that the effects of dispersion directly translate to influence on the spectral phase. Most often, the effects of dispersion on spectral phase are described by expanding the spectral phase in a Taylor series around the central frequency of the incident spectrum of light [102]:

$$\phi(\omega) = \phi_0 + \phi_1(\omega - \omega_0) + \frac{1}{2}\phi_2(\omega - \omega_0)^2 + \frac{1}{6}\phi_3(\omega - \omega_0)^3 + \cdots \tag{6.1}$$

In this expansion, the first term is largely ignored and has negligible effect on the temporal pulse shape. The first order phase, ϕ_1, only effects the arrival time of the pulse envelope. The second order term, ϕ_2, indicates the effect of group delay dispersion (GDD) on the pulse and is the first term that has a strong effect on the temporal waveform. Higher order terms also effect the pulse shape.

From Eq. (6.1) many researchers have drawn the inspiration for temporal pulse

shaping [60, 103, 102, 61]. It has become commonplace to implement spatial light modulators (SLMs) composed of liquid crystal pixel masks to control the spectral phase and amplitude directly [59]. While others have developed powerful methods of characterizing the temporal behavior of pulses, we seek to implement a pulse shaping algorithm that will automatically generate the optimal temporal waveform to maximize nonlinear optical signal generation in the focal plane of a microscope.

6.2 A genetic algorithm approach to waveform synthesis

In order to optimize nonlinear optical signals from a coherent process in the focal plane of a microscope, we desire to develop a technique that will work to optimize the temporal waveform automatically without any prior notion of the experiment involved. To enhance our current TH microscope with such a technique requires both incorporation of an SLM based pulse shaper (Coherent Silhouette) and development of a software algorithm to search for a globally optimized signal. This algorithm will seek to optimize signal generation via control of the temporal waveform as implemented by the SLM.

The SLM setup is shown in Fig. 6.1. A prism separates the spectral components of the incoming pulse and together with the curved mirror ensures that spatially separated spectral components arrive perpendicular to the SLM. The distance between the prism and curved mirror as well as the distance between the curved mirror and the SLM are set to be f, the focal length of the curved mirror. With no signal applied to the SLM this $4f$ system results in no change to the input pulse. The SLM contains two liquid crystal masks (128 pixels each) for control of electric field phase and amplitude respectively. Control of both the phase and the amplitude of the elec-

tric field provides the most flexibility in synthesizing temporal waveforms, however, along with that flexibility come considerable complications in testing the algorithm for shaping. In this first attempt, we implement phase control alone. Figure 6.2 shows the resulting position of spectral components on the phase pixel mask of the SLM. At the very least, phase control allows for compensation of the sum dispersion from all the optical components present in the beam path, compensating the effects discussed surrounding Eq. (6.1), up to the limit of 70 radians of phase imposed by the SLM.

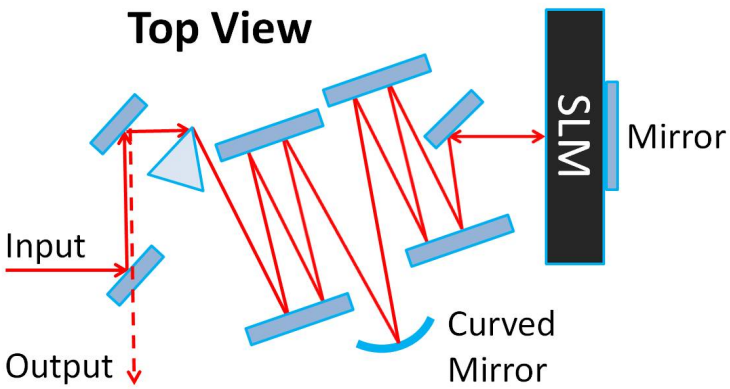

Figure 6.1: Layout of the spatial light modulator (SLM) setup used for temporal pulse shaping. The SLM contains a mirror to reflect the beam back through the setup.

Implementing computer control of the SLM pulse shaper, we may optimize the nonlinear optical signals generated by the shaped pulse simply via parameterization of the SLM pixels. Such an optimization algorithm relies both on control of the SLM pixel mask and on collection of subsequent electronic signals from experimental measurement of nonlinear optical signals. Considering that each of the 128 pixels is adjustable over 2^{12} voltage steps, a linear (sequential) search algorithm over all possible combinations is prohibitively time consuming. For this reason we turn to a learning algorithm that iteratively progresses towards a global maximum. In particular, we invoke a genetic algorithm (GA) so-called for its inspiration following

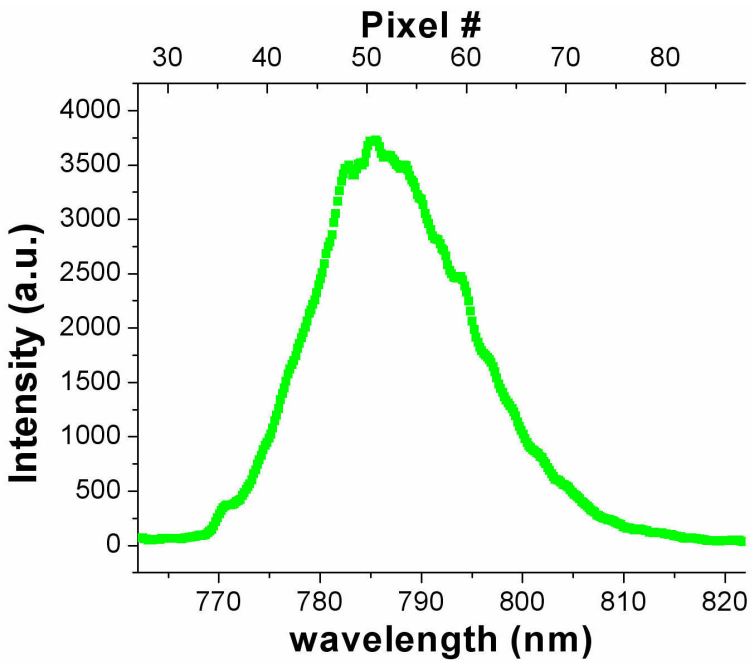

Figure 6.2: Overlaid Ti:S spectrum and corresponding SLM pixel.

from evolutionary biology [104] which treats optimization parameters as interrelated members of a genetic code that serve to improve the overall fitness of a population by progressing from generation to generation (iteration). Discussed in depth in the following section, a GA is chosen here for its reputation as a robust method of optimization. Also importantly, when tailored to the specific problem at hand it may be a very efficient learning algorithm. Furthermore, genetic algorithms comprise a proven method that have been implemented successfully in previous work with temporal waveform synthesis [56, 60, 61].

6.2.1 Overview of the genetic algorithm

Here we describe the function of the specific steps involved in the genetic algorithm of Fig. 6.3 which has been implemented in a LabVIEW programming environment. This

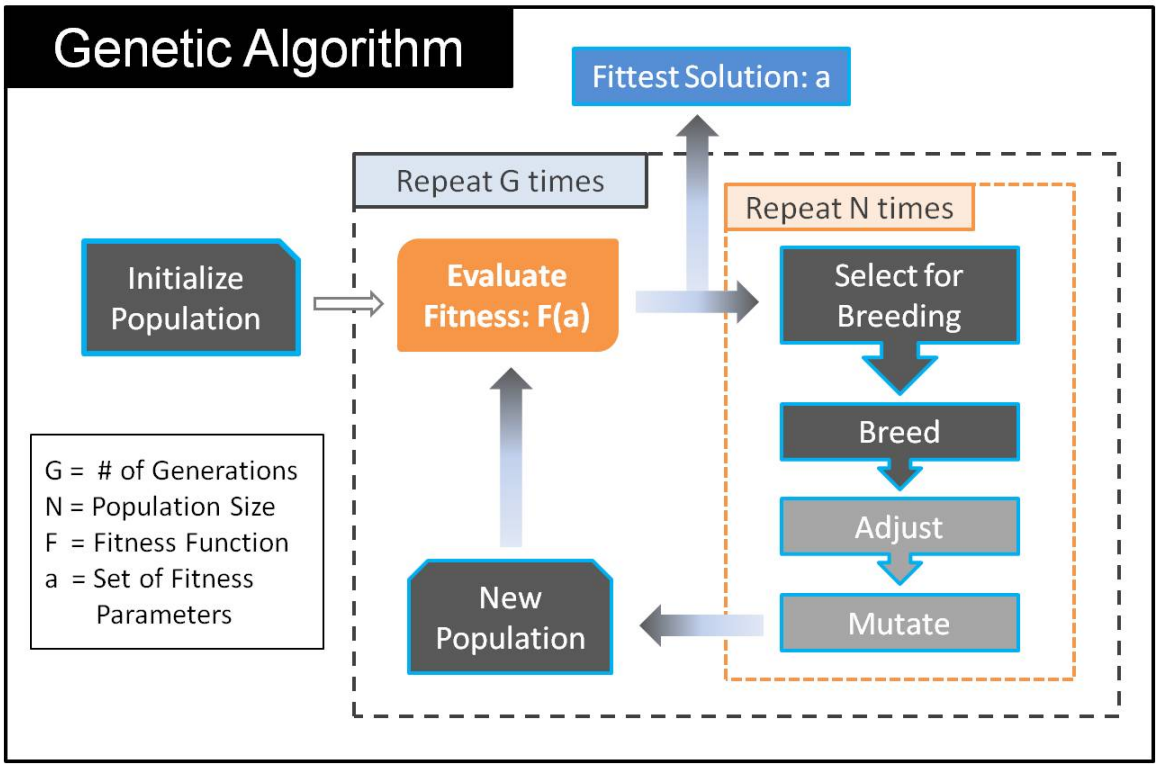

Figure 6.3: Schematic of the implemented genetic algorithm.

algorithm maximizes detected nonlinear optical signals by searching for an optimal set of spectral phase values applied to a femtosecond pulse by the pixels of a liquid crystal phase mask. This may be considered as an optimization carried out over the parameters describing the values assigned to each pixel in the mask.

We develop two variations of the GA which respectively use methods of direct and indirect parameterization of the phase values applied to each pixel. For the case of direct parameterization, the value of each pixel corresponds to its own parameter. For 128 pixels in the phase mask, this version of the algorithm optimizes over 128 separate parameters. The parameter describing the ith pixel is p_i, and the state of the entire phase mask is described by the set of parameters $a(p_1, p_2, ...)$. In this case, the phase value of the ith pixel is simply $v_i = p_i$. For the case of

indirect parameterization, the value of each pixel is determined by a reduced set of parameters, here the coefficients of a 9th order polynomial function, that define the values across the entire pixel mask. For 9 coefficients describing the polynomial, this version of the algorithm optimizes over only 9 separate parameters. For example, the set of optimization parameters for a polynomial function would still be expressed as $a(p_1, p_2, ...)$ but where the phase value of the ith pixel is given by $v_i = p_1(i-c) + p_2(i-c)^2 + p_3(i-c)^3 + \cdots$ where c is the pixel corresponding to the center of the incident pulse spectrum. Indirect parameterization reduces the number of search parameters from 128 to 9 and expedites the search, but it also sacrifices the overall degree of freedom related to the variety of synthesized pulses. A polynomial function makes sense for indirect parameterization of phase values in the pixel mask because the spectral phase distortions caused by dispersive optics, Eq. (6.1), are also expressed as a polynomial in phase. In the very least, parameterization with a polynomial will allow for compensation of dispersion effects on the pulse. It should be noted that certain spectral phase compensations, such as a sinusoid of more than one period, are not handled well by parameterization with a polynomial. In light of these two methods of parameterization, we discuss the specifics of the GA implemented in the following work.

The steps involved in the genetic algorithm are as follows.

1. **Initialize population.** This step generates N sets of parameters, $a(p_1, p_2, ...)$, where the optimization parameters, p_i, are determined at random within a user defined range. Each set of parameters represents a specific state of the phase mask and constitutes a trial solution in the optimization problem. The number of sets, N, is referred to as the population size of the search where each trial solution a is a member of the population. The initialization step produces the first generation of trial solutions.

2. **Evaluate fitness.** This step i) takes each trial solution one at a time, ii) cal-

culates the phase value for each pixel, iii) applies the values to the phase mask and iv) acquires the signal produced in the experiment. The recorded signal is the figure of merit for the trial solution and is referred to as the fitness of the solution, $F(a)$. In analogy to evolutionary mechanisms, the fitness in some way determines the ability of one member of the population to breed and thereby pass along its traits, the parameters p_i, to the next generation.

3. **Select for breeding.** This step selects two trial solutions from the current generation for breeding. The method of selection is important in that it determines what trial solutions are allowed to pass along their traits to the next generation. We implement the commonly used roulette wheel selection method [105] where each trial solution is preferentially assigned a chance of selection based on its fitness relative to the population as a whole. Fitter trial solutions have a higher chance of being selected according to Eq. (6.2). This chance of selection may be visualized as a segment of a roulette wheel. A random spin of the wheel then determines which trial solution is selected for breeding.

$$\text{selection \% for } a_k = \frac{F(a_k)}{\sum_{j=1}^{N} F(a_j)} \tag{6.2}$$

4. **Breed.** This step takes the two trial solutions selected for breeding and combines their traits, parameters p_i, into a new trial solution to be passed on to the next generation. The process by which this combination of parameters is accomplished is known as breeding. The breeding process for direct parameterization is to directly replace parameters in the fitter solution with a fitness weighted percentage of parameters from the less fit solution. Direct replacement is required due to 2π periodicity in the parameter space. The breeding process for indirect parameterization is a fitness weighted averaging of parameters. In this case a weighted average is allowed because the parameters do not suffer from periodicity.

5. **Adjust (optional).** This step has a user defined chance of occuring. This step takes the new trial solution produced by breeding and makes a small adjustment, addition or subtraction, to the value of each parameter. The size of adjustment is chosen to be small enough so that if applied to a single parameter, it has no measurable effect on the fitness of a trial solution. However, when applied to several parameters the net effect may prove to be sufficient to cause a change in the measured fitness of the trial solution. This adjustment allows the overall algorithm to probe coupled parameters and thereby exhibit improved efficiency.

6. **Mutate (optional).** This step has a user defined chance of occuring. This step takes the new trial solution and replaces some of its optimization parameters with new randomly generated parameters. This type of parameter replacement is akin to mutation in a genetic code. In the search algorithm, mutation serves as a way to enact change on a large scale in the search space, perhaps moving away from a local maxima and into another region of optimization.

7. **Repeat steps 3-6.** Steps 3-6 are repeated to generate a new population from the preceding population of trial solutions. The algorithm used here implements elitism which retains the trial solution with the best overall fitness from one generation for inclusion in the next. In this way, the fitness can never decrease more than the limit imposed by experimental noise. Accounting for elitism, steps 3-6 are repeated $N-1$ times to produce a new generation of trial solutions with N members.

8. **Repeat steps 2-7.** Steps 2-7 are repeated for a set number of generations, G, until the algorithm is stopped and subsequently returns the fittest solution obtained through the optimization search.

Figure 6.4 shows a typical progression of fitness as the genetic algorithm pro-

ceeds through several generations. In this case we have simulated the progression of SHG signals assuming that the algorithm needs to search for a quadratic phase compensation. The plot shows the average maximum fitness (with standard deviation) attained over 40 simulations. Since the initial trial solutions are generated randomly, the algorithm essentially starts from noise, yet in 20 generations the algorithm finds a phase compensation resulting in 96% (±1%) of the maximum fitness. For further details on simulation, refer to Appendix B.

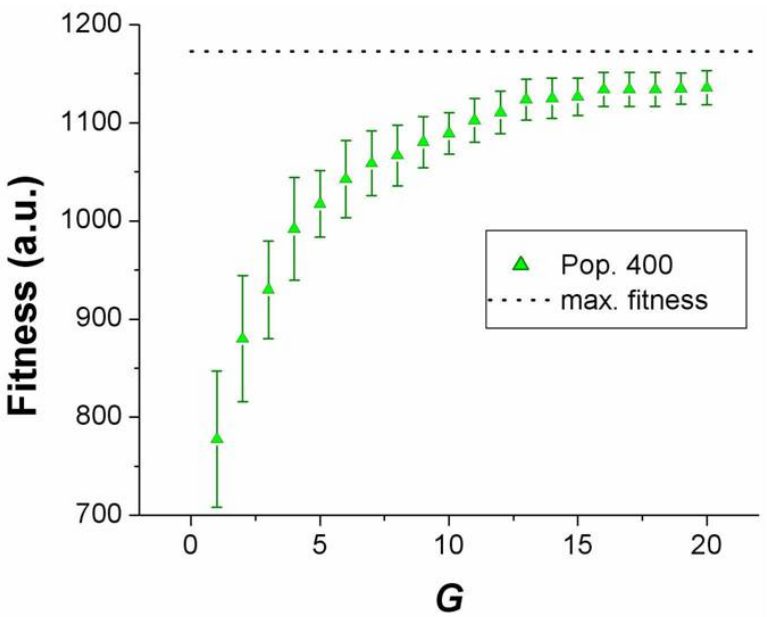

Figure 6.4: Simulated progression of SHG signals assuming the need to compensate a quadratic spectral phase. The plot shows average maximum fitness values (with standard deviation, error bars) attained over 40 simulations. Population $N = 400$ in the 9th order polynomial version of the GA.

6.2.2 Optimization of second harmonic signal and comparison with a phase retrieval method

For benchmarking the success of our genetic algorithms, we select an experiment where we can compare the results of our methods with those of another well established algorithm for spectral phase compensation of femtosecond pulses. In this case, we turn to comparison with a commercially available method based on multi-photon intra-pulse interference phase scan (MIIPS) [60, 61, 62].

The experimental setup for waveform synthesis via SH optical signals is shown in Fig. 6.5. A train of pulses (787 nm) from the Ti:S laser described in Chapter 3 passes through a collimating telescope and into the SLM-based pulse shaper of Fig. 6.1 (Coherent Silhouette). Pulses are attenuated with a reflective neutral density filter (ND = 0.5) and proceed to the BBO crystal unfocused ($\approx$ 140 mW). SH signals exit the crystal for detection while the undesired fundamental field is rejected by an IR filter attached to the backside of the crystal. There are two separate detection paths corresponding to the two methods we wish to compare. For use of the MIIPS algorithm, the SH signals ($\sim$ 395 nm) proceed to a spectrometer (Ocean Optics USB4000) for digitization. For use of our genetic algorithm, a mirror is inserted into the beam path to direct the SH optical signals to an amplified silicon detector (Thorlabs PDA36A). Additionally, this method requires the insertion of an optical chopper (415 Hz) to allow averaging of the collected electronic signals in a lock-in amplifier (Stanford Research Systems model 810). For both methods of optimization, the electronic signals, from the spectrometer and lock-in respectively, provide feedback to the software algorithm which then controls the shaper. This setup also allows for comparison of the total SH optical signals generated by both algorithms. Once the MIIPS optimization is finished, the movable mirror may be inserted to measure the resulting SH optical signals. Both optimization methods will seek to compensate the spectral phase distortions due to all of the dispersive optics

in the beam path (lenses, filters etc.), as well as any uncompensated phase from the Ti:S laser cavity itself.

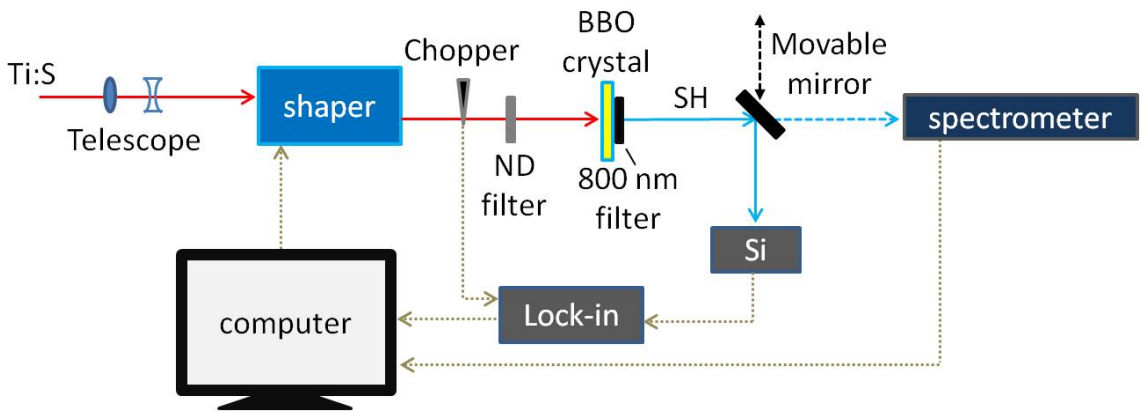

Figure 6.5: Setup for SH optimization via pulse shaping. Gold dotted lines indicate electronic connections.

MIIPS seeks to force the spectral phase to be flat (zero) at the SH crystal. This method works by using the SLM to place a known reference phase, f(ω), on top of the unknown spectral phase of the incoming pulse, $\phi(\omega)$. The total spectral phase of the pulse is then given by $\varphi(\omega) = \phi(\omega) + \mathrm{f}(\omega)$. MIIPS then monitors the SH spectrum of the pulse, which depends on $\varphi(\omega)$, to retrieve the unknown $\phi(\omega)$. This process is also accomplished with an iterative learning algorithm. Although this technique is quite powerful for characterizing the temporal waveform at a specific place in the beam path, namely the placement of the SH crystal, it requires the user to know *a priori* what waveform to implement. By default this technique reproduces pulses with flat spectral phase, that is, with bandwidth limited duration. In contrast, our algorithms only rely on maximization of a nonlinear optical signal and has the advantage of potentially producing arbitrary waveforms to do so. The results of these three methods, commercial MIIPS and our two GAs, may be compared for an experiment where nonlinear signal generation is expected to be maximized for pulses of bandwidth limited duration, where all techniques should find the same result. For

such an experiment we turn to optimization of SH signals produced by a Ti:S laser in a thin (0.01 mm) beta barium borate (BBO) nonlinear crystal. The BBO crystal has been used widely to produce SH from Ti:S lasers and yields maximum SH signals for a bandwidth limited pulse duration. This experiment allows MIIPS to optimize the spectral phase by monitoring the SH spectrum while forcing residual spectral phase to zero and it allows our genetic algorithms to optimize the spectral phase by maximizing detected SH signals.

The results of spectral phase compensation are shown in Fig. 6.6 for MIIPS and both variations of our genetic algorithm. The MIIPS software was run in the 'fine' compensation setting which takes approximately 5 minutes. Following optimization, MIIPS measured pulses that were compensated to be 3% longer than bandwidth limited duration resulting in $\approx$ 48 fs pulses. The 9th order polynomial version of the genetic algorithm was run with $N = 32$ $G = 20$ which took approximately 7 minutes to complete. The independent pixel version of the genetic algorithm was run with $N = 4$ $G = 1100$ and took approximately 2.6 hours to complete. The independent pixel version takes longer to progress because of both the increased number of parameters and the requirement of longer averaging time in the lock-in for signals beginning from random phase values applied to each pixel in the SLM phase mask. As expected for the independent pixel genetic algorithm, the pixels in the middle of the mask, with higher incident intensity (cf. Fig. 6.2), appear to be preferentially corrected. This explains why pixels at the edges of the compensated region show such large fluctuation.

The SH signals acquired for MIIPS, 9th order polynomial GA and independent pixel GA increase by factors of 3.0, 3.1 and 2.9 respectively compared to the signal acquired for no compensation (a flat phase applied to the SLM). If one makes a simplifying assumption that the uncorrected pulse had a broadened Gaussian shape, the (conserved) pulse energy may be estimated by the product of pulse duration and

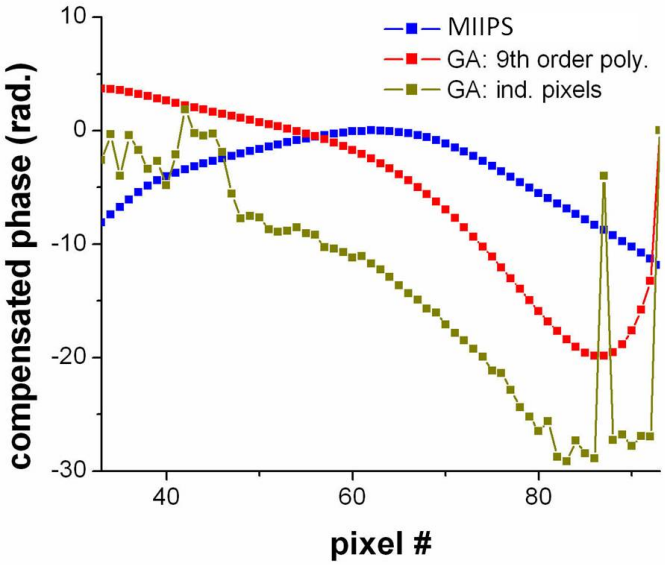

Figure 6.6: Comparison of the phase compensation found by the MIIPS program, the independent pixel GA and the 9th order polynomial GA for SHG.

peak power. Then assuming that the SH signals are proportional to energy via the squared peak power of the pulse, a factor of three increase in signal indicates that the uncompensated pulse duration was ≈ 48 fs$(\sqrt{3}) \approx 83$ fs.

Though the phase solutions shown in Fig. 6.6 are clearly different, they may still indicate the same temporal waveform. Recall from Eq. (6.1) that a linear change in $\phi(\omega)$ indicates only a change in the arrival time of the pulse, not a change in the waveform itself. Since MIIPS forced a phase compensation resulting in a near bandwidth limited pulse, we may compare to the MIIPS results and observe the difference in phase acquired with the other two algorithms. Figure 6.7 shows that the difference between MIIPS phase and the phase determined by our genetic algorithms is nearly linear across the central part of the phase mask (center of the incident spectrum). All three phase compensation results appear to be converging on the same pulse of bandwidth limited duration. This confirms that our genetic algorithms are capable of finding an optimal phase compensation using only the strength of the

nonlinear signal as feedback to the search process. Such confirmation lends a clear advantage to our algorithms in optimizations that require the ability to search for arbitrary spectral phase compensation.

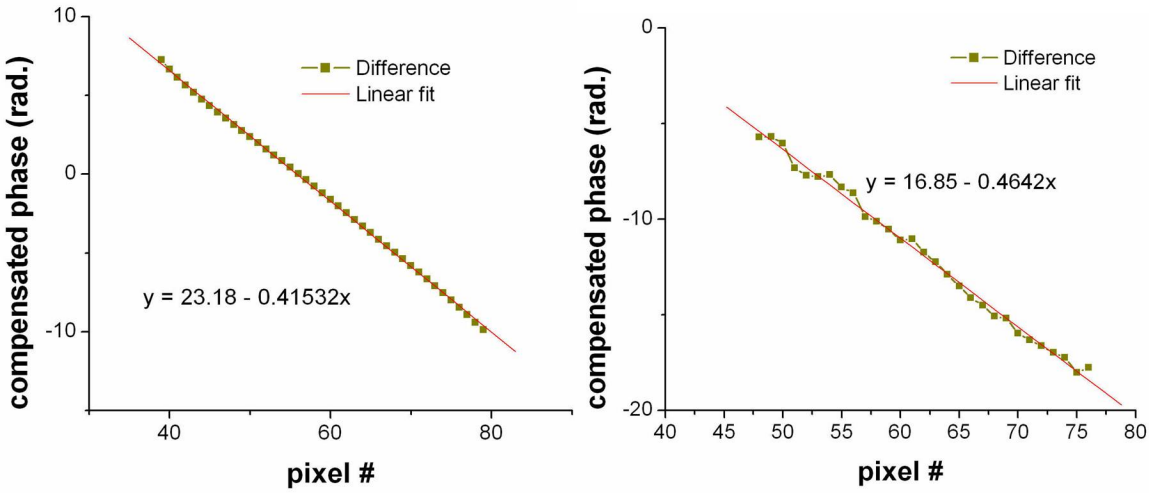

Figure 6.7: The difference in phase between (a) MIIPS and 9th order polynomial GA solutions, and (b) MIIPS and independent pixel GA solutions.

6.2.3 Optimization of third-harmonic microscope signal in fused silica

We now extend the use of our genetic algorithm to optimization of nonlinear signals produced in the focal volume of a microscope. To begin, we inspect TH signals produced from a fused silica slide (1 mm) under linearly polarized illumination. Since fused silica is expected to yield maximal TH signals from pulses of bandwidth limited duration (flat spectral phase) we may use this sample to characterize the uncompensated spectral phase of our typical setup.

The experimental setup for TH microscopy with temporal waveform synthesis is

shown in Fig. 6.8. This setup is nearly identical to the one described in Section 4.2. The main differences are the inclusion of a chopper (415 Hz) to enable lock-in detection and the inclusion of the pulse shaper itself. Time averaged electronic signals from the lock-in provide feedback to the software algorithm which then controls the shaper. This setup includes a prism compressor which attempts to compensate second order phase distortions corresponding to group delay dispersion (GDD). Its alignment is fine tuned by maximizing TH signals produced in the microscope. The optimization algorithm will seek to compensate the remaining spectral phase distortions due to all of the dispersive optics in the beam path (objectives, lenses, filters etc.), as well as any uncompensated phase from the Ti:S laser cavity itself. Note that this compensation also represents a best fit over radial coordinates for radially varying dispersion typical of thick lenses and microscope objectives. Measurements in fused silica are carried out with an average power of 320 mW entering the focusing objective.

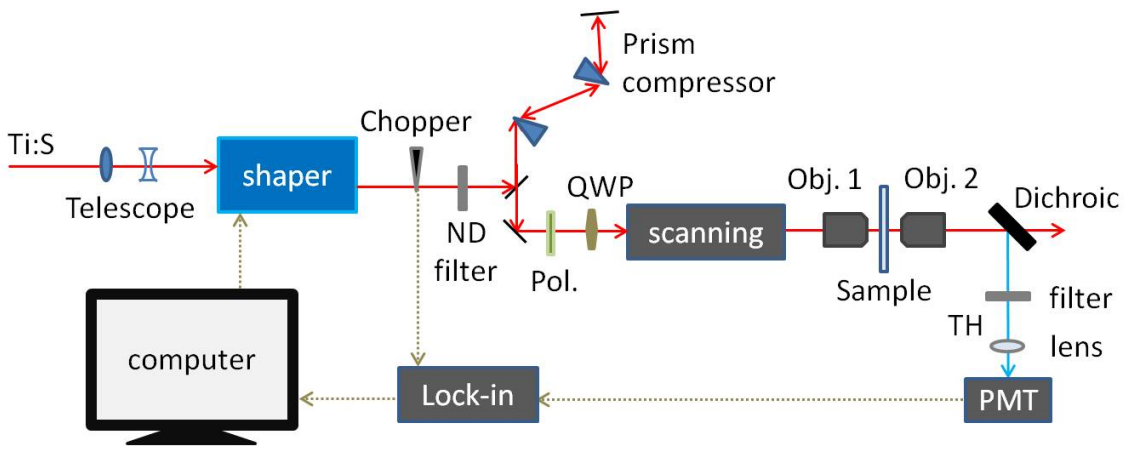

Figure 6.8: Setup for TH microscopy with temporal waveform synthesis. Gold dotted lines indicate electronic connections.

For spectral phase optimization in fused silica with the 9th order polynomial version of the genetic algorithm, the progression of TH signals (Fitness) is shown over

several generations of optimization in Fig. 6.9. Optimization of the spectral phase increases the TH signal by a factor of ≈ 12. For optimization with the independent pixel version of the genetic algorithm, TH signals increase by a factor of only ≈ 10, however the algorithm was halted after 3.1 hours while still making slow progression.

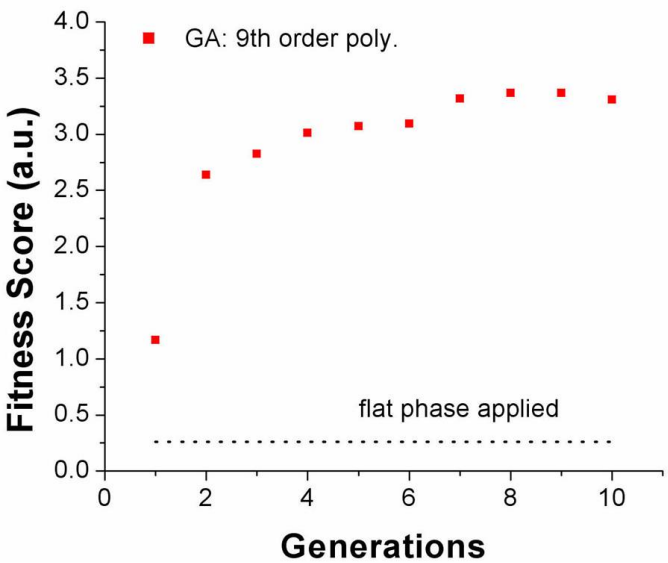

Figure 6.9: Progression of TH signals over ten generations of optimization with $N = 128$ in the 9th order polynomial GA. The dotted line represents the TH signals for an uncorrected pulse (flat phase applied to the SLM).

Comparing the spectral phase compensation results from both versions of the genetic algorithm in Fig. 6.10, we see that the difference is again linear. As was discussed in the last section, this indicates that the algorithms appear to be converging on the same temporal waveform since a linear difference in spectral phase indicates only a change in the arrival time of the pulses according to Eq. (6.1). If we assume that fully optimized spectral phase compensation leads to a 12× increase in TH signal as was observed for polynomial compensation, we can estimate the ratio of durations for compensated and uncompensated pulses. Assuming that TH signals are proportional to the cubed peak intensity of the pulse, a 12× in-

crease in signal indicates that the uncompensated pulse duration is estimated by $\tau_{uncomp} \approx (\sqrt[3]{12}\ \tau_{comp}) \approx 2.3\ \tau_{uncomp}$. We may attempt to confirm this by measuring the compensated and uncompensated pulse duration prior to the the focusing objective. Using a commercial FROG (frequency-resolved optical gating) measurement technique (Swamp Optics Grenouille), the uncompensated pulse has duration $\sim$ 140 fs and the compensated pulse has duration $\sim$ 56 fs prior to entering the focusing objective. The ratio of these two durations, 2.5, is close to the estimated ratio of 2.3 and may be expected to differ because of the dispersion effects within the focusing objective.

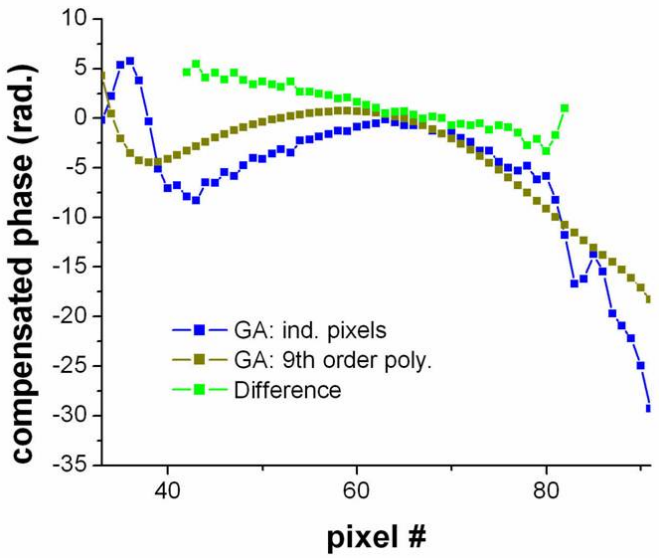

Figure 6.10: Comparison of phase solutions for TH signals using both GA versions. The difference is highly linear and indicates nearly identical temporal waveforms.

The addition of spectral phase compensation to the TH microscope repeatably leads to greater than ten fold increase in TH signal strength. While the reason for needing such relatively drastic compensation remains unclear, it may be related to the shear number of dispersive elements in the beam path which render the effects of higher order dispersion considerable.

6.2.4 Optimization of third harmonic microscope signal: observation of beam steering

Here we document the observation of beam steering encountered as a side effect of temporal waveform synthesis during the interrogation of gold film islands with TH microscopy. Gold triangles with variable aspect ratio A:B, Fig. 6.11a, were imaged with THLP (Fig. 6.11b) and THCP (Fig. 6.11c) techniques and were found to have signifcant THLP signals even when the illuminating beam was entirely within the area of the gold triangle (Fig. 6.11d). While such islands were originally of interest for potential size dependent suface plasmon enhancement of TH signals, no such effect was found. Here we report the effects of temporal waveform synthesis within triangles of aspect ratio 2:4.

Using the TH microscopy setup of Fig. 6.8, we optimize the temporal waveform with the 9th order polynomial version of the genetic algorithm for two positions of the focal spot, 1) centered within the area of the 2:4 ratio gold island of Fig. 6.12a and 2) centered entirely in the substrate. The resulting spectral phase compensation for each case is shown in Fig. 6.13. Both optimizations increase the total TH signal $\approx 9\times$ and their spectral phase difference is linear indicating the formation of identical temporal waveforms with different arrival times as discussed in the two previous sections. However, we note that the two spectral phase compensations lead to slightly shifted fields of view in the microscope. For example, we load the phase compensation determined for a focus in the substrate and then center the field of view of the microscope on the gold triangle as shown in Fig. 6.12a. Then simply by loading the phase compensation determined in the triangle, the field of view is shifted in the vertical direction $\approx$ 1 μm as shown in Fig. 6.12b. This shift in the field of view is easily reproduced by alternating between the two phase masks in repetition and is not simply due to a small movement of the sample. Considering the phase compensation found for focusing on the gold triangle, Fig. 6.13, we see how this

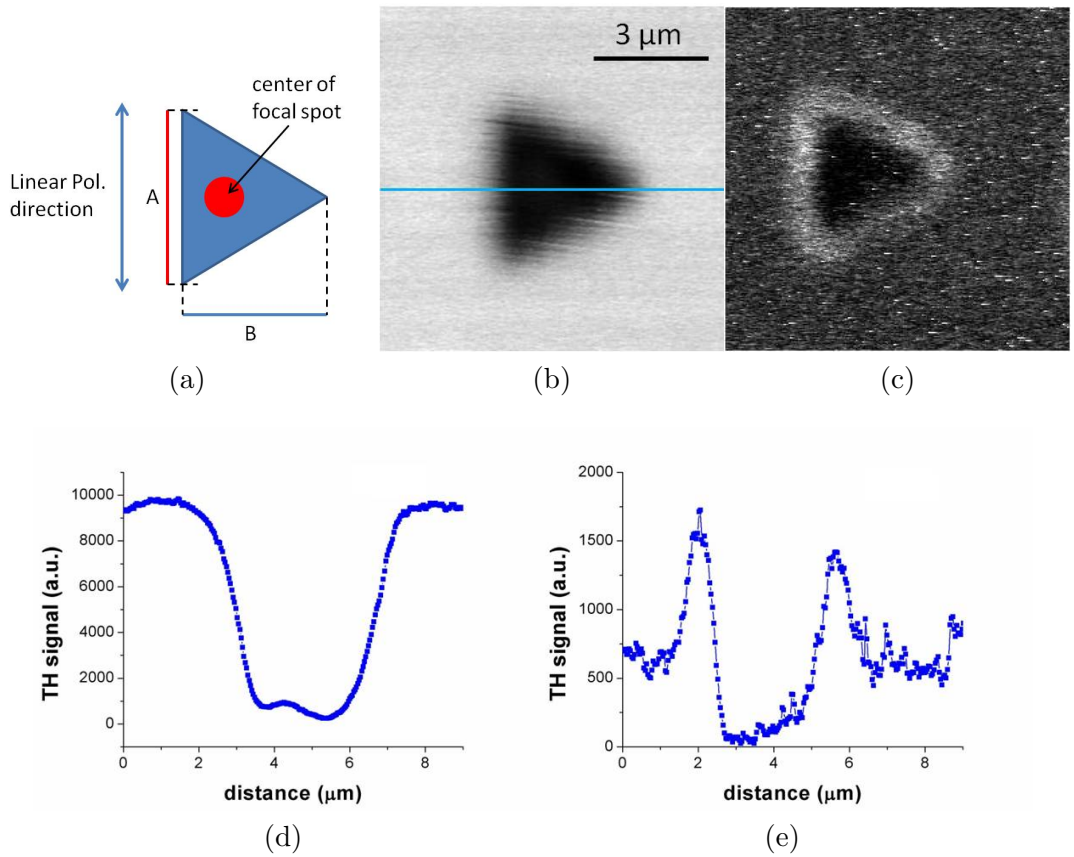

Figure 6.11: (a) Diagram of gold film islands with variable aspect ratio A:B from 1:4 to 4:4. (b) THLP image of 4:4 ratio gold triangle. (c) THCP image of 4:4 ratio gold triangle. Cross sections taken at the line in (b) of the THLP (d) and THCP (e) images respectively.

is possible. The total phase compensation includes a large linear component that covers $\approx$ 35 radians across the pulse spectrum from pixels 40 to 83 where the incident intensity is appreciable (cf. Fig. 6.2). Adding a linear phase across the SLM can be considered to have the same effect as adding a slight tilt to the back-reflecting mirror attached to the SLM (cf. Fig. 6.1), thus leading to a very slight redirection of the beam exiting the shaper. This redirection of the beam is in the correct direction to appear as a vertical shift in the field of view of the microscope. Presumably, the shaper simultaneously optimized the temporal waveform as well as the pointing

of the beam. In this case, by steering the beam away from the center of the gold triangle the TH signals increased as more of the incident beam became unimpeded by the triangle.

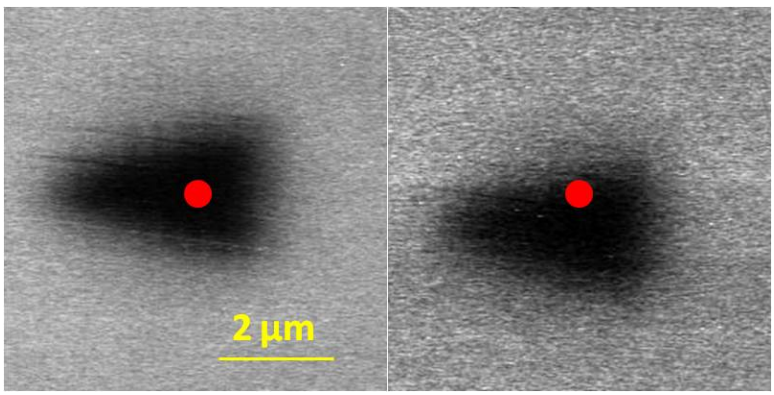

(a) (b)

Figure 6.12: THLP images of the same gold triangle for two different spectral phase compensations. The field of view shifts vertically due to the compensation. The red dot indicates the center of the field of view.

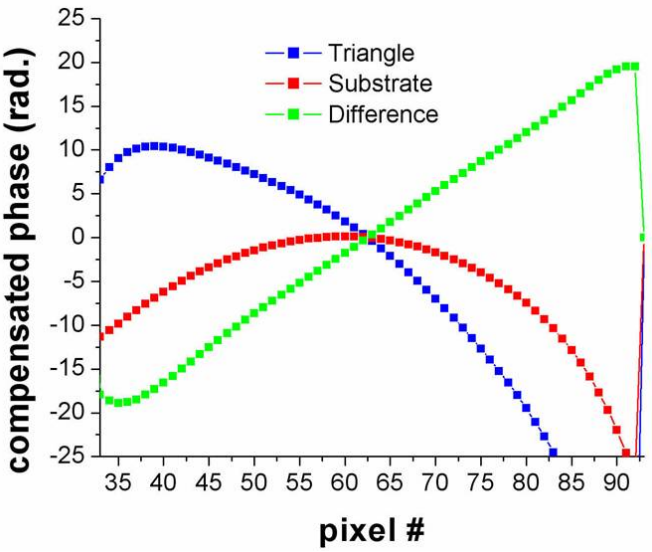

Figure 6.13: Spectral phase compensation for focus on the substrate and on the triangle of Fig. 6.12a. The difference is a large linear slope.

Although the shift in focal position caused by the shaper is only ≈ 1 μm this is not insignificant when considering many applications. For example, optical signals produced by nanoparticles may be sensitive to alignment position within the focal geometry of the beam diameter. Furthermore, automated control over fine spatial alignment may be useful when aligning the spatial overlap of two beams in the focal plane of a microscope as is often the case for FWM microscopy. Such simultaneous control over the temporal waveform and the fine tuning of spatial alignment may find many applications in microscopy, especially if two orthogonal liquid crystal masks are employed to allow alignment in both vertical and horizontal directions.

It should be noted that the shift in focal position is not critical for most applications. If desired, the shift in focal position is easily overcome by loading an additional linear phase to overcome that imposed by the shaper.

6.3 Chapter Summary

This chapter outlined the development and implementation of a genetic algorithm that works to optimize nonlinear signals via temporal waveform synthesis. The success of the algorithm is confirmed by comparing the resulting spectral phase compensation with that of a commercial technique. For cases of SHG and TH microscopy, the algorithm is able to increase nonlinear signals by factors of 3.1 and ≈ 12 respectively. The spectral phase compensation found for a fused silica sample in the TH microscope leads to a decrease in pulse duration by a factor of ≈ 2.3. Furthermore, for optimization in the TH microscope we observed an example of simultaneous waveform synthesis and beam steering applied by the shaper. Such an effect may be useful for fine alignment in the focal plane of nonlinear microscopes.

The version of the GA that makes use of indirect parameterization of the SLM pixels via a 9th order polynomial proves to be efficient, requiring only minutes to

search for a near optimal phase compensation, as well as practical, being well suited for routine compensation of multi-order optical dispersion commonly encountered in nonlinear microscopes. The version of the GA that makes use of direct parameterization of the SLM pixels presents a robust method to search for arbitrary phase compensation in problems that require the synthesis of complicated unknown temporal waveforms. This method still provides tenable efficiency for most problems, typically requiring a few hours to complete. The latter method is truly intriguing for it's potential to unveil hidden dynamics of systems as inferred from synthesized waveforms.

Chapter 7

Summary and implications for future work

The work presented in this thesis centers upon the characterization of material properties via third-harmonic (TH) and four-wave mixing (FWM) microscopy. The TH microscopy studies presented here focus on characterizing dielectric oxide thin films used in fs laser-induced damage threshold studies. The FWM microscopy studies presented here focus upon interpreting time-resolved signals that depend on the inter-pulse time delay between two laser excitation sources. TH and FWM studies were enhanced by improving both the stability and the output characteristics of the femtosecond laser sources they rely upon to create nonlinear optical signals. In addition, the development of a genetic algorithm that uses nonlinear optical signals as feedback for the synthesis of temporal waveforms opens up new applications for the TH and FWM microscopes employed here.

Both the titanium sapphire (Ti:S) and optical parametric oscillator (OPO) femtosecond laser sources were optimized for application to nonlinear microscopy. In the Ti:S laser, a proclivity for double pulse output was eradicated by reducing the intra-

cavity intensity through determination of a suitable (20%) outcoupler. Together with replacement of the pump focusing lens, this led to both an increase in average output power from 1.35 W to 1.42 W and and increase in modelocked spectral bandwidth from 16 nm to 19 nm. Both improvements contribute to increased peak intensity of the output thereby enhancing nonlinear signal generation. Additionally, a systematic study of two critical alignment regions in the Ti:S laser led to an increased stability ($>$ 24 hours duration) in the modelocked output. Improvements in the Ti:S laser proved to be useful for facilitating both increased sensitivity at the detection limit[†] in TH microscopy of oxide films, as well as extended duration experiments with the pulse shaper which required stable modelocking over several hours. In the OPO cavity, fine alignment of counterpropagating beams in the periodically poled lithium niobate (PPLN) crystal enabled a $TEM_{0,0}$ spatial mode output allowing for the removal of an intra-cavity knife's edge. Removal of the knife's edge also effectively doubled the output power of the OPO from 35 mW to 70 mW. $TEM_{0,0}$ output of the OPO is crucial for enabling ideal spatial overlap with the Ti:S beam in the focal plane of the FWM microscope.

We confirmed the value and sensitivity of TH microscopy applied to sources of contrast encountered in high quality oxide thin films. These studies commenced with TH imaging of fabricated sources of contrast thought to play a role in laser-induced damage of oxide thin films. In evaluating the sensitivity of TH from circularly polarized illumination (THCP) microscopy to induced anisotropy and nanoscale features, we presented the first ever high contrast images of both material strain induced by nanoindentation and individual 10 nm gold nanoparticles (S/N $>$ 100 : 1). To the author's knowledge these are the smallest individual nanoparticles imaged by any variation of TH microscopy. These results imply that THCP imaging is potentially sensitive to laser-induced strain as well as to nanoscale defects or contamination in

[†]Detection of small signals is limited here by maximum available laser power and maximum gain on the PMT.

oxide films.

TH imaging proved to deliver unique insight and high sensitivity to the oxide thin films in a variety of ways. Compared to other sensitive imaging techniques such as Nomarski and dark field, THCP imaging exhibits dramatically increased sensitivity to typical material modifications undergone during the formation of optical damage as evidenced by a dynamic range $\approx 10^6 : 1$. For further interrogation of optical damage sites, THCP images reveal the presence of permanent material modification not evidenced by other techniques. Simultaneously, TH from linearly polarized illumination (THLP) images show a unique ability to quantify the depth of material ablation. In answer to a long standing question, THCP images divulge the presence of permanent material modification even for laser exposures not leading to optical damage. A next logical step is to implement TH detection while a laser damage experiment is online. This may allow one to probe for the presence of short lived material modifications. Evidence in support of this thinking is provided by the THLP observation of reversible material modification in a scandia film. An exposure of $\approx 4.3{\times}10^8$ J/cm^2 total fluence incident on an 8×8 μm square of scandia film led to an $\sim$ 16% decrease in THLP signal generation. However, after 29 hours of recovery THLP signals rebounded to 95% of their value before the exposure. This reversible material modification is believed to be the first observed in oxide films.

Even prior to laser exposure, THCP images reveal features in the nascent oxide films themselves. These features are shown to correlate to strain in the film and the effect of their presence on damage threshold remains unclear. THCP imaging also may be useful for online monitoring of films during deposition if one desires to eliminate these features. TH imaging creates contrast where other techniques fail and should certainly continue to be applied to the study of laser damage morphology. TH imaging also displays promise for providing valuable information by interrogating films during deposition and during exposure to high fluence laser radiation.

The results of TH interrogation of oxide thin films may also hold relevance for nano- and micro-patterning of materials. This practice also makes use of the highly deterministic behavior of oxide films when exposed to femtosecond pulses, however, in this case it is exploited to make precise material modifications to the film. An example of such patterning in bulk material is the creation of optical damage within glass to yield 3-dimensional data storage accessed by THG [106]. Films hold unique interest for patterning because they constrain the depth of patterning within a range from a few atomic monolayers to several hundred nanometers.

With regard to FWM, we sought to characterize the behavior of two FWM microscopy signals as a function of the inter-pulse time delay between two excitation pulses. These two FWM signals, referred to as visible FWM and IR FWM respectively, show dependence on the delay between the excitation pulses especially when resonant processes contribute a significant percentage of either signal. Making use of several solvents (methanol, ethanol, propanol, butanol, hexane) these inter-pulse delay scans were shown to exhibit a material specific separation on the delay scale between the two FWM signal peaks. Comparing the relative positions of all the FWM signals indicated that the signal separation was due to a shift of the visible FWM signals towards positive delay values. Numerical modeling of coherent anti-Stokes Raman scattering (CARS), coherent Stokes Raman scattering (CSRS), visible stimulated parametric emission (SPE) and IR SPE signals suggest that a resonant CARS process which probes a characteristic material response time $\approx 90 - 100$ fs* is responsible for such a shift in visible FWM signals. This hypothesis is confirmed by suppressing resonant CARS signals with a polarization scheme. When resonant CARS signals are suppressed, inter-pulse delay scans no longer generate a delay separation between the two FWM signal peaks. Measurements indicate that the resonant contribution accounts for $\approx 95\%$ of the total visible FWM signal. The resonant fre-

*When determining the characteristic response times, the precision is limited by the sensitivity of the models used.

quency probed in the CARS process is in the range 2770-3130 cm^{-1}, as defined by the spectral FWHM of the excitation sources, and likely indicates the net effects of several Raman active C-H stretch bands near 2950 cm^{-1}. This technique may be applied to characterize the dominant resonant response of the sample under study. Furthermore this technique presents the newfound capability to provide estimates of characteristic material dephasing times in combination with spatial resolution ≈ 1 μm. Such a combination of information may be useful for applications such as monitoring the diffusion of resonant molecules into cellular components.

We also sought to develop and implement a genetic algorithm capable of optimizing nonlinear optical signals by interfacing with a spatial light modulator for temporal waveform synthesis of femtosecond regime optical pulses. The developed algorithm works by controlling the temporal pulse behavior via modulation in the frequency domain. Specifically, the algorithm modulates the spectral phase of the pulse through spatially separated spectral components incident on individual liquid crystal pixels in a phase mask. The algorithm relies on parameterization of the pixels in the phase mask to search for a pulse shape that results in the generation of maximal nonlinear optical signals. Two versions of the algorithm are developed, one with fully independent parameterization of the pixels, and one where the phase mask is parameterized through a 9th order polynomial function. The reduced parameter space for the 9th order polynomial version of the program leads to efficient determination of optimal pulses taking only several minutes. Indeed this version of the program proved suitable for compensating multiple orders of optical dispersion and, because of it's efficiency, could be used routinely to compensate dispersion anytime a setup is changed. Through application to second-harmonic generation (SHG) and comparison with another shaping method, the technique developed is shown to succeed in optimizing the temporal waveform automatically without any prior notion of the experiment involved. Applied to TH microscopy, the optimized pulses lead to $\gtrapprox$ 10$\times$ increase in TH signals from fused silica. Such an increase in signals allows

for more sensitive detection by promoting signals above the former detection limit of our setup. Optimization of TH signals from gold film islands revealed an interesting case where control of the spectral phase also resulted in a slight steering of the beam exiting the pulse shaper. This amounts to simultaneous waveform synthesis and automated spatial alignment. The algorithm developed has shown the potential to find complex temporal waveforms that optimize resonant nonlinear processes and illuminate the underlying physics. An obvious extension of this last point would be to apply the shaping algorithm to FWM of solvents. In this way, one could simultaneously probe a material resonance to reveal underlying dynamics while automatically optimizing the delay between excitation pulses.

Appendices

Appendix A

Interpretation of complementary far field imaging techniques

In order to most fully characterize laser damage exposures, studies may make use of several imaging techniques to provide complementary information. Linear far field imaging techniques boast unmatched prevalence and ease of use while demonstrating sensitivity to a considerable stable of contrast sources. TH microscopy establishes an entirely new basis of information by probing the third order material susceptibility while maintaining the benefits of a far field technique such as wide field of view, fast acquisition and ease of use. Here we compare the sources of contrast in TH imaging with those of several linear techniques commonly used in studying laser damage. For comparison, we view the same laser-induced damage crater with all the imaging techniques.

Figure A.1 shows images of a laser-induced damage crater in 110 nm hafnia film caused by a single laser pulse at 127 % damage threshold fluence taken with THCP, THLP, polarization, bright field, dark field and Nomarski imaging techniques. Let us review the sources of contrast for each imaging technique and interpret how that

effects the image of this particular damage spot. The THCP and THLP images are taken in transmission while all others are taken in a reflection configuration.

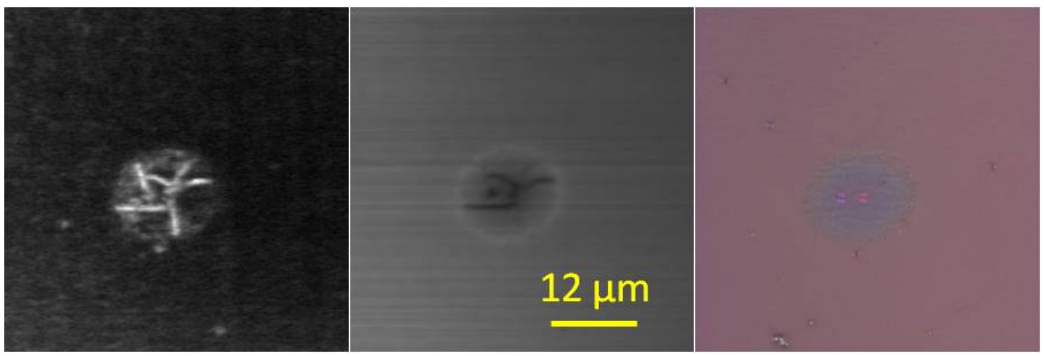

(a) THCP (b) THLP (c) Polarization

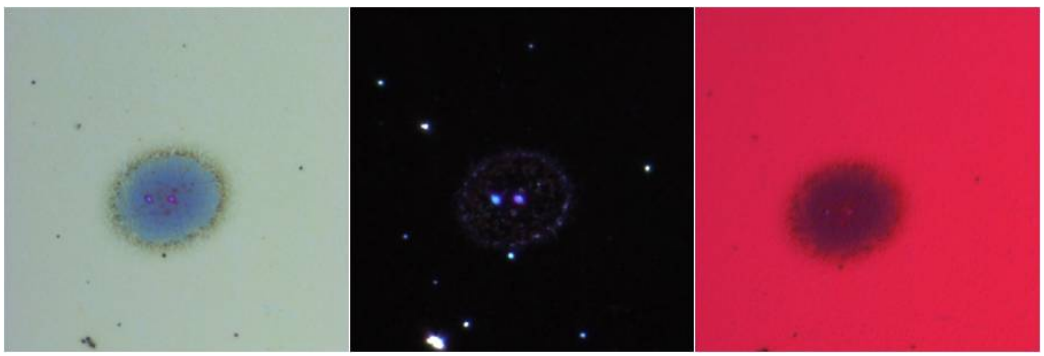

(d) Bright field (e) Dark Field (f) Nomarski

Figure A.1: Comparison images of a single pulse damage exposure in 110 nm hafnia thin film comprising the range of imaging techniques referenced by the author.

THCP images plot a distribution of anisotropy in $\chi^{(3)}$. Optical signals indicate regions where the isotropy condition ($\chi^{(3)}_{xyyx} = \chi^{(3)}_{xyxy} = \chi^{(3)}_{xxyy} = \frac{1}{3}\chi^{(3)}_{xxxx}$) is not met. THCP images may show contrast indicating birefringence, material strain, crystalline structures, material discontinuity, et cetera. Strong THCP signals in Fig. A.1a most likely indicate fracture lines in the film.

THLP images plot a distribution of $\chi^{(3)}$. THLP images may show contrast indicating the strength of $\chi^{(3)}$, the relative transmission and/or scattering of the fundamental field, et cetera. Dark lines in Fig. A.1b may indicate material removal

Polarization images plot a distribution of birefringence. Polarization images may reveal any source of contrast that can cause a change in polarization. Figure A.1c may reveal induced birefringence or increased scattering depolarization within the laser exposure.

Bright field images plot a distribution of absorbance and reflection coefficient. The color change in the middle of the exposure, Figure A.1d, may indicate the creation of defect absorbers or a delamination of the film from the substrate or a thinning of the film.

Dark field images plot a distribution of scatterers. The scatterers within the exposure, Fig. A.1e, may indicate fine fractures or surface roughness. The scatters outside the exposure indicate film contamination. Likely sources include dust and redeposited material expelled from within damage craters on this sample.

Nomarski images plot a distribution of the linear phase difference between orthogonally polarized paths. The flat dark nature of the exposure, Fig. A.1f, is typical of Nomarski images of a rough surface.

Taken together, these complementary imaging techniques assert that within the exposed spot the film was likely fractured and only partially removed. Additionally, it appears that material has been redistributed from within the exposure to the edge of the exposure leaving behind a rough interior surface. These assertions could not be made simply by consulting one image in the group.

Appendix B

Simulation of nonlinear signal optimization via temporal pulse shaping

Genetic algorithms represent a robust method of optimization, however they are not necessarily efficient. For this reason it is beneficial to implement user defined controls along with the typical optimization parameters. Typical controls include the population size, N, the number of generations, G, the initialization conditions, mutation rate, and the wait time necessary for interfacing with hardware and allowing for experimental equilibrium. Since optimization of these users controls would be prohibitively time consuming to determine through actual experimentation, we turn to simulation of the specific experiments we desire to carry out in the lab. This allows the computer to run in seconds what may take a day in the lab. In this way, not only do we determine reasonable parameters for the algorithm, but also we can determine the limitations on what is practical to accomplish given experimental constraints on time (laser stability, etcetera.) In general, all simulations are plotted as a function of fitness versus the product $N \times G$. $N \times G$ represents the total number of trial

solutions implemented to hardware and serves to estimate the time required to carry out an experiment. Here we present simulations of SHG and THG for a variety of conditions.

Simulations of SHG and THG account for parameterization across only the 60 middle pixels of the SLM as required by the intensity distribution of the Ti:S spectrum on the SLM (cf. Fig. 6.2). In this way, pixels with negligible incident intensity are removed from the optimization in an attempt to improve algorithm efficiency. All simulations make the assumption that for such a small FWHM in wavelength for the Ti:S (19 nm FWHM at 787 nm), the frequency of light incident at each pixel is approximately constant. With this assumption the signal for nth harmonic generation may be approximated by:

$$S_{nHG} \propto \left[\left(\sum_{i=1}^{60} A_i \cos(r_i - v_i) \right)^2 \right]^n \tag{B.1}$$

Where the index i indicates a pixel number, r_i are the values of the reference phase, v_i are the values of the current trial solution phase and A_i are the amplitudes given by a Gaussian distribution with FWHM 25 pixels. Quite simply, the reference phase is the solution goal. Eq. B.1 represents the fitness of a trial solution as outlined in Section 6.2.1. When the solution phase (set of v_i) matches the reference phase, the simulated signal is an absolute maximum and an ideal solution is found. However, the algorithm typically stops after the user defined number of generations. Everything inside the squared term indicates the simulated electric field. Everything inside the nth power term indicates the simulated intensity. It is important to note that because we have assumed identical frequency incident at each pixel, no integration in time is required.

All the data referenced here represents the mean maximum fitness (and standard

deviation) from at least 10 simulations.

Fig. B.1 shows SHG simulations in the 9th order polynomial version of the GA for several different population sizes. Simulations suggest an optimal population size of ≈ 25.

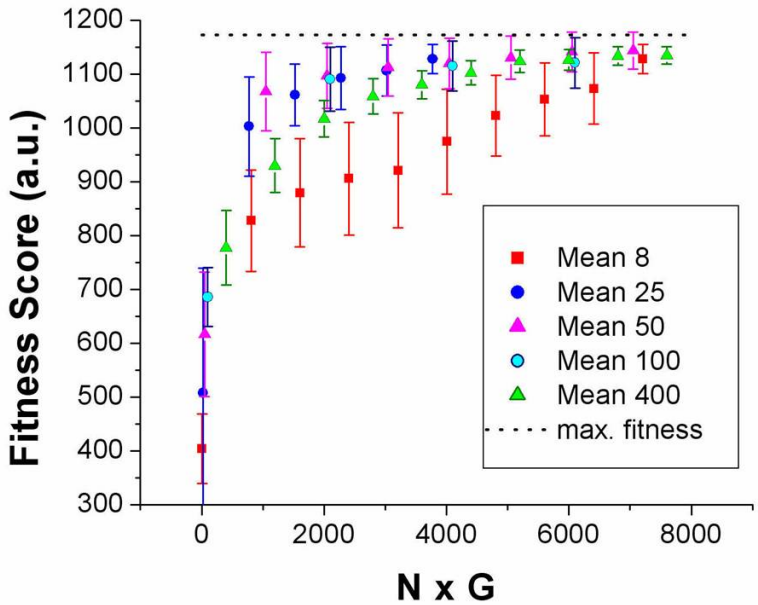

Figure B.1: Mean simulated SHG signal (and standard deviation) for several population sizes in the 9th polynomial fit version of the GA.

Fig. B.2 shows THG simulations in the 9th order polynomial version of the GA for several different population sizes. Simulations suggest an optimal population size of ≈ 8.

Fig. B.3 shows SHG simulations in the independent pixel version of the GA for several different population sizes. Simulations suggest an optimal population size of ≈ 4.

Fig. B.4 shows THG simulations in the independent pixel version of the GA for several different population sizes. Simulations suggest an optimal population size of $\approx 2 - 4$.

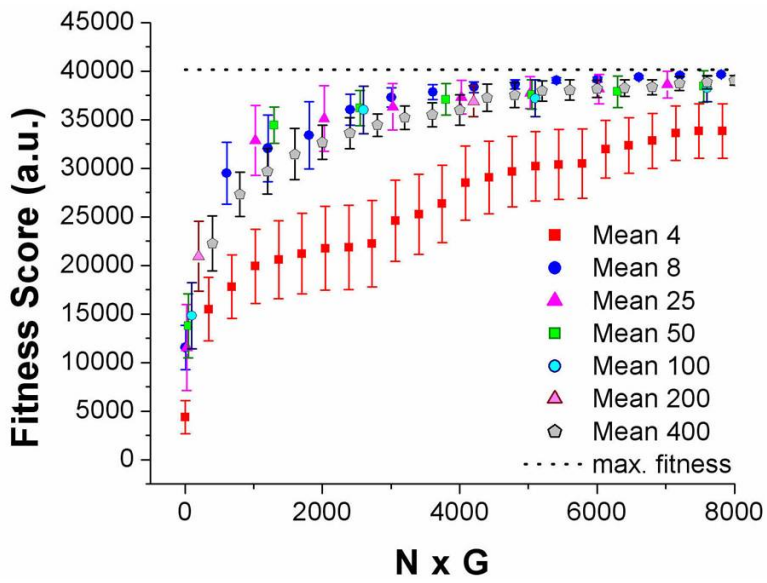

Figure B.2: Mean simulated TH signal (and standard deviation) for several population sizes in the 9th polynomial fit version of the GA.

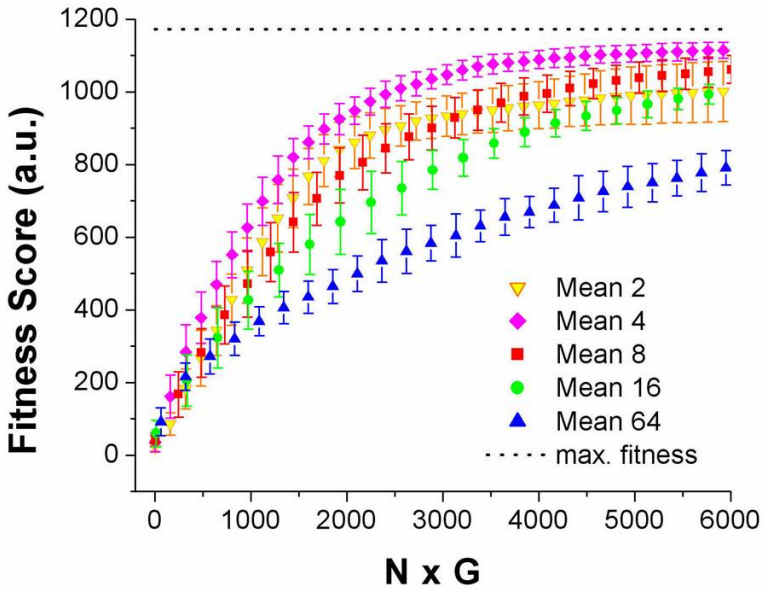

Figure B.3: Mean simulated SHG signal (and standard deviation) for several population sizes in the independent pixel version of the GA.

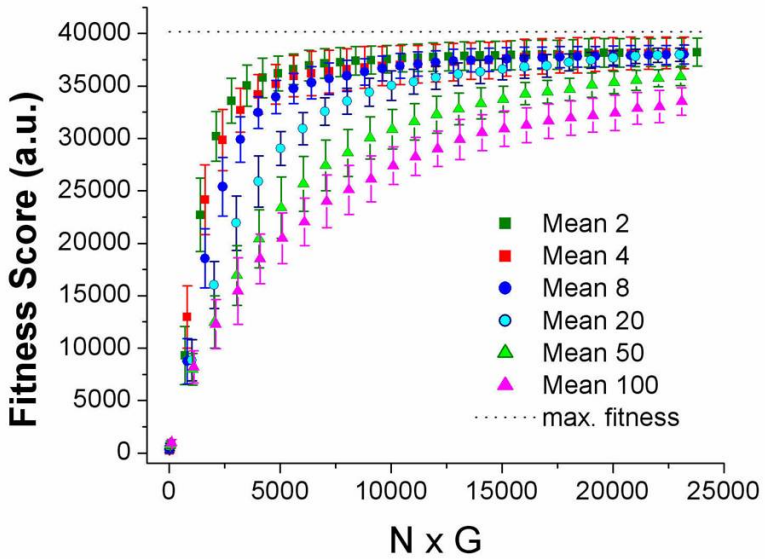

Figure B.4: Mean simulated TH signal (and standard deviation) for several population sizes in the independent pixel version of the GA.

Fig. B.5 shows SHG simulations in the independent pixel version of the GA and compares the progression of fitness for different reference phase shapes. Simulations suggest the independent pixel version of the GA works equally well for the different phase compensation shapes.

Fig. B.6 shows SHG simulations in the 9th order polynomial version of the GA and compares the progression of fitness for different reference phase shapes. Simulations suggest the 9th order polynomial version of the GA is not equally efficient at finding different phase compensation shapes.

Fig. B.7 shows SHG simulations in the independent pixel version of the GA and compares the progression of fitness for two cases of optimization with $N = 4$: phase mask only, and both phase and transmission (amplitude) masks. Simulations suggest the independent pixel version of the GA is much more efficient with only phase compensation. Here, 1400 generations corresponds to $\approx$ 196 minutes in the lab. Given a goal of 90% maximum fitness, it appears that simultaneous phase and

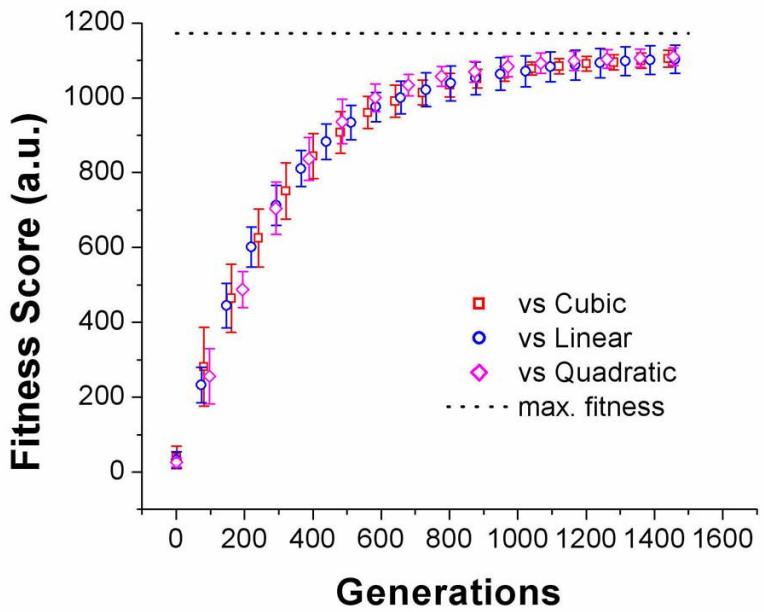

Figure B.5: Mean simulated SHG signal (and standard deviation) for different reference phase shapes in the independent pixel version of the GA.

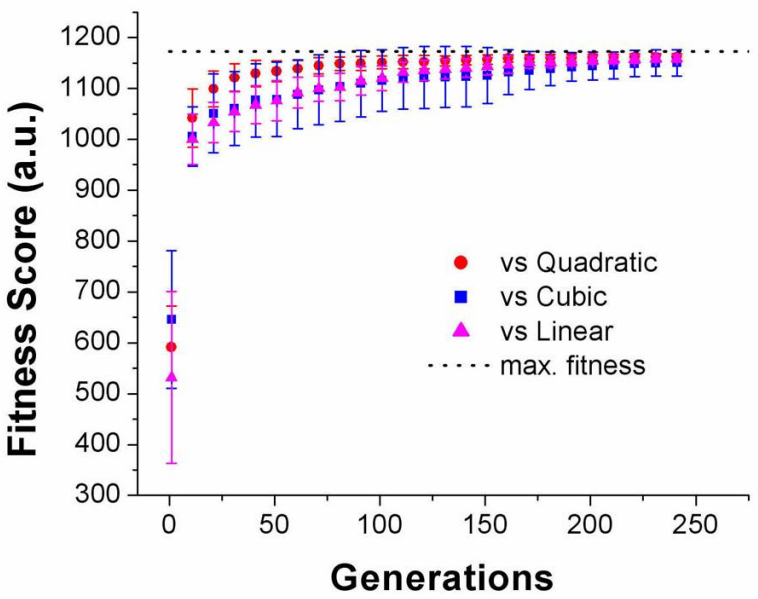

Figure B.6: Mean simulated SHG signal (and standard deviation) for different reference phase shapes in the 9th order polynomial version of the GA.

amplitude control requires too much time to be experimentally useful.

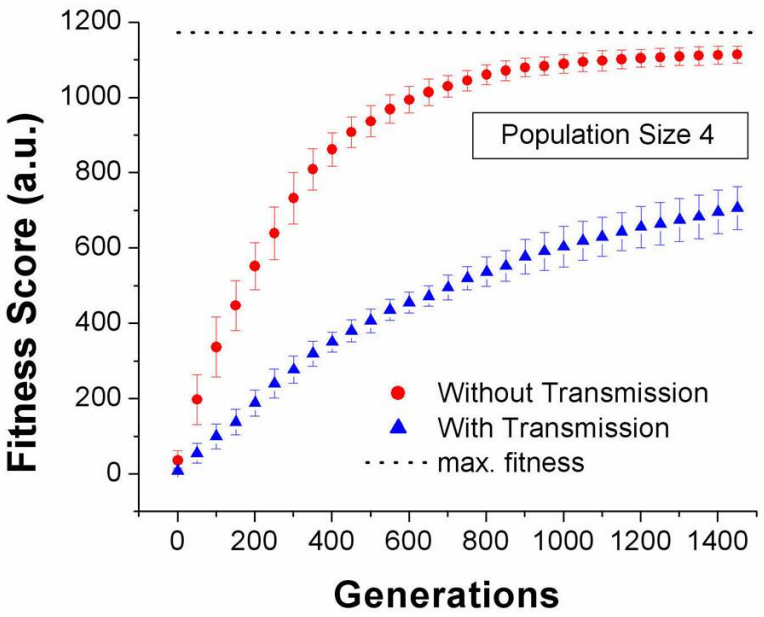

Figure B.7: Mean simulated SHG signal (and standard deviation) comparing phase compensation alone to phase plus transmission compensation in the independent pixel version of the GA.

References

[1] J. A. Squier, M. Müller, G. J. Brakenhoff, and K. R. Wilson, "Third-harmonic generation microscopy," *Optics express*, vol. 3, pp. 315–324, Dec. 1998.

[2] D. Oron and Y. Silberberg, "Third-harmonic generation with cylindrical Gaussian beams," *JOSA B*, vol. 21, no. 11, pp. 1964–1968, 2004.

[3] E. Tal, D. Oron, and Y. Silberberg, "Improved depth resolution in video-rate line-scanning multiphoton microscopy using temporal focusing," *Optics Letters*, vol. 30, no. 13, p. 1686, 2005.

[4] P. Franken, A. Hill, and C. Peters, "Generation of optical harmonics," *Physical Review Letters*, vol. 7, no. 4, pp. 118–120, 1961.

[5] R. Terhune, P. Maker, and C. Savage, "Optical harmonic generation in calcite," *Physical Review Letters*, vol. 8, no. May 1962, pp. 404–406, 1962.

[6] J. Ward and G. New, "Optical third harmonic generation in gases by a focused laser beam," *Physical Review*, vol. 185, no. 1, pp. 57–72, 1969.

[7] D. Kleinman, "Nonlinear dielectric polarization in optical media," *Physical Review*, vol. 126, no. 6, pp. 1977–79, 1962.

[8] H. Simon and N. Bloembergen, "Second-harmonic light generation in crystals with natural optical activity," *Physical Review*, vol. 171, Numbe, no. July 1968, pp. 1104–1114, 1968.

[9] W. Denk, J. H. Strickler, and W. W. Webb, "Two-photon laser scanning fluorescence microscopy.," *Science (New York, N.Y.)*, vol. 248, pp. 73–6, Apr. 1990.

[10] I. Freund and M. Deutsch, "Second-harmonic microscopy of biological tissue," *Optics letters*, vol. 11, no. 2, pp. 94–96, 1986.

[11] P. J. Campagnola, M.-d. Wei, A. Lewis, and L. M. Loew, "High-Resolution Nonlinear Optical Imaging of Live Cells by Second Harmonic Generation," *Biophysical Journal*, vol. 77, no. 6, pp. 3341–3349, 1999.

[12] Y. Barad, H. Eisenberg, M. Horowitz, and Y. Silberberg, "Nonlinear scanning laser microscopy by third harmonic generation," *Applied Physics Letters*, vol. 70, no. February 1997, pp. 922–924, 1997.

[13] M. Duncan, J. Reintjes, and T. Manuccia, "Scanning coherent anti-Stokes Raman microscope," *Optics Letters*, vol. 7, no. 8, pp. 350–352, 1982.

[14] W. R. Zipfel, R. M. Williams, and W. W. Webb, "Nonlinear magic: multiphoton microscopy in the biosciences.," *Nature biotechnology*, vol. 21, pp. 1369–77, Nov. 2003.

[15] R. W. Boyd, *Nonlinear Optics, 2nd ed.* Academic Press, 2003.

[16] M. Bakalar, J. L. Schroeder, R. Pursley, T. J. Pohida, B. Glancy, J. Taylor, D. Chess, P. Kellman, H. Xue, and R. S. Balaban, "Three-dimensional motion tracking for high-resolution optical microscopy, in vivo.," *Journal of microscopy*, vol. 246, pp. 237–47, June 2012.

[17] R. A. Farrer, M. J. Previte, C. E. Olson, L. A. Peyser, J. T. Fourkas, and P. T. So, "Single-molecule detection with a two-photon fluorescence microscope with fast-scanning capabilities and polarization sensitivity.," *Optics letters*, vol. 24, pp. 1832–4, Dec. 1999.

[18] D. Oron, D. Yelin, E. Tal, S. Raz, R. Fachima, and Y. Silberberg, "Depth-resolved structural imaging by third-harmonic generation microscopy.," *Journal of structural biology*, vol. 147, pp. 3–11, July 2004.

[19] D. Yelin, D. Oron, S. Thiberge, E. Moses, and Y. Silberberg, "Multiphoton plasmon-resonance microscopy.," *Optics express*, vol. 11, pp. 1385–91, June 2003.

[20] E. Korkotian, D. Oron, Y. Silberberg, and M. Segal, "Confocal microscopic imaging of fast UV-laser photolysis of caged compounds," *Journal of Neuroscience Methods*, vol. 133, pp. 153–159, Feb. 2004.

[21] D. Débarre, W. Supatto, A. Pena, A. Fabre, T. Tordjmann, L. Combettes, M. Schanne-Klein, and E. Beaurepaire, "Imaging lipid bodies in cells and tissues using third-harmonic generation microscopy," *Nature Methods*, vol. 3, no. 1, p. 47, 2006.

[22] J. M. Schins, T. Schrama, J. Squier, G. J. Brakenhoff, and M. Müller, "Determination of material properties by use of third-harmonic generation microscopy," *Journal of the Optical Society of America B*, vol. 19, p. 1627, July 2002.

[23] E. Fourkal, I. Velchev, A. Taffo, C. Ma, V. Khazak, and N. Skobeleva, "Photo-Thermal Cancer Therapy Using Gold Nanorods," in *World Congress on Medical Physics and Biomedical Engineering, September 7-12, 2009, Munich, Germany*, pp. 761–763, Springer, 2009.

[24] G. Filippidis, E. J. Gualda, K. Melessanaki, and C. Fotakis, "Nonlinear imaging microscopy techniques as diagnostic tools for art conservation studies.," *Optics letters*, vol. 33, pp. 240–2, Feb. 2008.

[25] D. Yelin and Y. Silberberg, "Laser scanning third-harmonic-generation microscopy in biology.," *Optics express*, vol. 5, pp. 169–75, Oct. 1999.

[26] D. Débarre, W. Supatto, and E. Beaurepaire, "Structure sensitivity in third-harmonic generation microscopy.," *Optics letters*, vol. 30, pp. 2134–6, Aug. 2005.

[27] D. Oron, E. Tal, and Y. Silberberg, "Depth-resolved multiphoton polarization microscopy by third-harmonic generation.," *Optics letters*, vol. 28, pp. 2315–7, Dec. 2003.

[28] B. Rethfeld, "Unified Model for the Free-Electron Avalanche in Laser-Irradiated Dielectrics," *Physical Review Letters*, vol. 92, pp. 1–4, May 2004.

[29] M. Mero, L. A. Emmert, and W. Rudolph, "The role of native and photoinduced defects in the multi-pulse subpicosecond damage behavior of oxide films," *Proceedings of SPIE*, vol. 7132, pp. 713209–713209–10, 2008.

[30] L. A. Emmert, M. Mero, and W. Rudolph, "Modeling the effect of native and laser-induced states on the dielectric breakdown of wide band gap optical materials by multiple subpicosecond laser pulses," *Journal of Applied Physics*, vol. 108, no. 4, p. 043523, 2010.

[31] B. Rethfeld, O. Brenk, N. Medvedev, H. Krutsch, and D. H. H. Hoffmann, "Interaction of dielectrics with femtosecond laser pulses: application of kinetic approach and multiple rate equation," *Applied Physics A*, vol. 101, pp. 19–25, June 2010.

[32] N. Medvedev and B. Rethfeld, "A comprehensive model for the ultrashort visible light irradiation of semiconductors," *Journal of Applied Physics*, vol. 108, no. 10, p. 103112, 2010.

[33] S. Demos, M. Staggs, K. Minoshima, and J. Fujimoto, "Characterization of laser induced damage sites in optical components.," *Optics express*, vol. 10, pp. 1444–50, Dec. 2002.

[34] L. Yuan, Y. Zhao, G. Shang, C. Wang, H. He, J. Shao, and Z. Fan, "Comparison of femtosecond and nanosecond laser-induced damage in HfO2 single-layer film and HfO2-SiO2 high reflector," *J. Opt. Soc. Am. B*, vol. 24, no. 3, pp. 538–543, 2007.

[35] D. N. Nguyen, L. a. Emmert, P. Schwoebel, D. Patel, C. S. Menoni, M. Shinn, and W. Rudolph, "Femtosecond pulse damage thresholds of dielectric coatings in vacuum.," *Optics express*, vol. 19, pp. 5690–7, Mar. 2011.

[36] A. Foster, F. Lopez Gejo, A. Shluger, and R. Nieminen, "Vacancy and interstitial defects in hafnia," *Physical Review B*, vol. 65, pp. 1–13, May 2002.

[37] O. Schwartz and D. Oron, "Background-free third harmonic imaging of gold nanorods.," *Nano letters*, vol. 9, pp. 4093–7, Dec. 2009.

[38] V. V. Yakovlev and S. V. Govorkov, "Diagnostics of surface layer disordering using optical third harmonic generation of a circular polarized light," *Applied Physics Letters*, vol. 79, no. 25, p. 4136, 2001.

[39] S. Konorov, A. Ivanov, M. Alfimov, and A. Zheltikov, "Third-harmonic generation as a local probe for on-line monitoring of femtosecond optical breakdown in transparent materials," *Journal of Optics A*, vol. 5, no. 2003, pp. 362–366, 2003.

[40] M. Muller, J. Squier, De Lange CA, and G. Brakenhoff, "CARS microscopy with folded BoxCARS phasematching," *Journal of microscopy*, vol. 197 (Pt 2), pp. 150–8, Feb. 2000.

[41] N. Kurnit, I. Abella, and S. Hartmann, "Observation of a photon echo," *Physical Review Letters*, vol. 13, no. 19, pp. 567–569, 1964.

[42] W. de Boeij, M. Pshenichnikov, and D. A. Wiersma, "Ultrafast solvation dynamics explored by femtosecond photon echo spectroscopies," *Annual review of*, pp. 99–123, 1998.

[43] J. Stenger, D. Madsen, P. Hamm, E. T. J. Nibbering, and T. Elsaesser, "A Photon Echo Peak Shift Study of Liquid Water ," *The Journal of Physical Chemistry A*, vol. 106, pp. 2341–2350, Mar. 2002.

[44] M. Fickenscher, H. Purucker, and A. Laubereau, "Resonant vibrational dephasing investigated by high-precision femtosecond CARS," *Chemical physics letters*, vol. 191, no. 1-2, pp. 182–188, 1992.

[45] H. Okamoto and K. Yoshihara, "Femtosecond time-resolved coherent Raman scattering under various polarization and resonance conditions," *Journal of the Optical Society of America B*, vol. 7, p. 1702, Aug. 1990.

[46] J.-L. Oudar, R. W. Smith, and Y. R. Shen, "Polarization-sensitive coherent anti-Stokes Raman spectroscopy," *Applied Physics Letters*, vol. 34, no. 11, p. 758, 1979.

[47] J. X. Cheng, L. D. Book, and X. S. Xie, "Polarization coherent anti-Stokes Raman scattering microscopy.," *Optics letters*, vol. 26, pp. 1341–3, Sept. 2001.

[48] A. Volkmer, J.-X. Cheng, and X. Sunney Xie, "Vibrational Imaging with High Sensitivity via Epidetected Coherent Anti-Stokes Raman Scattering Microscopy," *Physical Review Letters*, vol. 87, pp. 2–5, June 2001.

[49] K. Isobe, S. Kataoka, R. Murase, W. Watanabe, T. Higashi, S. Kawakami, S. Matsunaga, K. Fukui, and K. Itoh, "Stimulated parametric emission microscopy.," *Optics express*, vol. 14, pp. 786–93, Jan. 2006.

[50] X. Liu, W. Rudolph, and J. L. Thomas, "Photobleaching resistance of stimulated parametric emission in microscopy.," *Optics letters*, vol. 34, pp. 304–6, Feb. 2009.

[51] X. Liu, W. Rudolph, and J. L. Thomas, "Characterization and application of femtosecond infrared stimulated parametric emission microscopy," *Journal of the Optical Society of America B*, vol. 27, p. 787, Mar. 2010.

[52] H. M. Dang, T. Kawasumi, G. Omura, T. Umano, S. Kajiyama, Y. Ozeki, K. Itoh, and K. Fukui, "Three-Dimensional Unstained Live-Cell Imaging Using Stimulated Parametric Emission Microscopy," *Japanese Journal of Applied Physics*, vol. 48, p. 097003, Sept. 2009.

[53] W. Dietel, J. J. Fontaine, and J. C. Diels, "Intracavity pulse compression with glass: a new method of generating pulses shorter than 60 fsec.," *Optics letters*, vol. 8, pp. 4–6, Jan. 1983.

[54] R. L. Fork, O. E. Martinez, and J. P. Gordon, "Negative dispersion using pairs of prisms.," *Optics letters*, vol. 9, pp. 150–2, May 1984.

[55] M. Müller, J. Squier, R. Wolleschensky, U. Simon, and G. Brakenhoff, "Dispersion pre-compensation of 15 femtosecond optical pulses for high-numerical-aperture objectives.," *Journal of microscopy*, vol. 191, pp. 141–150, Aug. 1998.

[56] A. Assion, T. Baumert, M. Bergt, T. Brixner, B. Kiefer, V. Seyfried, M. Strehle, and G. Gerber, "Control of chemical reactions by feedback-optimized phase-shaped femtosecond laser pulses," *Science (New York, N.Y.)*, vol. 282, pp. 919–22, Oct. 1998.

[57] N. Dudovich, D. Oron, and Y. Silberberg, "Single-pulse coherently controlled nonlinear Raman spectroscopy and microscopy.," *Nature*, vol. 418, pp. 512–4, Aug. 2002.

[58] S. Postma, A. Rhijn, J. Korterik, J. Herek, and H. Offerhaus, "Femtosecond spectral phase shaping for CARS spectroscopy and imaging," *Ultrafast Phenomena XVI*, vol. 92, no. 6, pp. 523–525, 2009.

[59] A. M. Weiner, "Femtosecond pulse shaping using spatial light modulators," *Review of Scientific Instruments*, vol. 71, no. 5, p. 1929, 2000.

[60] K. Walowicz, I. Pastirk, V. Lozovoy, and M. Dantus, "Multiphoton intrapulse interference. 1. Control of multiphoton processes in condensed phases," *The Journal of Physical Chemistry A*, vol. 106, no. 41, pp. 9369–9373, 2002.

[61] V. V. Lozovoy, I. Pastirk, and M. Dantus, "Multiphoton intrapulse interference. IV. Ultrashort laser pulse spectral phase characterization and compensation.," *Optics letters*, vol. 29, pp. 775–7, Apr. 2004.

[62] M. Comstock, V. Lozovoy, I. Pastirk, and M. Dantus, "Multiphoton intrapulse interference 6; binary phase shaping.," *Optics express*, vol. 12, pp. 1061–6, Mar. 2004.

[63] F. Weise and A. Lindinger, "Full control over the electric field using four liquid crystal arrays," *Optics letters*, vol. 34, no. 8, pp. 1258–1260, 2009.

[64] P. J. Campagnola, A. C. Millard, M. Terasaki, P. E. Hoppe, C. J. Malone, and W. A. Mohler, "Three-dimensional high-resolution second-harmonic generation imaging of endogenous structural proteins in biological tissues.," *Biophysical journal*, vol. 82, pp. 493–508, Jan. 2002.

[65] D. Yelin, Y. Silberberg, Y. Barad, and J. S. Patel, "Depth-resolved imaging of nematic liquid crystals by third-harmonic microscopy," *Applied Physics Letters*, vol. 74, no. 21, p. 3107, 1999.

[66] C. Rodríguez, "Computational modeling of TH microscopy signals in thin films." Group report, March 2012.

[67] W. Burns and N. Bloembergen, "Third-harmonic generation in absorbing media of cubic or isotropic symmetry," *Physical Review B*, vol. 4, no. 10, pp. 3437–3450, 1971.

[68] X. Liu, *Imaging with and without time resolution using femtosecond laser pulses*. PhD thesis, University of New Mexico, 2009.

[69] S. Uemura and K. Torizuka, "Development of a diode-pumped Kerr-lens mode-locked Cr:LiSAF laser," *IEEE Journal of Quantum Electronics*, vol. 39, pp. 68–73, Jan. 2003.

[70] O. Masihzadeh, P. Schlup, and R. A. Bartels, "Enhanced spatial resolution in third-harmonic microscopy through polarization switching.," *Optics letters*, vol. 34, pp. 1240–2, Apr. 2009.

[71] J. C. Diels and W. Rudolph, *Ultrashort Laser Pulse Phenomena, 2nd ed.* Academic Press, 2006.

[72] V. P. Kalosha, M. Müller, J. Herrmann, and S. Gatz, "Spatiotemporal model of femtosecond pulse generation in Kerr-lens mode-locked solid-state lasers," *Journal of the Optical Society of America B*, vol. 15, p. 535, Feb. 1998.

[73] J. L. A. Chilla and O. E. Martinez, "Spatialtemporal analysis of the self-mode-locked Ti: sapphire laser," *Journal of the Optical Society of America B*, vol. 10, p. 638, Apr. 1993.

[74] T. Brabec, C. Spielmann, P. F. Curley, and F. Krausz, "Kerr lens mode locking.," *Optics letters*, vol. 17, pp. 1292–4, Sept. 1992.

[75] M. Lai, J. Nicholson, and W. Rudolph, "Multiple pulse operation of a femtosecond Ti: sapphire laser," *Optics communications*, vol. 142, no. 1-3, pp. 45–49, 1997.

[76] R. Stock, "Femtosecond electron relaxation dynamics in gold," Master's thesis, University of New Mexico, 2001.

[77] D. Jones, S. Diddams, J. Ranka, A. Stentz, R. Windeler, J. Hall, and S. Cundiff, "Carrier-envelope phase control of femtosecond mode-locked lasers and direct optical frequency synthesis," *Science (New York, N.Y.)*, vol. 288, pp. 635–40, Apr. 2000.

[78] T. M. Fortier, D. J. Jones, J. Ye, S. T. Cundiff, and R. S. Windeler, "Long-term carrier-envelope phase coherence.," *Optics letters*, vol. 27, pp. 1436–8, Aug. 2002.

[79] M. Mero, *Femtosecond laser induced electron-lattice dynamics and breakdown in dielectric oxide films*. PhD thesis, University of New Mexico, 2005.

[80] M. Sparks, D. Mills, R. Warren, T. Holstein, A. A. Maradudin, L. J. Sham, E. Loh, and D. F. King, "Theory of electron-avalanche breakdown in solids," *Physical Review B*, vol. 24, no. 6, pp. 3519–3536, 1981.

[81] R. Stoian, D. Ashkenasi, A. Rosenfeld, and E. E. B. Campbell, "Coulomb explosion in ultrashort pulsed laser ablation of Al_ {2} O_ {3}," *Physical Review B*, vol. 62, no. 19, pp. 167–173, 2000.

[82] B. Rethfeld, K. Sokolowski-Tinten, D. Von Der Linde, and S. I. Anisimov, "Timescales in the response of materials to femtosecond laser excitation," *Physics A: Materials*, vol. 79, pp. 767–769, 2004.

[83] W. Rudolph, L. a. Emmert, D. N. Nguyen, M. Mero, D. Patel, C. S. Menoni, and C. Phipps, "Single and Multiple Pulse Subpicosecond Breakdown in Dielectric Films," vol. 380, no. 1, pp. 380–391, 2010.

[84] T. A. Pologruto, B. L. Sabatini, and K. Svoboda, "ScanImage: flexible software for operating laser scanning microscopes.," *Biomedical engineering online*, vol. 2, p. 13, May 2003.

[85] J. T. Verdeyen, *Laser Electronics, 3rd ed.* Prentice Hall, 2000.

[86] M. Klein and T. Furtak, *Optics, 2nd ed.* John Wiley & Sons, 1986.

[87] B. Boulbry, B. Bousquet, B. Le Jeune, Y. Guern, and J. Lotrian, "Polarization errors associated with zero-order achromatic quarter-wave plates in the whole visible spectral range.," *Optics express*, vol. 9, pp. 225–35, Aug. 2001.

[88] S. Xu, X. Zeng, G. Zheng, and D. Zou, "Flat broadband birefringent retardation of the zero-order quarter-wave plates made from multi-birefringent materials," *ICEOE*, vol. 4, pp. 174–177, 2011.

[89] M. Lippitz, M. A. van Dijk, and M. Orrit, "Third-harmonic generation from single gold nanoparticles.," *Nano letters*, vol. 5, pp. 799–802, Apr. 2005.

[90] S. Fomichev, S. Popruzhenko, D. F. Zaretsky, and W. Becker, "Laser-induced nonlinear excitation of collective electron motion in a cluster," *Journal of Physics B:*, vol. 36, pp. 3817–3834, 2003.

[91] J. Yguerabide and E. E. Yguerabide, "Light-scattering submicroscopic particles as highly fluorescent analogs and their use as tracer labels in clinical and biological applications.," *Analytical biochemistry*, vol. 262, pp. 157–76, Sept. 1998.

[92] T. Masuda, T. Miyake, and M. Enami, "Ultra-high residual compressive stress ($>$ 2 GPa) in a very small volume ($<$ 1 μm^3) of indented quartz," *American Mineralogist*, vol. 96, pp. 283–287, Feb. 2011.

[93] S. Kohli, P. R. McCurdy, C. D. Rithner, P. K. Dorhout, A. M. Dummer, and C. S. Menoni, "Effect of Annealing on the Interfacial and Structural Properties of Amorphous Silicon-Hafnia Films," *Metallurgical and Materials Transactions A*, vol. 42, pp. 71–75, Nov. 2010.

[94] D. N. Nguyen, "Notes on laser induced damage of hafnia." Personal correspondence.

[95] C. S. Menoni, E. M. Krous, D. Patel, P. Langston, J. Tollerud, D. N. Nguyen, L. A. Emmert, A. Markosyan, R. Route, M. Fejer, and W. Rudolph, "Advances in ion beam sputtered Sc2O3 for optical interference coatings," *Proceedings of SPIE*, vol. 7842, pp. 784202–1–12, 2010.

[96] W. Rudolph, C. S. Menoni, and S. Peplinski, "Development, modeling and test of optical coatings with novel thermal and stress management for high-energy laser applications." Program Review, 2012.

[97] A. Markosyan and C. S. Menoni, "Photothermal common path interferometer absorption data." Personal correspondence, 2012.

[98] X. Zhang, "Photothermal absorption measurements in scandia thin films." Group Report, 2012.

[99] R. A. Weber, C. Rodríguez, D. N. Nguyen, L. A. Emmert, D. Patel, C. S. Menoni, and W. Rudolph, "Third harmonic microscopy of intrinsic and induced material anisotropy in dielectric thin films," *Optical Engineering*, vol. 51, Dec. 2012.

[100] A. M. Weiner, S. D. Silvestri, and E. P. Ippen, "Three-pulse scattering for femtosecond dephasing studies: theory and experiment," *Journal of the Optical Society of America B*, vol. 2, p. 654, Apr. 1985.

[101] T. Basiev, A. Sobol, P. Zverev, V. Osiko, and R. Powell, "Comparative spontaneous Raman spectroscopy of crystals for Raman lasers," *Applied optics*, vol. 38, no. 3, pp. 594–598, 1999.

[102] Y. Coello, V. Lozovoy, T. Gunaratne, and B. Xu, "Interference without an interferometer: a different approach to measuring, compressing, and shaping ultrashort laser pulses," *JOSA B*, vol. 25, no. 6, pp. 140–150, 2008.

[103] D. Oron and Y. Silberberg, "Harmonic generation with temporally focused ultrashort pulses," *JOSA B*, vol. 22, no. 12, pp. 2660–2663, 2005.

[104] J. Holland, *Adaptation in natural and artificial systems*. University of Michigan press, 1975.

[105] T. Back, *Evolutionary algorithms in theory and practice*. Oxford University press, 1996.

[106] J. A. Squier and M. Müller, "Third-harmonic generation imaging of laser-induced breakdown in glass.," *Applied optics*, vol. 38, pp. 5789–94, Sept. 1999.